LBL-10035

Lawrence Berkeley Laboratory
UNIVERSITY OF CALIFORNIA
Physics, Computer Science & Mathematics Division

DIMUON PRODUCTION BY HIGH ENERGY NEUTRINOS AND ANTINEUTRINOS IN THE FERMILAB FIFTEEN-FOOT BUBBLE CHAMBER

John L. Orthel
(Ph. D. thesis)

September 1979

Prepared for the U.S. Department of Energy under Contract W-7405-ENG-48

LBL-10035

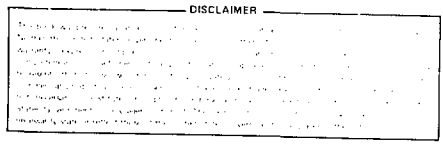

DIMUON PRODUCTION BY HIGH ENERGY NEUTRINOS AND ANTINEUTRINOS IN THE FERMILAB FIFTEEN-FOOT BUBBLE CHAMBER *

John L. Orthel
(Ph.D. Thesis)

Lawrence Berkeley Laboratory
University of California
Berkeley, California 94720

September 1979

* This work was supported by the Physics, Computer Science & Mathematics Division of the Lawrence Berkeley Laboratory under the U. S. Department of Energy under Contract W-7405-ENG-48.

DIMUON PRODUCTION BY HIGH ENERGY NEUTRINOS AND ANTINEUTRINOS IN THE FERMILAB FIFTEEN-FOOT BUBBLE CHAMBER

JOHN L. ORTHEL

UNIVERSITY OF CALIFORNIA AT BERKELEY

ABSTRACT

The Fermilab fifteen foot bubble chamber/two-plane External Muon Identifier (EMI) hybrid detector filled with *Ne*(47% atomic)-H_2 is exposed to the quadrupole triplet beam ($<E_{\nu_\mu}>$ = 89 GeV, $<E_{\bar{\nu}_\mu}>$ = 60 GeV). In 326000 pictures there are 10148 neutrino and 1773 antineutrino charged current events with two-plane EMI muon identification and muon momenta > 4 GeV/c. In this sample there are 55 $\mu^-\mu^+X$, 11 $\mu^-\mu^-X$ and 0 $\mu^+\mu^+X$ candidates with muon momenta > 4 GeV/c. The like-sign events are consistent with background. The opposite-sign dimuons occur at $R_{\mu\mu} = 0.35\pm0.10\%$ of the single muon rate. The ν_μ -induced $\mu^-\mu^+$ rate is $0.20\pm0.15\%$ below E_{ν_μ} = 100 GeV and $0.50\pm0.30\%$ above 100 GeV. In the opposite sign dimuons there are 10 candidates with an associated V^0 implying 0.76 ± 0.36 neutral strange particle per opposite sign dimuon event. The production rate, excess of neutral strange particles, and kinematic distributions of the dimuon events are consistent with the charm model predictions.

CONTENTS page

1. INTRODUCTION

The neutrino is somewhat unique in its ability to transform the nature of matter. If there are new degrees of freedom possible then the neutrino may cause transitions to such states. The new states may then decay weakly to (among other things) a muon. Therefore neutrino events with a second muon in the final state are potentially very interesting. The Fermilab fifteen-foot bubble chamber with its ability to record the details of the hadronic final state, the new two-plane External Muon Identifier (EMI) and the high energy quadrupole-triplet neutrino beam are well suited for the exploration of such phenomena.

1.1. WEAK INTERACTIONS

In 1938 E. Fermi [1], in analogy with the successful theory of Quantum Electrodynamics (QED), attempted to describe β decay with a current-current form for the weak interaction Lagrangian,

$$L_{int} = \frac{G}{\sqrt{2}} \bar{J}_h J_l$$

where,

$$G = Fermi\ constant$$

$$J_h = hadronic\ current$$

$$J_l = leptonic\ current$$

A pictorial representation (Feynman diagram) for the four-fermion interaction $n \rightarrow p\ e^-\ \bar{\nu}_e$ is shown in figure 1.1. The Fermi theory was extended and generalized by others and, in particular to explain parity violations in weak decays, the V-A theory [3,4] assumed the lepton current had a (polar vector)-(axial vector) spatial structure. However

the theory suffered from the fundamental problems that it was phenomenological and gave infinities for higher order processes.

Again the analogy with QED proved useful. QED was a finite theory because it was a gauge theory, i.e. invariant under arbitrary phase transformations at any point, and the carrier of the force was the zero-mass gauge boson, the photon (γ). An example of a QED process is $e\,e \rightarrow e\,e$ scattering (figure 1.2). The Weinberg-Salam unified gauge theory of weak and electromagnetic interactions [5,6] assumes the carriers of the forces are the isosinglet B^0 (the "primordial photon") and the W^+ and W^- (the mediators of the weak charged current (CC) interactions, e.g. muon decay as in figure 1.3). Isospin gauge invariance requires the existence of the W^0 which gives rise to the weak neutral current (NC) interaction.

In weak interactions the range of the force is extremely small so the W's must be massive. The problem of how to give the W's mass and still keep the theory finite was solved by the mechanism of spontaneous symmetry breaking. This has the effect of mixing the B^0 and the W^0 to get the physical particles: the massless γ and the massive Z^0. The advent of high energy and high intensity neutrino beams made possible the discovery of neutral current interactions in 1974 [7,8]. An example of a NC reaction is $\nu_\mu\, e^- \rightarrow \nu_\mu\, e^-$ scattering for which the Feynman diagram is shown in figure 1.4.

In this model the group which represents the QED interaction is U(1), and the group which represents the weak interaction is SU(2): the unification of the two interactions is represented by the group SU(2) X U(1).

To classify the leptons with respect to weak isospin the Weinberg-Salam model puts the right-handed parts of the leptons in isosinglets and the left-handed parts in isodoublets,

$$\begin{bmatrix} \nu_e \\ e^- \end{bmatrix}_{LH}, \quad \begin{bmatrix} \nu_\mu \\ \mu^- \end{bmatrix}_{LH}, \quad \ldots$$

where LH = left-handed.

1.2. QUARKS

Prior to 1974 all the known hadrons could be assumed made out of three fundamental constituents the up (u), down (d), and strange (s) quarks [9]. For example the proton is made of the three valence quarks uud; the π^+ meson is a $u\bar{d}$ pair. The properties of the three "ordinary" flavors of quarks are listed in the first three columns of the following table

Table 1.1 Quark Properties

flavor	u	d	s	c
charge	2/3	-1/3	-1/3	2/3
isospin	1/2	-1/2	0	0
strangeness	0	0	-1	0
charm	0	0	0	1

The quarks are arranged in the weak isodoublet

$$\begin{bmatrix} u \\ d' \end{bmatrix}_{LH}$$

where $d' = d\cos\theta_c + s\sin\theta_c$ and $\sin^2\theta_c = 0.05$. The reason for mixing d and s is to correctly describe the ratio of strangeness changing CC reactions (e.g. $K \rightarrow \mu\,\nu$) with respect to non-strangeness changing CC reactions (e.g. $\pi \rightarrow \mu\,\nu$), which is of order $\tan^2\theta_c$ [10]. This arrangement, however predicts a strangeness changing neutral current proportional to $\sin\theta_c\cos\theta_c$ [11]: unfortunately the experimental upper limit on strangeness changing NC's is several orders of magnitude lower than this prediction [12,13].

1.3. GIM MODEL AND CHARM

The Glashow-Illiopoulis-Maiani (GIM) mechanism [14] cancels the strangeness changing NC by introducing a fourth quark which is in the weak isodoublet

$$\begin{bmatrix} c \\ s' \end{bmatrix}_{LH}$$

where $s' = s\cos\theta_c - d\sin\theta_c$. The properties of the c quark are listed in the last column of table 1.1. Since the discovery in 1974 of the J/ψ meson [17,18] (a $c\bar{c}$ pair) and the discovery in 1976 of the D meson [19,20] ($c\bar{d}$) the existence of charm has been well documented in e^+e^- annihilation. Further evidence for charm came from neutrino events with two oppositely charged leptons and a strange particle in the final state [24,25].

1.4. SCATTERING KINEMATICS

The weak charged current may be written [15]

$$J_\lambda = \bar{\nu}_e\gamma_\lambda(1-\gamma_5)e + \bar{\nu}_\mu\gamma_\lambda(1-\gamma_5)\mu$$

$$+ \bar{u}\gamma_\lambda(1-\gamma_\lambda)d' + \bar{c}\gamma_\lambda(1-\gamma_5)s'$$

and for $Q^2 << (mass\ W)^2$ (where Q^2 is defined below) the charged current interaction Lagrangian is

$$L_{int} = \frac{G}{\sqrt{2}} \bar{J}_\lambda J_\lambda$$

For neutrino-lepton scattering (e.g. $\nu_\mu e^- \rightarrow \mu^- \nu_e$ shown in figure 1.5) the cross section is easily derived by standard techniques [15]

$$\frac{d\sigma}{dy} = \frac{G^2}{\pi} s$$

where $y = 2Q.P/s$, s = center of mass energy, Q = $(P_\nu - P_\mu)$ and P_ν, P_μ and P are the four-momenta of the incoming neutrino, outgoing muon and target lepton, respectively. For the antineutrino process $\bar{\nu}_\mu e^- \rightarrow \mu^+ \nu_e$ the cross section is

$$\frac{d\sigma}{dy} = \frac{G^2}{\pi} s (1-y)^2$$

If, as in the quark-parton model [16] the nucleon is made up of free structureless spin-1/2 quarks then the cross section for ν-N scattering should be similar to the ν-lepton cross sections

$$\frac{d\sigma^{\nu N}}{dxdy} = \frac{G^2}{\pi} s x \left[d(x) + \bar{u}(x)(1-y)^2 \right]$$

and

$$\frac{d\sigma^{\bar{\nu} N}}{dxdy} = \frac{G^2}{\pi} s x \left[u(x)(1-y)^2 + \bar{d}(x)2 \right]$$

where θ_c is approximated as zero, u(x), d(x), $\bar{u}(x)$, and $\bar{d}(x)$ are the number of ordinary quarks and antiquarks carrying nucleon momentum fraction x = $Q^2/2M\nu$, and ν = energy carried by the virtual W particle to the hadrons. The strong interactions ("gluon" exchange) between quarks have been ignored under the assumption that the time and

distance scale of the exchanged W is much smaller than the typical time and distance scale of the exchanged gluons. In this limit ($\nu, Q^2 \rightarrow \infty$) the process takes place in two phases: in the first phase the neutrino causes the transformation of a d into a u or a $\bar{u}$ into a $\bar{d}$ (the charge-conjugate reactions hold for antineutrinos); in the second phase the transformed quark dresses itself in the environment of the original hadron to produce the final state hadrons (see figure 1.6). Ordinary charged current cross sections show that the quark-antiquark sea is a few per cent of the valence quarks and peaked at low x.

1.5. POSSIBLE SOURCES OF DIMUON EVENTS

In ordinary CC events the neutrino is changed into a muon (if it is a muon-type neutrino) as in figures 1.5 and 1.6. However events with a second oppositely-charged lepton apparently from the primary vertex occur at $\approx 1/2\%$ of the single muon rate. Dimuon events have been studied by counter experiments since 1975 [21-23,50,51]. Bubble chambers, which (unlike counter experiments) can study the details of the final hadronic state, have looked at relatively lower energy μe events since 1976 [24-29]. At high energies it becomes difficult to determine whether or not electrons or positrons are produced at the primary vertex. Now with improved muon identification bubble chambers can study dimuons [30,31] making it possible to look at the hadronic state of high energy dilepton events.

The possible sources of dimuon events fall into five main categories.

first: The muons may result from the decay of a hypothetical heavy lepton produced as in figure 1.7a [31-33]. In this process one would expect that on the average the energies of the leptons would be equal. Indeed a calculation by Pais and Treiman has shown that $<E_{\mu_1}>/<E_{\mu_2}>$ should lie between 0.48 and 2.1 [34]. Experimentally the ratio is outside this range.

second: There may be a four-fermion process in the coulomb field of a proton as in figure 1.7b. The rate for this process should be down from the CC rate by a factor of the QED fine structure constant (1/137) squared and is therefore too low to explain the observed rate of about 1/2%. (The required Q^2 is too high for significant coherent nuclear contributions).

third: A neutral current event could have a $\mu^-\mu^+$ pair emerging from the hadronic sector as in figure 1.7c. Again one expects that $<E_{\mu_1}> \approx <E_{\mu_2}>$. Moreover dimuon production in hadronic collisions is at the 10^{-4} level so this is an unlikely explanation.

fourth: Production and decay of an intermediate vector boson (figure 1.7d) would be characterized by low energy transfer to the hadrons and a cross section that rises steeply with energy. However the mass of the W would have to be low and consequently propagator effects would have shown up in the single muon cross section. Again none of these predictions fit the data.

fifth: The most favored explanation of the source of dimuon events is the production of a charmed hadron (or possibly a hadron containing a newer and heavier quark). In the GIM model neutrinos interacting with nucleons can make dimuons in two ways. The first is where a valence d quark is transformed into a c quark and then dresses itself into a charmed hadron. The c quark in the charmed hadron then decays preferentially to an s quark and possibly a $\mu^+\nu$ pair as in figure 1.8a This rate is of order $d(x)\sin^2\theta_c$. The other process is where an $s\bar{s}$ pair from the sea is broken up as in figure 1.8b-- this should be of order $s(x)\cos^2\theta_c$ and result in two strange particles in the final state. Furthermore, sea quarks are alleged to inhabit the low x region so the cross section would be peaked at low x for charm production off the sea. (Since the c quark is massive one expects that there is no significant charm component to the sea: therefore charm production involving breakup of $c\bar{c}$ pairs is not considered).

Antineutrinos can make (anti) charm in only one way, breaking up an $s\bar{s}$ pair in the sea (of order $s(x)cos^2\theta_c$ where s(x) is of order 10% or less) giving two strange particles per event as in figure 1.8c. Again since production is off the sea the cross section should be peaked at low x. For both neutrino and antineutrino charm dimuon events the average y should be somewhat higher than for single muon events because of charmed quark mass threshold effects and because scattering is fermion-fermion or antifermion-antifermion . If the semileptonic branching ratio is $\approx$ 10% then the relative rate for charm dimuon events would be of order $(10\%)\sin^2\theta_c \approx 1/2\%$. A Monte Carlo program which simulates these processes for comparison with the data is described in appendix B.

(Two other models of charm production should be considered for completeness. First is associated production as shown in figure 1.9a and 1.9b. A struck quark radiates a gluon which then produces a $c\bar{c}$ pair. Clearly the energy threshold for this would be higher than for single charm production and the decays would give as many like-sign as opposite-sign dileptons: experimental data show the like-sign dilepton rate to be less than 10-20% of the opposite-sign rate. The other possibility is diffractive production of a charmed vector meson C^* as shown in figure 1.9c. The C^* would tend to emerge with most of the hadronic energy and therefore most of the visible hadronic energy would come from the products of the C^* decay. Note that the neutral current versions of the processes in figure 1.9 could produce dimuons if both $c\bar{c}$ decay to leptons.. however this is down from the CC process by an extra factor of the semileptonic branching ratio).

1.6. GOALS OF THIS THESIS

The goals of this thesis are to

1) study the dimuon production rate,

2) study the strange particle content of dimuon events,

3) study the kinematic properties of dimuon events, and

4) compare with the predictions of the charm and other models of section 1.5.

2. EXPERIMENTAL APPARATUS

The data for this thesis are from Fermi National Accelerator Laboratory experiment E546. Some of the distinctive features of E546 are the high energy spectrum of the quadrupole-triplet beam, good V^0 ($K_S^0 \rightarrow \pi^+ \pi^-$, $\Lambda^0 \rightarrow \pi\, p$) identification and the good high energy second lepton identification of the External Muon Identifier (EMI).

A schematic of the main ring, neutrino beam and bubble chamber/2-plane EMI plus IPF detector at Fermilab is shown in figure 2.1. The 400 Gev proton beam was extracted from the main ring of the accelerator and impinged on an alumina target. The spill duration was 2 milliseconds with 10^{13} protons per pulse for a total of 3.4×10^{18} protons on target. The secondaries of both signs were "focussed" by the quadrupole triplet of magnets and then allowed to coast down the 400 meter long decay pipe producing neutrinos and antineutrinos predominantly through the decay modes $\pi^+ \rightarrow \mu^+ \nu_\mu$, $\pi^- \rightarrow \mu^- \bar{\nu}_\mu$, $K^+ \rightarrow \mu^+ \nu_\mu$ and $K^- \rightarrow \mu^- \bar{\nu}_\mu$. The neutrino and antineutrino flux spectra from a Monte Carlo calculation [42] are shown in figure 2.2. A 1000 meter long earth shield removes everything but the ν_μ and $\bar{\nu}_\mu$ which then impinge on the bubble chamber/EMI detector which is shown in figure 2.3. In the bubble chamber the 30 kGauss magnetic field bends charged tracks (1 Gev/c $\approx$ 1 meter radius of curvature). The chamber was filled with 47% (atomic) Neon and Hydrogen for a density of 0.56 g/cm^3, a pion absorption length of 198 cm and a radiation length of 54 cm. Since the radius of the bubble chamber is 1.9 meter almost all of the gammas materialize and most of the hadrons interact in the chamber. Tracks that leave the chamber without interacting are either muons or hadrons. The 3-5 absorption lengths of magnet coil and zinc absorber remove all but a few per cent of the leaving hadrons before the first plane of EMI multi-wire proportional chambers (MWPC). Essentially all of the remaining hadrons interact in the next 4-7 absorption lengths before they can reach the second plane of EMI MWPCs. A muon is then a leaving noninteracting track ($\equiv$ LT) whose position in the EMI (predicted from the bubble chamber measurements) matches closely the position reconstructed from the EMI data.

A simplified schematic of an EMI MWPC and associated electronics is shown in figure 2.4. There are three coordinate planes x,y and the diagonal u which read out into delay lines. The time for the signal to arrive at the ends is a measure of the position of the particle that passes through the MWPC. For this experiment the old one-plane EMI [35] was expanded and reconfigured [36]. The new chambers have an amplifier on each end of the delay lines, the diagonal delay lines on the old chambers have amplifiers on only one end. A delay signal is read out of each delay line amplifier and in addition a prompt signal is recorded so that an ideal solution has a total of 7 measured times on the new MWPCs and 6 on the old MWPCs. Since there are three things to be determined (x, y and t) the new MWPCs get up to 4-constraint solutions and the old MWPCs get up to 3-constraint solutions for the coordinates of a given track.

One of the main virtues of two planes is that the solutions in one plane must be at the same time as the solutions in the other plane so that out-of-time background from other events is eliminated. The time difference between plane-2 and plane-1 EMI solutions for a sample of muons from CC events is histogrammed in figure 2.5. For this experiment two solutions are defined to be simultaneous if they are within 10 clock counts (357 nanoseconds) of one another.

Also during this experiment a partial Internal Picket Fence (IPF) was tested [37] but it is not used in this thesis.

3. ANALYSIS PROCEDURE

The 326000 pictures (in three stereoscopic views) were scanned for leaving non-interacting tracks ($\equiv LTs$) which were then measured and reconstructed in the bubble chamber using the geometric reconstruction programs TVGP and HYDRA. Then the tracks were extrapolated through the magnetic field and absorber to the first and second planes of the EMI by program XTRAP and the predicted hit positions compared with the reconstructed hit from the EMI data found by program EMIKE.

The difference between predicted and measured coordinates in the horizontal and vertical plane are x_i and y_i, respectively where i = plane 1,2. A single plane confidence level can be constructed

$$CL_i = e^{-\frac{\chi_i^2}{2}}$$

where

$$\chi^2 = \frac{x_i^2}{\sigma_{x_i}^2} + \frac{y_i^2}{\sigma_{y_i}^2}$$

and σ_{x_i}, σ_{y_i} = the calculated uncertainties (errors) in the x and y directions respectively for plane i. At low momentum the errors are due mainly to multiple coulomb scattering in the absorber. At high momentum the errors are mainly due to a small contribution from film measurement error and MWPC resolution. The coulomb error is plotted as a function of inverse momentum in figures 3.1 and 3.2 for planes 1 and 2 respectively.

A four-variable confidence level can be constructed

$$CL_{12} = \left(1 + \frac{\chi^2}{2}\right) e^{-\frac{\chi^2}{2}}$$

where

$$\chi^2 = \chi_x^2 + \chi_y^2$$

and

$$\chi_x^2 = \left[\frac{x_1^2}{\sigma_{x_1}^2} - \frac{2C_x x_1 x_2}{\sigma_{x_1}\sigma_{x_2}} + \frac{x_2^2}{\sigma_{x_2}^2} \right] (1-C_x^2)^{-1}$$

$$\chi_y = \left\{ \chi_x \right\}_{with\ x \to y}$$

C_x = *correlation between* x_1 and x_2

C_y = *correlation between* y_1 and y_2

The number of muons versus confidence level should be flat between 0 and 1 but in practice there are contributions from wider gaussians of about 10% in each plane. This is probably due to other hits in the chamber smearing the wave forms on the delay lines, or reflections and amplifier cross-couplings. The actual forms used were

$$CL'_i = (1-\delta)\ CL_i + \delta \left[CL_i \text{ with } \sigma_{x_i}^2 \to \sigma'^2_{x_i} = \sigma_{x_i}^2 + 2.89\ cm^2 \right.$$

$$\left. \text{and } \sigma_{y_i}^2 \to \sigma'^2_{y_i} = \sigma_{y_i}^2 + 2.89\ cm^2 \right]$$

[35] and

$$CL'_{12} = (1-2\delta)\ CL_{12} + \delta \left\{ CL_{12\ broad\ 1} + CL_{12\ broad\ 2} \right\}$$

where

$$CL_{12\ broad\ i} = \left[CL_{12} \text{ with } \sigma_{x_i} \to \sigma'_{x_i},\ \sigma_{y_i} \to \sigma'_{y_i}, \right.$$

$$\left. C_x \to (\sigma_{x_i}/\sigma'_{x_i})C_x, \text{ and } C_y \to (\sigma_{y_i}/\sigma'_{y_i})C_y \right]$$

and $\delta = 10\%$. With these definitions the confidence level distributions are flat to within a few per cent (see section 5.2).

Dimuon candidates with $CL'_{12} > 1\%$ and P > 4 GeV/c for both muons and a potential length (distance along the beam from primary vertex to downstream bubble chamber wall) of more than 50 cm were then completely measured. For comparison purposes a random sample of single muon events with $CL'_{12} > 10^{-4}$, muon momentum > 4 GeV/c and potential length > 50 cm was also completely measured. The cuts were based in part on the background calculations in the next section.

4. BACKGROUND DIMUONS

The main background for dimuon events is single muon events with the false muon coming from π or K meson decay in flight or punchthrough (PT) of energetic hadron LTs.

4.1. π and K MESON DECAY

π and K mesons can decay in flight either in the bubble chamber or outside the chamber in the vacuum tank (everywhere else the absorber is too dense-- see figure 2.3). When the meson track and the decay muon trajectory line up the result can resemble a prompt muon from the primary vertex. This background is the most serious. Low momentum mesons are more likely to decay than high momentum mesons (because of time dilation at high momentum) but low momentum mesons are also more likely to fail the criteria for a good muon because the lab decay angle and change of momentum tend to be larger. Some factors which help to eliminate these false prompt muons are

1.) momentum cut

2.) visible momentum change (for decays in the chamber)

3.) visible kink on track (mainly K decays in the chamber)

4.) poor match with EMI hits

Most decays are inside the bubble chamber and in these events the π (or K) and decay μ form a single composite track which is measured and processed by the geometry reconstruction program. Since it was not known a priori how the composite track would be handled by geometry it was necessary to simulate the decays in a Monte Carlo calculation.

The actual positions and momenta of the LTs from 289 μ^+ and 1587 μ^- events were used in a Monte Carlo of decays inside the bubble chamber. For each LT in the event (excluding the primary muon) a simulated track was allowed to decay according to the

expected π and K decay probability distribution. The simulated film point measurements were then processed through TVGP as a single track and then extrapolated to the EMI by XTRAP. The exact path of the true muon from the decay was also extrapolated to the EMI (see figure 4.1) and the hit was jiggled around to simulate coulomb scattering and the other errors. The effects of film measurement error and coulomb scattering in the liquid were also randomly generated by the simulation program. The Monte Carlo was tested by requiring that the confidence levels on non-decayed tracks be flat. A final weight was applied to each decay to correct for 1.)longer tracks in the LT sample being more likely to interact (and are hence under-represented) and 2.)the longer tracks in the sample may have a small contamination of decays [see appendix A].

Assuming 5% of the LTs are protons and 6% are kaons [38] the background estimates for the decays in the bubble chamber for the sub-sample are shown in table 4.1 [45].

Table 4.1 Decay Background in 289 μ^+, 1587 μ^- events

	$CL'_{12} > 0.01$	$CL'_{12} > 0.05$
	P(composite) > 4 GeV/c	
$\mu^-\mu^-$	0.66 events	0.57 events
$\mu^-\mu^+$	1.84	1.61
$\mu^+\mu^-$	0.15	0.14
$\mu^+\mu^+$	0.17	0.14
	P(composite) > 6 GeV/c	
$\mu^-\mu^-$	0.47	0.42
$\mu^-\mu^+$	1.20	1.01
$\mu^+\mu^-$	0.11	0.10
$\mu^+\mu^+$	0.07	0.06

The results for the total sample for decays in the bubble chamber plus the estimates for decays outside the chamber from another Monte Carlo [43] are displayed in table 4.5.

The estimated error in the decay background is $\approx$20% and comes from the uncertainty in the π/K interaction process at low momentum, uncertainty in the proton and K content of the LTs, and uncertainty in the uniformity of track measurement.

4.2. PUNCHTHROUGH

The number of hadrons that would pass through the 7-11 absorption lengths to the second plane without interacting is completely negligible, however the products of secondary interactions in the absorber and delta rays from the primary muon may register extra hits in the EMI giving matches with the extrapolations of LTs. A Monte Carlo program [41] capable of simulating hadronic cascades was modified for this experiment. This program includes essentially all of the processes that would produce charged particles that would trigger the EMI MWPCs. However the program, which follows the hadronic shower until each product is absorbed or hits the second plane of the EMI, is quite expensive to run.

In order to reduce computing costs only LTs with hits in the first plane are run through the Monte Carlo calculation. The magnetic field between planes is sufficiently small that bending is negligible compared with the angles in hadronic interactions consequently the field is set to zero. In Monte Carlo runs of 6,10,15,25 and 40 GeV/c, pions were started at the middle of the first plane. The number of hits in the second plane is plotted versus the distance r from the point where the pions would hit if there were no absorber. The distribution is roughly linear in r out to 60 cm or so (this implies a flat χ_I^2 distribution) after which it is flat for a while then drops off slowly. The density of hits, ρ, per starting pion is shown in the last column of table 4.2.

Table 4.2 Punchthrough Density in Plane-2 (r<60 cm)

P(GeV/c)	No. pions	No. hits	ρ (10^{-5} per cm^2)
6	1042	16	0.14
10	467	30	0.57
15	334	121	3.20
25	189	130	6.08
40	116	160	12.20

The density of hits due to spray from other tracks in the event can be calculated as follows: in 2548 CC events there were 10 tracks with matches ($CL'_2 > 0.01$) in the second plane but not in the the first plane. Dividing the number of matches by the area ($1.37\times10^6 cm^2$) we get a contribution of 0.73×10^{-5} *per* cm^2 per CC event. The actual EMI data can also be used to determine ρ (although dimuons and π/K decays must be subtracted and statistics are poor) and it is in good agreement with the Monte Carlo ρ [44].

To complete the punchthrough background calculation the actual positions and momenta of LTs with plane-1 matches from a sample of 2358 μ^- events and 370 μ^+ events were used. In the sample there were 37 LTs with $P > 4$ GeV/c and a hit in plane-1 (only) giving a match with $CL'_1 > 10^{-5}$ (matches with the primary muon's plane-1 hit are excluded). For each such track the punchthrough was simulated by Monte Carlo using the coordinates of the plane-1 hit and the coordinates of fake hits randomly generated using the previously determined values of ρ. The numbers of expected punchthrough events in the sample passing the cuts are displayed in table 4.3.

Table 4.3 Punchthrough Background in 370 μ^+, 2358 μ^- events

	$CL'_{12} > 0.01$	$CL'_{12} > 0.05$
	P > 4 GeV/c	
$\mu^-\mu^-$	0.55 events	0.27 events
$\mu^-\mu^+$	0.87	0.39
$\mu^+\mu^-$	0.24	0.13
$\mu^+\mu^+$	0.07	0.03
	P > 6 GeV/c	
$\mu^-\mu^-$	0.31	0.12
$\mu^-\mu^+$	0.52	0.22
$\mu^+\mu^-$	0.11	0.05
$\mu^+\mu^+$	0.02	0.003

The final punchthrough (PT) rates normalized to the total sample are displayed in table 4.5 at the end of section 4.4 [46].

The estimated error in the punchthrough is $\approx$40% and is due to the uncertainty in evaluating the contribution to the density from sources other than the track that punches through, and from the uncertainty in the momentum of the track at the first plane.

4.3. ACCIDENTALS

In principle, events in the absorber within the allowed time interval may have solutions in the EMI that match with an extrapolated LT. In order for a hit in plane-1 and a hit in plane-2 to form a match not only must the hits be in the right spatial positions (close to the extrapolated track) but also within the same 10 clock count interval as the primary muon time (10 clock counts = 357 nsec). To estimate the accidental background we looked for "dimuons" where the second muon "candidate" had its EMI hits in a 10 count interval displaced to a much earlier time. We conclude that the accidental background is totally negligible.

4.4. FAKE DIMUON EVENT SAMPLE

In the following sections it will be useful to have a representative sample of complete background events. This was obtained in the following way: each event in the random sample was weighted by the probability that it could give rise to a background dimuon event. This probability was calculated by summing over the LTs in the event (requiring P > 4 GeV/c and aimed at the EMI) the probability that a track of that particular momentum and length could fake a muon. This background probability per LT was obtained from a distillation of the π/K decay and punchthrough Monte Carlo data and is displayed in table 4.4 below.

From table 4.4 we see that the probability per LT of decays in the bubble chamber increases with track length: this increase is to compensate for the depletion of long length

LTs due to interactions. Also note that the decrease in probability at large momentum is because of time dilation, whereas the low probability at low momentum is due to the better rejection efficiency there. Studies of punchthrough (PT) of solitary hadrons indicate that the rise of PT density with momentum is roughly compensated by the fall with momentum of the coulomb scattering ellipse so that PT is flat with momentum [41]. However in this experiment there is an initial drop off of punchthrough at low momentum because of the constant contribution to the density due to spray from other tracks in the event. At high momentum there is a slow rise in punchthrough because of the constant term 2.89 cm^2 added in quadrature to the coulomb scattering error.

Table 4.4 Fake Muon Background Probability (% per LT)

L(cm)	P(GeV/c) = 4-6	6-8	8-12	12-20	20-
	decays in bubble chamber				
50-90	0.06	0.19	0.18	0.09	0.04
90-130	0.20	0.26	0.19	0.15	0.07
130-170	0.36	0.39	0.27	0.30	0.13
170-230	0.44	0.50	0.53	0.29	0.17
230-	1.23	1.22	0.78	0.63	0.38
	decays outside chamber				
50-	0.15	0.09	0.08	0.06	0.03
	punchthrough				
50-	0.29	0.06	0.05	0.10	0.17

To complete the transformation of a random sample event into a fake dimuon event a fake secondary muon was chosen randomly from the LTs consistent with the probability distributions in table 4.4.

The fake dimuon sample was then normalized to the total expected background using table 4.5 below (each of these background rates is normalized to the number of [$\nu_\mu N \rightarrow \mu^- X + \bar{\nu}_\mu N \rightarrow \mu^+ X$] events).

Table 4.5 Total Dimuon Background (% per single-muon event)

	$\mu^-\mu^-X$	$\mu^-\mu^+X$	$\mu^+\mu^-x$	$\mu^+\mu^+X$
decays in chamber	0.035	0.099	0.008	0.009
decays outside	0.009	0.024	0.002	0.002
punchthrough	0.020	0.031	0.008	0.002
Total	0.064	0.154	0.018	0.013

5. DETECTOR EFFICIENCY

Muon candidates may be lost at the scan stage or by EMI inefficiency (geometrical and instrumental). K_S^0's and Λ^0's may be lost if they interact in the bubble chamber or escape without decaying inside the bubble chamber. Energy may be lost if neutral particles leave the bubble chamber without interacting or decaying.

5.1. SCAN EFFICIENCY

The efficiency for finding CC events and measuring the right number of leaving tracks was found by comparing the results of two separate scans of the same film. The average scan efficiency for finding a CC event is $ESEV = 95\pm3\%$ [53]. The average efficiency for recording and measuring the secondary muon candidate LTs in the event is $ESLT = 95\pm3\%$ per LT (the loss is due mainly to messy events with many tracks and events low down in the bubble chamber where visibility is poor. The total scan and measure efficiency is therefore $ES1 = ESEV = 95\%$ for single muon events and $ES2 = (ESEV)(ESLT) = 90\%$ for opposite-sign dimuon events.

5.2. EMI EFFICIENCY

Because of the limited geometric extent of the EMI, events with muons of low momentum and wide angles (with respect to the beam) may be missed. In order to correct for the fact that geometric efficiency varies from event to event an average weight (inverse efficiency) is computed by randomly moving the actual events around in the bubble chamber (requiring the primary vertex to be in the fiducial volume and visible in all three film views), rotating the event randomly around the beam axis, and extrapolating the muon(s) to the EMI. The distribution of EMI geometric weights for single- muon events is shown in figure 5.1. The averages of these weights are $WGM = 1.12\pm0.01$, $WGP = 1.11\pm0.01$ for μ^- and μ^+ events, respectively. The distribution of weights for

the opposite sign dimuon candidates is shown in figure 5.2 and the average weight is $WGPMC = 1.34 \pm 0.01$; however this includes the background events. From the distribution of weights for the fake dimuon sample shown as a smooth curve in figure 5.2 one finds that the average weight is $WGPMB = 1.38 \pm 0.01$, (this is higher than the weight for the dimuon candidates because the momentum of the fake secondary muons is slightly lower than the momentum of the real muons). The average EMI geometric weights are sumarized in table 5.1 below (see section on rates for separation of dimuons by sign).

Table 5.1 Average EMI Geometric Weights

	μ^-	μ^+	$\mu^-\mu^+$	$\mu^+\mu^-$	$\mu^-\mu^+ + \mu^+\mu^-$
candidates	1.12	1.11	1.22	1.87	1.34
background	--	--	1.34	1.63	1.38

The instrumental efficiency of the EMI is a measure of how likely the EMI (including electronics and software) can detect a muon that is aimed at it. A fairly pure sample of muons can be obtained from the neutrino events in the earth shield upstream of the bubble chamber. A sample of muons that entered the bubble chamber from the upstream end was used to calculate the EMI instrumental efficiency. The average efficiency of an EMI MWPC for EMIKE solutions with at least one constraint is $91\pm2\%$. For single muons, where it was required that the EMIKE solution in each plane have at least one constraint, the instrumental efficiency is estimated to be $EI1 = 83\pm2\%$; for dimuons the instrumental efficiency is $EI2 = 96\pm3\%$ (this is somewhat higher than the single muon efficiency because EMIKE solutions with zero and -1 constraints were allowed for one of the muon's solution if it was consistent with the time of the other muon-- the MWPCs are essentially 100% efficient when 0 and -1 constraint solutions are used).

From the confidence level distribution of the same sample of through-muons used for the instrumental efficiency study it is estimated that the cut $CL'_{12} > 0.01$ results in an efficiency of $ECL = 95\pm2\%$ per muon.

5.3. V^0 DETECTION EFFICIENCY

K_S^0's or Λ^0's that interact before they can decay will be lost. Decays too close to the primary vertex, too near or outside the downstream bubble chamber wall will be lost. A K_S^0 or Λ^0 is less likely to decay in the bubble chamber if it has high momentum or the primary vertex of the event is near the downstream wall. On the other hand downstream events are more more likely to be detected by the EMI because of its larger solid angle there. Thus V^0 detection efficiency is coupled with EMI geometric efficiency. To correct for these effects a weight was computed for each event in the following way. Each event was moved about the bubble chamber in a manner similar to the EMI geometric efficiency calculation. If at a given point in the bubble chamber the muon(s) extrapolated to the

EMI then the probability that the K_S^0 or Λ^0 would decay in the chamber more than 0.5 cm from the primary vertex and less than 20 cm from the downstream wall is

$$P_{V^0} = \left[\frac{1}{\alpha\gamma\beta c\tau} \right] \left(e^{-0.5\alpha} - e^{-(L-20)\alpha} \right)$$

where

L = *distance from primary vertex to wall*

$$\alpha = \frac{1}{\gamma\beta c\tau} + \frac{1}{\lambda}$$

λ = *absorption length*

γ, β = *Lorentz factors*

If either muon missed the EMI, zero was summed. (The scan efficiency for V^0's more than 0.5 cm from the primary vertex and less than 20 cm from the wall is 100%). The weight for the event was then the value of the summed quantity divided into the number of times the event was moved around. The EMI geometric/V^0 detection weight distributions for the single-muon, dimuon and fake dimuon events are shown in figure 5.3, 5.4 (histogram), and 5.4 (smooth curve) respectively. The average of the weight over the events was $WGVM = 1.52 \pm 0.01$, $WGVP = 1.41 \pm 0.01$ and $WGVPMC = 2.41 \pm 0.01$ for the $\mu^- V^0 X$, $\mu^+ V^0 X$, and opposite sign dimuon/V^0 candidates, respectively. For the fake dimuon sample the average weight was $WGVPMB = 1.57 \pm 0.01$ which is lower than $WGVPMC$ (in spite of the fact that the EMI geometric weight is higher for the fakes) because the average momentum of the background V^0's is considerably lower than the average momentum of V^0's in the dimuon candidate events.

5.4. CALORIMETRIC EFFICIENCY

Energy may be lost when neutral particles exit the bubble chamber without interacting or decaying to produce charged particles. Studies of a 25 GeV π^- beam run show that the bubble chamber detects about 87% of the hadronic energy on the average [56].

One possible method of correcting for the energy loss would be to scale the hadronic energy by a constant factor for each event. However if the dimuons are from charm decay then they may be missing additional energy in the form of a neutrino (and hence have a different calorimetric efficiency than single muon events). Furthermore the calorimetric efficiency may couple with the EMI geometric efficiency for the same reason the V^0 detection efficiency does. Therefore a method of missing energy correction based on the individual event transverse momentum imbalance was used. In this method [39] it is assumed that for hadrons the ratio of unseen to seen longitudinal momentum is equal to the ratio of unseen to seen transverse momentum. The hadronic energy is therefore scaled by the factor

$$G = 1 + \frac{P_u^{T\nu}}{P_s^{T\nu}}$$

$$where \quad P_s^{T\nu} = \sum_{i=seen\ hadrons} \left| \vec{P}_i^{T\nu} \right|$$

and $\vec{P}_i^{T\nu}$ = momentum of i^{th} hadron transverse to the neutrino beam and

$$P_u^{T\nu} = \sum_{i=unseen\ hadrons} \left| \vec{P}_i^{T\nu} \right| \approx \left| \sum_{i=unseen\ hadrons} \vec{P}_i^{T\nu} \right|$$

The last term is the missing momentum transverse to the incident neutrino direction. Because of the triangle inequality the last approximation means the correction factor is a slight underestimate on the average.

6. RELATIVE RATES

6.1. DIMUON EVENTS

We have a total of 10148 $\mu^- X$ and 1773$\mu^+ X$ events with $CL'_{12} > 0.0001$ and muon momenta > 4 GeV/c. The numbers of dimuon events with both muons satisfying $CL'_{12} > 0.01$ and momentum > 4 GeV/c in the sample are displayed in table 6.1 along with the expected backgrounds.

Table 6.1 Dimuon Events

	$\mu^-\mu^+X + \mu^+\mu^-X$	$\mu^-\mu^-X$	$\mu^+\mu^+X$
candidates	55	11	0
background	$20^{+}_{-}5$	$8^{+}_{-}3$	$1^{+}_{-}1$

The like-sign events are consistent with being background. With the definitions of sections 5.1 and 5.2 we calculate the beam-averaged rate

$$R_{\mu\mu} = \frac{(\nu_\mu N \rightarrow \mu^- \mu^+ X) + (\bar{\nu}_\mu N \rightarrow \mu^+ \mu^- X)}{(\nu_\mu N \rightarrow \mu^- X) + (\bar{\nu}_\mu N \rightarrow \mu^+ X)}$$

$$= \frac{\left[\frac{(\mu\mu X \text{ candidates})\ (WGPMC) - (\mu\mu X \text{ background})\ (WGPMB)}{(ESLT)\ (ECL)\ (ECL)\ (EI2)}\right]}{\left[\frac{(\mu^- X)\ (WGM) + (\mu^+ X)\ (WGP)}{(EI1)}\right]}$$

$$= 0.35\% \pm 0.10\% \text{ per single muon event}$$

for muon momenta > 4 GeV/c.

In neutrino events the hadrons tend to recoil opposite to the direction of the primary muon (see figure 1.6) so that the track with the highest P^{Tr} = momentum transverse to the neutrino beam or the highest P^{Th} = momentum transverse to hadron jet tends to be the primary muon. To further separate the ν-induced dimuons from the $\bar{\nu}$-induced dimuons the primary muon is defined to be the muon with the highest P^{Th}. This is reasonable if the second muon is of hadronic origin. Figures 6.1a and 6.1b show plots of $P^{Tr}_{\mu_2}$ versus $P^{Tr}_{\mu_1}$ for $\mu^- \mu^+ X$ (henceforth writing negative muon first implies a ν-induced event) and $\mu^+ \mu^- X$ ($\bar{\nu}$-induced) events respectively. Figures 6.2a and 6.2b show plots of $P^{Th}_{\mu_2}$ versus $P^{Th}_{\mu_1}$ for $\mu^- \mu^+ X$ and $\mu^+ \mu^- X$, respectively. Clearly the separation is cleaner because there are fewer points near the diagonal line $P^{Th}_{\mu_1} = P^{Th}_{\mu_2}$. With this definition we find 46 $\nu N \rightarrow \mu^+ \mu^- X$ and 9 $\bar{\nu} N \rightarrow \mu^+ \mu^- X$ candidates. The numbers of candidates and the expected background are summarized below in table 6.2 [40].

Table 6.2 Dimuon Events Separated by Sign

	$\nu_\mu N \rightarrow \mu^- \mu^+ X$	$\bar{\nu}_\mu N \rightarrow \mu^+ \mu^- X$
candidates	46	9
background	17 ± 3	3 ± 1
crossover	-2 ± 1	$+2 \pm 1$

The relative rates then are

$$R_{\mu^-\mu^+} = 0.32\% \pm 0.15\% \; per \; \mu^- X$$

$$\text{and} \;\; R_{\mu^+\mu^-} = 0.49\% \pm 0.30\% \; per \; \mu^+ X$$

Breaking at 100 GeV we find $R_{\mu^-\mu^+}$ $(E_{\nu_\mu} < 100 \; GeV) = 0.20 \pm 0.15\%$ and $R_{\mu^-\mu^+}$ $(E_{\nu_\mu} > 100 \; GeV) = 0.50 \pm 0.30$ (much of this rise may be from the 4 GeV/c muon momentum cut).

6.2. DIMUON EVENTS WITH V^0s

In the 53 $\mu^+\mu^- X$ candidates there were 10 V^0 candidates. The V^0's were kinematically fit by program SQUAW. The results of the 3-constraint fits and the EMI(geometric)/V^0 detection efficiency weight for each candidate are shown in table 6.3 [52].

Table 6.3 Dimuon + V^0 Candidates

event	K_S^0-fit χ^2	Λ^0-fit χ^2	P(fitted)	weight	mass(μ_2, V^0)
14730594($\mu^-\mu^+$)	3.2	--	12.8	1.4	1.4
14791740($\mu^-\mu^+$)	4.7	--	39.4	2.7	1.4
15101414($\mu^-\mu^+$)	--	2.5	0.5	1.3	6.5
15560114($\mu^-\mu^+$)	0.1	1.7	54.5	2.9	1.7
15690673($\mu^+\mu^-$)	0.8	--	6.1	1.4	1.9
15761797($\mu^-\mu^+$)	0.7	--	12.9	3.2	1.0
16051203($\mu^-\mu^+$)	0.2	--	2.2	0.0	1.3
16420642($\mu^-\mu^+$)	0.8	--	2.8	2.3	1.0
16460680($\mu^-\mu^+$)	1.9	17.8	3.1	1.6	1.1
16511246($\mu^-\mu^+$)	--	11.6	3.7	1.5	2.6

With the definitions of section 5.2 and 5.3 the relative dimuon + V^0 rate is

$$R_{\mu\mu V^0} = \frac{(\nu_\mu N \rightarrow \mu^- \mu^+ V^0 X) + (\bar{\nu}_\mu N \rightarrow \mu^+ \mu^- V^0 X)}{(\nu_\mu N \rightarrow \mu^- \mu^+ X) + (\bar{\nu}_\mu N \rightarrow \mu^+ \mu^- X)}$$

$$= \frac{(\mu\mu V^0 \text{ candidates})\ (WGVPMC)) - (\mu\mu V^0 \text{background})\ (WGVPMB)}{(\mu\mu X \text{ candidates})\ (WGPMC) - (\mu\mu X \text{ background})\ (WGPMB)}$$

From the fake dimuon sample we expect $3.1\pm.4$ weighted $K_S^0 \rightarrow \pi^+\pi^-$ and 1.4 ± 0.3 weighted $\Lambda^0 \rightarrow p\pi$ in the background. Therefore putting the numbers in the equation above we get 0.26 ± 0.12 $K_S^0 \rightarrow \pi^+\pi^-$ and 0.04 ± 0.04 $\Lambda^0 \rightarrow p\pi$ per opposite sign dimuon event.

Correcting for branching ratios we get 0.78 ± 0.36 neutral kaon per opposite sign dimuon event. In contrast the charged current random sample has 0.15 ± 0.03 neutral kaon per event. (The Λ^0 rate of the dimuon sample is consistent with being equal to the expected background). If charged kaons are equal in number and momentum distribution to neutral kaons we conclude there are 1.6 ± 0.7 kaon per opposite sign dimuon event.

7. KINEMATIC DISTRIBUTIONS

In this section the kinematic distributions of the single-muon and opposite-sign dimuon events are presented. All histograms contain events weighted by the inverse of their individual EMI geometric efficiency, except histograms of quantities pertaining to V^0's which are weighted by their inverse EMI geometric/V^0 detection efficiency. Antineutrino-induced candidates are shaded. No correction is made to the data for the 4 GeV/c muon momentum cut. The average values of some kinematic variables of interest for single and dimuon events are displayed in table 7.1 below.

The equations used to calculate the kinematic variables are

$$E_\nu = P_\mu^{L\nu} + G\ P_H^{L\nu}$$

where G is defined in section 5.4 and

$$P_\mu^{L\nu} = \textit{component of primary muon momentum along neutrino direction}$$

$$P_H^{L\nu} = \textit{component of hadron system momentum along neutrino direction}$$

$$E_\mu = \textit{energy of primary muon}$$

$$\nu = E_\nu - E_\mu$$

$$Q^2 = 2E_\nu(E_\mu - P_\mu^{L\nu}) - m_\mu^2$$

$$W^2 = M^2 + 2\ M\ \nu - Q^2$$

$$M = .9383\ GeV/c^2$$

$$x = \frac{Q^2}{2\ M\ \nu}$$

and $y = 1 - E_\mu/E_\nu$.

TABLE 7.1 AVERAGES OF SOME KINEMATIC QUANTITIES

		P_{μ_1}	P_{μ_2}	E_ν	x	y	Q^2	W	ϕ	$P_{\mu_2}^{\perp \mu_1 \nu}$	$P_{K_S^0}^{\perp \mu_1 \nu}$	$M_{\mu_2 K_S^0}$
	μ^-	50.1 ±2.1	—	89.2 ±3.1	0.24 ±0.01	0.43 ±0.02	16.5 ±0.7	6.6 ±0.3	138 ±6	0.39* ±0.01	0.39* ±0.02	—
$\mu^-\mu^+$	Candidates	56.6 ±8.5	13.3 ±2.0	126.0 ±19.0	0.19 ±0.03	0.56 ±0.08	27.1 ±4.1	9.5 ±1.4	136 ±20	0.29 ± 0.04	0.28 ±0.04	1.25 ±0.04
$\mu^-\mu^+$	Monte Carlo	52.6 ±1.6	13.8 ±0.4	122.0 ±4.0	0.20 ±0.01	0.57 ±0.02	25.7 ±0.8	9.3 ±0.3	129 ±4	0.29 ±0.01	0.33 ±0.01	1.41 ±0.04
$\mu^-\mu^+$	Background	55.0 ±3.8	10.8 ±1.0	108.5 ±8.1	0.24 ±0.02	0.52 ±0.04	24.2 ±1.7	8.1 ±0.6	134 ±9	0.25 ±0.02	0.27 ±0.01	1.47 ±0.40
	μ^+	38.6 ±2.5	—	57.7 ±3.7	0.22 ±0.01	0.38 ±0.03	8.8 ±0.6	5.1 ±0.3	131* ±8	0.32* ±0.02	—	—
$\mu^+\mu^-$	Candidates	28.6 ±11.9	13.3 ±4.4	53.2 ±17.6	0.15 ±0.05	0.58 ±0.19	9.6 ±3.2	6.7 ±2.2	143 ±47	0.34 ±0.11	—	—
$\mu^+\mu^-$	Monte Carlo	28.0 ±1.9	14.2 ±1.0	64.0 ±4.5	0.15 ±0.01	0.59 ±0.04	15.7 ±1.1	8.6 ±0.6	126 ±9	0.30 ±0.02	—	—
$\mu^+\mu^-$	Background	30.1 ±4.5	12.4 ±1.8	79.9 ±11.9	0.14 ±0.02	0.62 ±0.09	13.0 ±2.0	8.5 ±1.3	113 ±17	0.36 ±0.05	—	—

*Computed using hadrons with P > 4 GeV/c and charge opposite primary muon.

Two other variables which are relevant to whether or not an individual hadron in an event is leading are the energy fraction

$$z = E/\nu$$

and the rapidity in the frame of the struck quark [55]

$$Y_q = 0.5 \ln \left[\frac{E + P^{Lh}}{E - P^{Lh}} \right] - \ln \left[W^2/M^2 \right]$$

where E = energy of track and P^{Lh} = component of track momentum along hadron jet (the hadron jet direction is determined by summing all the visible hadronic momenta, and in the case of dimuons the second muon is included in this sum).

7.1. SINGLE-MUON EVENTS

To calibrate the procedure and for later comparison with the dimuons, the kinematic distributions for the single-muon events are presented here. Antineutrino events are shaded on the histograms. Figure 7.1 shows the momentum spectrum of the primary muon. The smooth curve is the prediction for P_μ from a Monte Carlo (using the flux of reference [42] and a B parameter of 0.8), by M. L. Stevenson. Figure 7.2a(b) shows the visible (corrected) energy distribution. After correction for missing neutrals, the average energy for $\nu_\mu(\bar{\nu}_\mu)$ is 89(60) GeV. Figure 7.3a(b) shows the visible (corrected) $x = Q^2/2M\nu$ distribution. The visible (corrected) y distribution is shown in figure 7.4a(b). The neutrino y distribution is flatter than the antineutrino y distribution as expected. The depletion at high y is due to the 4 GeV/c cut on the primary muon (y_{max} = 1 - $4/E_\mu$). The efficiency due to this cut, calculated by Monte Carlo, is shown as the smooth curve (arbitrary units). The corrected Q^2 distribution is shown in figure 7.5, and the corrected W distribution is shown in figure 7.6.

The momentum spectrum of the V^0's is shown in figure 7.7a and 7.7b. In general the K_S^0's are faster than the Λ^0's and slightly more common.

The distribution of P^{perp}, the momentum perpendicular to the $\mu_1\nu$ plane is shown in figure 7.8a (positive hadrons) and figure 7.8b (negative hadrons). The z and Y_q distributions for hadrons are shown in figures 7.9ab and 7.10ab. The effects on the P^{perp}, z, and Y_q distributions when a 4 GeV/c momentum cut is made may be seen in figures 7.8cd, 7.9cd, and 7.10cd. The P^{perp}, z and Y_q distributions for V^0's (for all momenta) are shown in figures 7.8e, 7.9e and 7.10e. The variable ϕ may be defined as the azimuthal angle between two momentum vectors when viewed along the neutrino direction. The distribution of ϕ between hadrons (of sign opposite the primary muon and with momentum > 4 GeV/c) and the primary muon is shown in figure 7.11: the clustering at 180 degrees is typical of hadrons. (The variables P^{perp}, z, Y_q and ϕ for hadrons in ordinary events are interesting for later comparison with the distributions for the second muon in the opposite-sign dimuon candidates).

7.2. DIMUON EVENTS

In this section the kinematic distributions of the opposite-sign dimuon candidates are presented along with the predictions (for $\mu^-\mu^+$) of a charm production and decay Monte Carlo, (based on the fifth (GIM) model of section 1.5 and described in appendix B), and the expected $\mu^-\mu^+$ background. The dimuon candidates are in histogram format (unshaded = $\mu^-\mu^+$; shaded = $\mu^+\mu^-$). The charm Monte Carlo predictions, normalized to the (signal - background), are the smooth curves and the $\mu^-\mu^+$ background is in solid dots. The background predictions are based on the fake dimuon sample of section 4.4.

In figure 7.12 is shown the primary muon momentum distribution, (the bin at 170 GeV/c contains only 3 events which are well measured but have a momentum uncertainty of about 20 GeV/c; therefore the excess is probably a statistical fluctuation). Figure 7.13 has the secondary muon momentum: the ratio $<P_{\mu_1}>/<P_{\mu_2}>$ is 3.3 even when $P_{\mu_2} > 4$

GeV/c is required. Since the ratio is outside the range [.48 to 2.1] of the Pais-Treiman theorem heavy lepton production cannot contribute very much to the dimuon rate. Figure 7.14 shows a plot of P_{μ_1} versus P_{μ_2} the opposite-sign dimuon candidates. The majority of events have $P_{\mu_1} > P_{\mu_2}$. (Recall that μ_1 is the muon with greater P^{Th}, which will usually, but not always, be the muon with greater P).

Figure 7.15a(b) shows the visible (corrected) energy distributions. The average energy is 125 GeV for $\mu^-\mu^+$ events and 60 GeV for $\mu^+\mu^-$ events, higher than the average corresponding single- muon event energies. Some of this effect is due to the 4 GeV/c secondary muon momentum cut but charm production threshold effects may also play a role.

Figure 7.16a(b) shows the visible (corrected) x distributions. The $\mu^+\mu^-$ x-distribution is concentrated at slightly lower x than the $\mu^-\mu^+$ x-distribution. In the charm model antineutrinos can make charm only off sea quarks which are at lower x than valence quarks.

The visible (corrected) y distributions are shown in figures 7.17a(b). The dimuon candidates, background, and charm Monte Carlo have a higher average value of y than the single-muon events. In the background and Monte Carlo events this is due to the 4 GeV/c cut on the secondary muon candidate: the Monte Carlo has an additional concentration at high y due to the charm threshold. The data show slightly more events at low y than would be expected from (background + Monte Carlo): this has also been observed in reference [50].

The corrected Q^2 distribution is shown in figure 7.18. The dimuons are distributed more broadly than the single-muon events in this variable presumably because they are at higher energy. The corrected invariant mass W of the hadron system is shown in figure 7.19. In the dimuon candidates W tends to be larger than the single-muon events: both the background and the Monte Carlo display a similar effect. The 4 GeV/c cut on the secondary muon candidate favors higher W for both background and Monte Carlo, with

the Monte Carlo there is an additional increase of W due to the charm production threshold effect.

The momentum of the primary muon transverse to the hadron jet (shown in figure 7.20) tends to be quite large and is consistent with its selection as the primary muon. The momentum of the second muon transverse to the hadron jet (figure 7.21) gives a clue to its origin. If the muon results from the semileptonic decay of a massive hadron then the transverse momentum can be no larger than half the decaying hadron mass. The transverse momentum of muon-2 is always less than 1.5 GeV/c and peaks around 500 MeV/c. The background (which is of hadronic origin) shows similar behaviour but peaks slightly lower. Some of the spread of the distribution is due to missing neutrals, to Fermi motion of the struck nucleon in the parent nucleus and analogous motion of the struck quark in the parent nucleon (or perhaps QCD effects). A variable which is independent of momentum balance is the component of the secondary muon momentum out of the $\mu_1\nu$ plane shown in figure 7.22 (compare with the corresponding CC distribution in figure 7.8). If the second muon is from the decay of a hadron this hadron cannot be much heavier than 2 GeV/c^2. (A slight depletion of the $\mu^-\mu^+$ data at high transverse momentum is expected due to the cross-over events).

From the z (figure 7.23) and Y_q (figure 7.24) distributions we see that there is agreement with the Monte Carlo prediction that the secondary muon is relatively leading, however comparison with figures 7.9 and 7.10 shows that ordinary hadrons above 4 GeV/c are also distributed similarly.

The azimuthal angle ϕ between the momentum vectors of the two muons when looking into the neutrino beam is shown in figure 7.25. It shows the same peaking at 180 degrees that the hadrons from the CC events do (see figure 7.11) implying the second muon has its origin in the hadronic jet. The invariant mass of the primary and secondary muons is shown in figure 7.26. It is broad (as is the background) showing that the primary muon and the secondary muon do not have the same origin, thereby ruling out heavy

lepton production and decay as the main source of dimuons.

The invariant mass of the V^0's with the secondary muon is shown in figures 7.27a and 7.27b. The mass($\mu_2 K_S^0$) distribution is consistent with the charm Monte Carlo. The momentum spectrum of the V^0's (figure 7.28a and 7.28b) is relatively hard compared to the momentum spectrum of the V^0's in the background dimuon and single-muon events (see figure 7.7a and b). The charm decay Monte Carlo indicates that the 4 GeV/c momentum cut on the second muon pushes up the average momentum of the strange particle by about 6 GeV/c.

P^{perp} for V^0's is shown in figure 7.29 and is consistent with the prediction of the charm Monte Carlo. The z and Y_q distributions for the V^0's are shown in figures 7.30 and 7.31: clearly the V^0 in the dimuon events tends to be "leading".

8. CONCLUSIONS

We have observed 55 events of the type $\nu_\mu(\bar{\nu}_\mu)\ N \rightarrow \mu^-\mu^+X(\mu^+\mu^-X)$ where we expect $20^{+}_{-}5$ due to background (mainly π/K decays). There are 10 neutral strange particles associated with these events where we expect $2^{+}_{-}1$ background.

We conclude by summarizing the evidence in favor of the charm model interpretation of the dimuons and argue against the alternate interpretations discussed in section 1.5. Additional inferences are drawn on the assumption of the validity of the charm model. Finally, comparison with the results of other experiments is made.

The first model of section 1.5, production and decay of heavy leptons is ruled out by the result $<P_{\mu_1}>/\ <P_{\mu_2}> \ = 3.3$ which is outside the range allowed by Pais-Treiman (even before correcting for the 4 GeV/c cut), the anticorrelation between the angle ϕ between the muons (figure 7.19) implying the second muon is associated with the hadrons, and the broad effective mass distribution of the primary and secondary muon (figure 7.20).

Four-fermion processes and neutral current events with a $\mu^+\mu^-$ pair emerging from the hadrons (the second and third models) are excluded because they predict a rate much lower than the experimentally observed rate (section 6.1) and because they predict little or no asymmetry in the momenta of the two muons (figure 7.10).

The fourth model, production and decay of an intermediate vector boson is ruled out because of the relatively high inelasticity of the events (figure 7.13) and because there is no evidence for a large energy dependence (compare figures 7.2 and 7.11).

On the other hand, the GIM charm model predictions fit the data well. We see a rate of $R_{\mu\mu} = 0.35^{+}_{-}0.10$ opposite sign dimuon events per single muon event (muon momenta > 4 GeV/c). Figures 7.17 and 7.18 show that the new hadron produced must have mass less than about 2 GeV/c^2, (and the mass$(\mu_2 K^0_S)$ distribution is also consistent with this). The D meson then is a prime candidate for the decay particle. Charm is

predicted to be produced in deep inelastic neutrino events at a rate of about 4 to 6 % (depending on the $s\bar{s}$ content of the sea [47]); if the semimuonic branching ratio is about 8% then we expect dimuon rate of about 0.3% to 0.5 %, in good agreement with our result. Furthermore the model predicts that most of the time charm will be accompanied by one or two strange particles per event (again depending on the strange content of the sea): from our observations and the assumptions of section 6.2 we deduce $1.6^{+}_{-}0.7$ strange particles per event. As we saw in section 7 the kinematic properties of the dimuons are in general agreement with the predictions of the charm production and decay Monte Carlo, (and there is no need to suspect NC production of $c\bar{c}$).

While in principle the measurement of $R_{\mu^-\mu^-}$ and $R_{\mu^+\mu^+}$ permit the determination of the strange quark content of the sea, the experimental error is too large because of the small number of $\mu^+\mu^-$ events.

Associated production of charm in CC events can be ruled out as the source of most of the dimuons because the opposite sign events dominate the like sign events.

Since within the confusion distance of 5 mm we see no visible evidence for a separate decay vertex in any of the dimuon events we can put an upper limit on the lifetime of the decaying meson of a few times 10^{-12} sec [48].

The results of this experiment may be compared with ref. [30] (the Aachen-Bonn-CERN-London-Oxford-Saclay collaboration). Using the BEBC bubble chamber and a one-plane EMI they find (with poor statistics) a dilepton rate $R_{\mu\mu+\mu e} = 0.8^{+}_{-}0.3\%$ ($1.8^{+}_{-}0.6\%$) and a rather high neutral strange particle multiplicity of $1.7^{+}_{-}0.7$ ($1.0^{+}_{-}1.0$) for ν_μ ($\bar{\nu}_\mu$), with the cuts muon momenta $>$ 4 GeV/c and electron momentum $>$ 0.3 GeV/c.

The bubble chamber experiment of ref. [24] (light neon mix) finds $R_{\mu^-\mu^+}$ = $0.77^{+}_{-}0.3\%$ and a neutral strange particle multiplicity of $1.84^{+}_{-}\frac{0.3}{0.3}$ (with an electron momentum cut of 0.8 GeV/c). Another bubble chamber experiment ref. [27] using heavy mix

neon finds $R_{\mu^-e^+} = 0.4^{+}_{-}0.1\%$ and a neutral strange multiplicity of $0.6^{+}_{-}0.2$. A third bubble chamber experiment, that of ref. [54], finds $R_{\mu^-e^+} = 0.41^{+}_{-}0.15\%$ and a neutral strange particle multiplicity of $1.2^{+}_{-}0.5$.

The Monte Carlo indicates that our 4 GeV/c secondary muon momentum cut loses about 40% of the dimuons. Taking this into account we are in better agreement with ref. [27], and assuming no energy dependence of the neutral strangeness multiplicity we also are consistent with their strangeness rate.

The CDHS counter group experiment of ref. [50] which requires muon momentum > 4.5 GeV/c quotes an energy dependent neutrino-induced dimuon rate that is in good agreement with ours. Another counter experiment (ref. [51]) which cuts on muon momentum > 5 GeV/c also quotes an energy dependent rate and is slightly higher but still in good agreement with our neutrino-induced dimuon rate.

APPENDIX A

π/K DECAY IN BUBBLE CHAMBER CALCULATION

Each non-primary muon LT in the sub-sample of 1587 CC and 289 $\overline{CC}$ events was allowed to decay according to the distribution

$$P_{decay} = (1 - e^{-\alpha L})$$

where

L = *path length in bubble chamber*

$$\alpha = \frac{1}{\gamma\beta c\tau} + \frac{1}{\lambda}$$

λ = *absorption length*

γ, β = *Lorentz factors*

The simulated film points for the (meson + decay muon) composite track were processed through the geometric reconstruction program. The output tape from geometry had decays distributed as

$$N_{geom} = N_{LT}\,(1 - e^{-\alpha l}) \qquad \text{A1}$$

The number of expected decays is distributed as

$$N_{decay} = \epsilon\, N_0 (1 - e^{\alpha L}) \qquad \text{A2}$$

where $\epsilon = 1/\alpha\gamma\beta c\tau$ and N_0 is the number of mesons produced at the primary vertex. The number of LTs is related to N_0 as

$$N_{LT} = N_0\, e^{-\alpha L} + N_{decay} \qquad \text{A3}$$

where allowance is made for a small contamination of decays in the LT sample. Substituting A1 and A3 into A2 we get

$$N_{decay} = N_{geom} \frac{\epsilon}{e^{-\alpha L} + \epsilon(1 - e^{-\alpha L})} \qquad \text{A4}$$

The path of the true muon from the decay is extrapolated to the EMI by XTRAP and the hit randomly moved around to simulate coulomb + EMI + film measurement errors a total of 10 times. Each time there was a match with $CL'_{12} > 0.01$ the weight

$$weight = 0.1 \frac{\epsilon}{e^{-\alpha L} + \epsilon(1 - e^{-\alpha L})} \qquad \text{A5}$$

was summed. The final sum is the number of expected fake muons in the sub-sample due to decays in the bubble chamber.

In summary then, we use the LT sample to deduce the total meson production at the primary vertex and from that we obtain the predicted number of decays. The decays are simulated as actual measured events and then put through the analysis system. The resulting number of decays passing the cuts is the expected background.

APPENDIX B

CHARM PRODUCTION AND DECAY MONTE CARLO

The Monte Carlo [49] makes charm by the following reactions

$$\nu_\mu + d \rightarrow \mu^- + c$$

$$\nu_\mu + s \rightarrow \mu^- + c$$

$$\bar{\nu}_\mu + \bar{d} \rightarrow \mu^+ + \bar{c}$$

$$\bar{\nu}_\mu + \bar{s} \rightarrow \mu^+ + \bar{c} \, .$$

The cross section for charm production is assumed to be

$$\frac{d\sigma^{\nu}}{dxdy}(c) = \frac{G^2}{\pi} \, s \, x \left[\sin^2\theta_c \, d(x') + \cos^2\theta_c \, s(x') \right] f(x,x',y)$$

for the first two reactions above, and

$$\frac{d\sigma^{\bar{\nu}}}{dxdy}(\bar{c}) = \frac{G^2}{\pi} \, s \, x \left[\sin^2\theta_c \, \bar{d}(x') + \cos^2\theta_c \, \bar{s}(x') \right] f(x,x',y)$$

for the second two reactions above.

The functions $u(x)$, $d(x)$, $\bar{u}(x)$, and $\bar{d}(x)$ are the Field-Feynman x-distribution parameterizations; because the transition is from light quark to heavy quark, the modified scaling variable $x' = x + m_c^2/2ME$ is used, (m_c = c quark mass $= 1.5$ GeV, $M = 0.938$ GeV and E = incident neutrino energy). Since the scattering is fermion-fermion (for ν_μ) or antifermion-antifermion (for $\bar{\nu}_\mu$), the y dependence is flat, apart from the heavy quark transition scale breaking factor $f(x,x',y) = 1 - y(1-x/x')$, and the threshold requirement $W > W_c = (m_c + M)$.

The ν flux spectrum is from reference [42]; to verify that the ν flux is correct it was input to a Monte Carlo for single muon events and the resulting P_{μ^-} distribution compared with the single muon data (see figure 7.1).

The charmed quark is allowed to fragment into a D meson according to a flat z = $P_D.P_N/P_N.Q = E_D/\nu$ distribution with the requirement zyE > D mass (the flat z distribution gives the best fit to the data). The D meson is allowed to undergo the 3-body decay $D \rightarrow K\ \mu\ \nu$ using a K_{e3} -type matrix element (the results are somewhat insensitive to the detailed assumptions of the type of decay).

Hadron momenta transverse to the hadron system jet, P^{Th}, are smeared according to the distribution $P^{Th}\ e^{-6m^{Th}}$ where $m^{Th} = ((P^{Th})^2 + m^2)^{1/2}$. The potential length cut and 4 GeV/c muon momentum cut are applied. The calorimetric inefficiency of the bubble chamber is simulated and the energy correction applied to each event.

REFERENCES

[1] E. Fermi, Z. Physik 88, 161 (1934).

[2] T.D.Lee and C.N.Yang, Phys. Rev. 104, 254 (1956).

[3] R.P.Feynman and M.Gell-Mann, Phys.Rev. 109, 193 (1958).

[4] E.C.G.Sudarshan and K.E.Marshak, Phys. Rev. 109 1860 (1958).

[5] S.Weinberg, Phys. Rev. Lett. 19, 1264 (1967).

[6] A. Salam in Elementary Particle Theory, ed. by N.Svartholm (Almquist and Wiksell, Stockholm, 1969), p.367.

[7] F.J.Hasert et al., Phys. Lett. B46, 138 (1973).

[8] A.Benvenuti et al., Phys. Rev. Lett. 32, 800 (1974).

[9] M.Gell-Mann, Phys. Lett. 8, 214 (1964).

[10] N.Cabbibo, Phys. Rev. Lett. 10, 531 (1963).

[11] M.K.Gaillard and B.W.Lee, Phys. Rev. D10, 897 (1974).

[12] W.A.Carithers et al., Phys. Rev. Lett. 31, 1025 (1973).

[13] S.H.Aronson et al., Phys. Rev. Lett. 25, 1057 (1970).

[14] S.L.Glashow, J.Iliopoulos and L.Maini, Phys. Rev. D2, 1285 (1970).

[15] See for example E.D.Commins, Weak Interactions, McGraw-Hill, 1973.

[16] See for example A.DeRujula et al., Rev. Mod. Phys. 46, 391 (1974) and references contained therein.

[17] J.J.Aubert et al., Phys. Rev. Lett., 33, 1404 (1974).

[18] J.-E.Augustin et al., Phys. Rev. Lett., 33, 1406 (1974).

[19] G.Goldhaber et al., Phys. Rev. Lett., 37, 255 (1976).

[20] I.Peruzzi et al., Phys. Rev. Lett., 37, 569 (1976).

[21] A.Benvenuti et al., Phys. Rev. Lett., 34, 419 (1975).

[22] A.Benvenuti et al., Phys. Rev. Lett., 36, 1199 (1976).

[23] B.C.Barish et al., Phys. Rev. Lett., 36, 939 (1976).

[24] J.VonKrogh et al., Phys. Rev. Lett., 36, 710 (1976).

[25] J.Blietschau et al., Phys. Lett., 60B, 207 (1976).

[26] P.Bosetti et al., Phys. Rev. Lett. 38, 1248 (1977).

[27] C.Baltay et al., Phys. Rev. Lett. 39, 62 (1977).

[28] H.C.Ballagh et al., Phys. Rev. Lett. 39, 1650 (1977).

[29] C.T.Murphy, talk given at the XIIth Rencontre de Moriand, Les Arcs, Savoie, France 1977.

[30] P.Bosetti et al., Phys. Lett. 73B, 380 (1978).

[31] L.N.Chang,E.Derman and J.N.Ng, Phys. Rev. Lett. 35, 6 (1975).

[32] L.N.Chang,E.Derman,J.N.Ng, Phys. Rev. D12, 3539 (1975)

[33] C.H.Albright, Phys. Rev. D12, 1329 (1975).

[34] A.Pais,S.B.Treiman, Phys. Rev. Lett. 35, 1206 (1975).

[35] R.J.Cence et al., Nucl. Inst. and Meth. 138, 245 (1976).

[36] S.Parker, J.Orthel and J.Marriner, IEE transactions on Nuclear Science 25, 1 (1978).

[37] M.L.Stevenson, talk given at the Topical Conference on Neutrino Physics at Accelerators, Oxford, England, July 3-7, 1978.

[38] The kaon content of the LTs is a conservative estimate based on the measurement of the K_S^0 content of the random sample events and the assumption that the charged component equals the neutral component. Note that kaons are about 1.7 times as effective at producing fake muons from decays, compared to pions of the same momentum. If the kaon content were as high as 25% the background estimates for

decays would increase by about 10%. The proton fraction is based on the references Yeager et al., Phys.Rev. D16, 1294 (1977) and Burnett et al., Phys.Lett. 77B, 443 (1978).

[39] R.Heilman, CERN WA21-int-1 (11 Sept. 1978).

[40] A significant background to $\mu^+\mu^-$ events is $\mu^-\mu^+$ events that happen to lie in the area of phase space with $P_{\mu_1}^{Th} < P_{\mu_2}^{Th}$. Because of Fermi motion of the target nucleon in the parent Neon nucleus one expects transverse momentum to balance to within an uncertainty of about 400 MeV/c. From figure 6.2a we see that there are 2 ± 1 $\mu^-\mu^+$ events within 400 MeV/c of the diagonal line so that we take this as the estimated crossover. The charm Monte Carlo (see appendix B for description) is consistent with this estimate. Note also that the background crossover is about 1 event and is included in the backgrounds of table 6.2.

[41] A. Grant,CERN/D.Ph.II/PHYS 75-42, 15 August 1975

[42] R.J.Stefanski, private communication.

[43] J.Lys, private communication.

[44] F.Harris, private communication.

[45] These numbers include a correction factor of 0.99 to account for EMI instrumental inefficiency in detecting the decay muon.

[46] These numbers include a correction factor of 1.09 to account for the missed 0 and -1 constraint solutions in plane-1.

[47] M.K.Gaillard, B.W.Lee, J.L.Rosner, Rev.Mod.Phys. 47, 277 (1975).

[48] There is evidence for separate decay vertices in some of the μe events found in this experiment. See University of Hawaii preprint UH-511-351-79, July 1979.

[49] The Monte Carlo was modified from a program written by J. Wills based on C.H.Lai, Phys.Rev. D18, 1422 (1978). (Note the typo in equation 18).

[50] M.Holder et al., Phys.Lett 69B, 377 (1977).

[51] A.Benvenuti et al., Phys.Rev.Lett. 41, 1204 (1978).

[52] Event 15760673 is given no weight because the V^0 decays less than 0.5 cm from the primary vertex. Also note that there is only one K/Λ ambiguity: event 15560114. One of the decay tracks in this V^0 interacts after 22 cm so that its momentum is poorly determined by curvature. However measurement of the secondaries rules out the Λ interpretation.

[53] Note that the relative dimuon rate will not depend on the value of ESEV.

[54] J.Alitti et al., Phys.Lett. 77B, 227 (1979).

[55] A general measure of the width of the pion rapidity distribution in the laboratory frame (= first term in definition of Y_q) for a group of events with invariant hadron mass W, is $ln(W^2/M^2)$. The purpose of the $-ln(W^2/M^2)$ term in the definition of Y_q is to line up the upper ends of the rapidity distributions of groups of events with different W. See J.Bell et al., Phys.Rev. D19, 1 (1979).

[56] University of Washington internal reports VTL-HEP-59 (8 march, 1978) and VTL-HEP-59.1 (9 Febuary, 1979).

FIGURE CAPTIONS

Fig. 5.1 Distribution of EMI geometric weights for single-muon events.

Fig. 5.2 Distribution of EMI geometric weights for opposite-sign dimuon candidates (histogram) and background (smooth curve labeled BG).

Fig. 5.3 Distribution of EMI geometric/V^0 detection weights for single-muon events.

Fig. 5.4 Distribution of EMI geometric/V^0 detection weights for opposite sign dimuon candidate events (histogram) and background (smooth curve labeled BG).

Fig. 6.1 Scatter-plot of momentum perpendicular to the neutrino direction for muon-1 versus muon-2 in opposite-sign dimuon events. The solid dots are $\mu^-\mu^+$candidates; the open dots are $\mu^+\mu^-$ candidates.

Fig. 6.2 Scatter-plot of momentum perpendicular to the hadron jet direction for muon-1 versus muon-2 in opposite-sign dimuon events. Solid dots are $\mu^-\mu^+$ candidates; open dots are $\mu^+\mu^-$ candidates.

Fig. 7.1 Momentum distribution of muon in single-muon events. The smooth curve is from a Monte Carlo, (using the flux of reference [42] and B=0.8), for P_{μ^-} by M. L Stevenson. All events are weighted by the inverse of the EMI geometric detection efficiency; neutrino-induced events are unshaded histograms, antineutrino-induced events are shaded histograms-- these conventions are used in all the following figures.

Fig. 7.2 Energy distribution of single-muon events: (a)visible; (b)corrected for missing neutrals.

Fig. 7.3 Distribution of the scaling variable x for single muon events: (a)visible, (b)corrected.

Fig. 7.4 Distribution of the scaling variable y for single-muon events: (a)visible; (b)corrected; smooth curve is Monte Carlo-calculated efficiency resulting from the 4 GeV/c primary muon cut.

Fig. 7.5 Distribution of the square of the four-momentum transfer, Q^2, (corrected) for single-muon events.

Fig. 7.6 Distribution of the corrected invariant mass of the hadron system, W, for single-muon events.

Fig. 7.7 Distribution of the momentum of strange particles in single-muon events (this and all suosequent histograms pertaining to V^0's contain events weighted for EMI/V^0 geometric detection efficiency): (a) K_S^0; (b) Λ^0.

Fig. 7.8 Distribution of momentum perpendicular to the muon-neutrino plane of hadrons in single-muon events (a)positive hadrons (all momenta); (b)negative hadrons (all momenta); (c)positive hadrons (P > 4 GeV/c); (d)negative hadrons (P > 4 GeV/c); (e) V^0 all momenta.

Fig. 7.9 Distribution of the fraction of total hadronic energy z carried by individual hadrons in single-muon events: (a)positives (all momenta); (b)negatives (all momenta); (c)positives (P > 4 GeV/c); (d)negatives (P > 4 GeV/c); (e) V^0 all momenta.

Fig. 7.10 Distribution of the rapidity in the quark frame Y_q of hadrons in single-muon events: (a)positives (all momenta); (b)negatives (all momenta); (c)positives (P > 4 GeV/c); (d)negatives (P > 4 GeV/c); (e) V^0 all momenta.

Fig. 7.11 Distribution of the azimuthal angle ϕ between primary muon and hadrons (with hadron momentum > 4 GeV/c) in single-muon events. For neutrino events (unshaded) the hadrons selected are positive: for antineutrino events (shaded) the hadrons are negative. For definition of angle ϕ see section 7 of text.

Fig. 7.12 Primary muon momentum P_{μ_1} distribution in opposite-sign dimuon candidates. The charm production and decay Monte Carlo for $\mu^-\mu^+$ events (normalized to signal minus background) is the smooth curve, the $\mu^-\mu^+$ background is in solid dots, and the $\mu^+\mu^-$ candidates are shaded histograms; these conventions are used throughout the remaining figures.

Fig. 7.13 Secondary muon momentum P_{μ_2} distribution in opposite-sign dimuon candidates.

Fig. 7.14 Scatter-plot of P_{μ_2} versus P_{μ_1} in opposite-sign dimuons. Solid dots are $\mu^-\mu^+$ candidates; open dots are $\mu^+\mu^-$ candidates.

Fig. 7.15 Energy distribution of opposite-sign dimuon candidates: (a)visible; (b)corrected for missing neutrals.

Fig. 7.16 x distribution of opposite-sign dimuon candidates: (a)visible; (b)corrected.

Fig. 7.17 y distribution of opposite-sign dimuon candidates: (a)visible; (b)corrected.

Fig. 7.18 Distribution of corrected four-momentum transfer to the hadron system squared, Q^2, of opposite-sign dimuon candidates.

Fig. 7.19 Distribution of corrected invariant hadron system mass, W, for opposite-sign dimuon candidates.

Fig. 7.20 Distribution of primary muon momentum transverse to hadron jet in opposite-sign dimuon candidates.

Fig. 7.21 Distribution of secondary muon momentum transverse to hadron jet in opposite-sign dimuon candidates.

Fig. 7.22 Distribution of secondary muon momentum perpendicular to the plane containing the primary muon and incoming neutrino momentum vectors in opposite-sign dimuon candidates.

Fig. 7.23 z (fraction of total hadronic energy) distribution of secondary muon in opposite-sign dimuon candidates.

Fig. 7.24 Y_q (rapidity in struck quark frame) distribution of secondary muon in opposite-sign dimuon candidates.

Fig. 7.25 Distribution of the azimuthal angle ϕ between primary and secondary muons (see section 7 of text for definition) in opposite-sign dimuon candidates.

Fig. 7.26 Distribution of invariant mass of primary and secondary muons in opposite-sign dimuon candidates.

Fig. 7.27 Distribution of invariant mass of secondary muon and V^0 in opposite-sign candidates: (a) K_S^0; (b) Λ^0.

Fig. 7.28 Distribution of V^0 momentum in opposite-sign dimuon candidates: (a) K_S^0 (note that background and Monte Carlo are times 10); (b) Λ^0.

Fig. 7.29 Distribution of V^0 momentum perpendicular to μ_1-ν plane.

Fig. 7.30 z distribution of V^0s in opposite sign dimuons.

Fig. 7.31 Y_q distribution of V^0 in opposite sign dimuons.

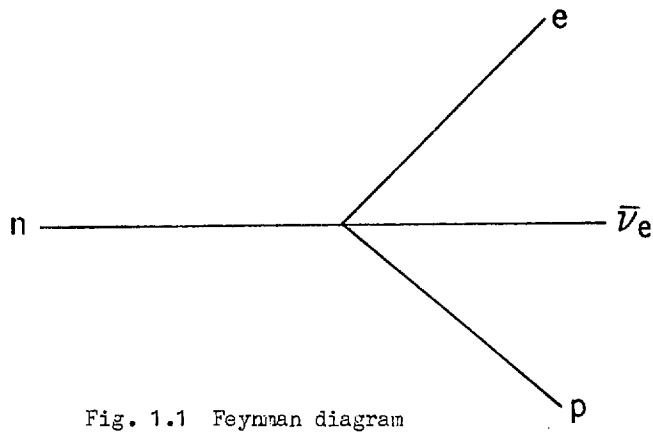

Fig. 1.1 Feynman diagram for four-fermion interaction in neutron decay.

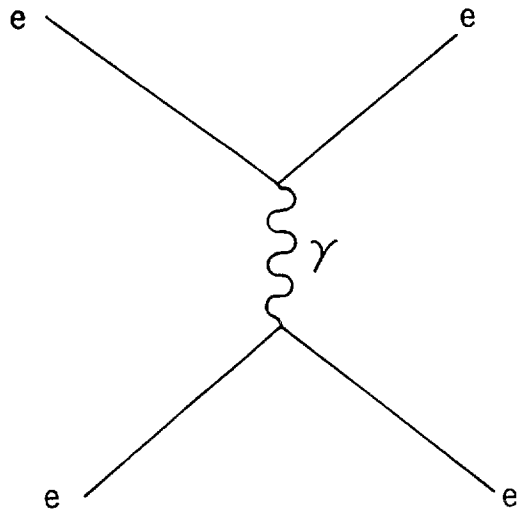

Fig. 1.2 Electron-electron scattering.

XBL 797-2114

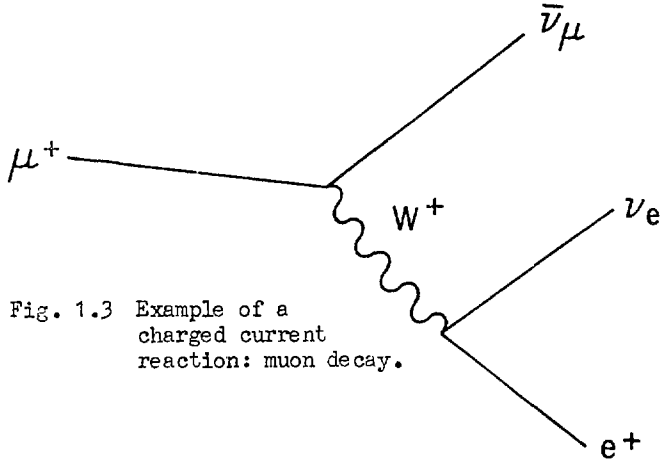

Fig. 1.3 Example of a charged current reaction: muon decay.

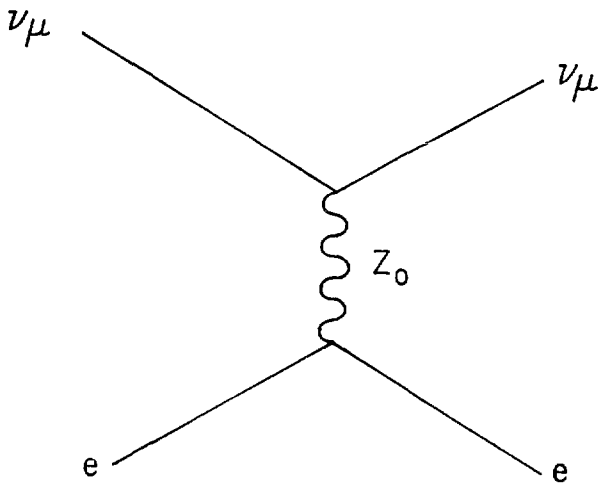

Fig. 1.4 Example of a neutral current reaction: neutrino-electron scattering.

XBL 797-2116

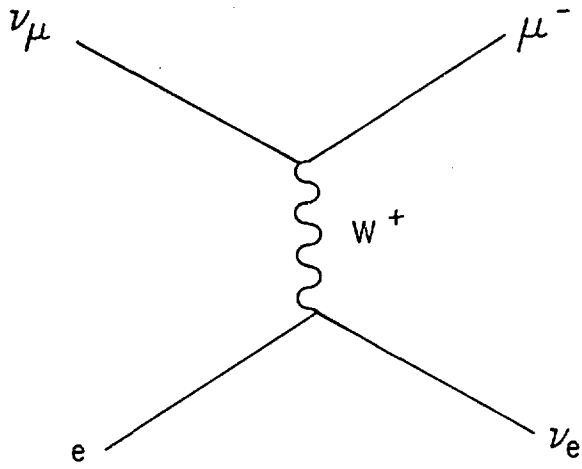

Fig. 1.5 Neutrino-lepton scattering.

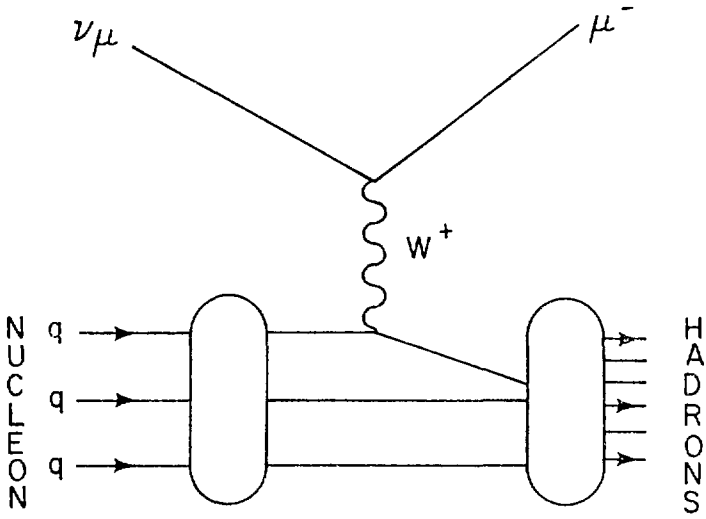

Fig. 1.6 Deep inelastic neutrino-nucleon scattering.

XBL 797-2117

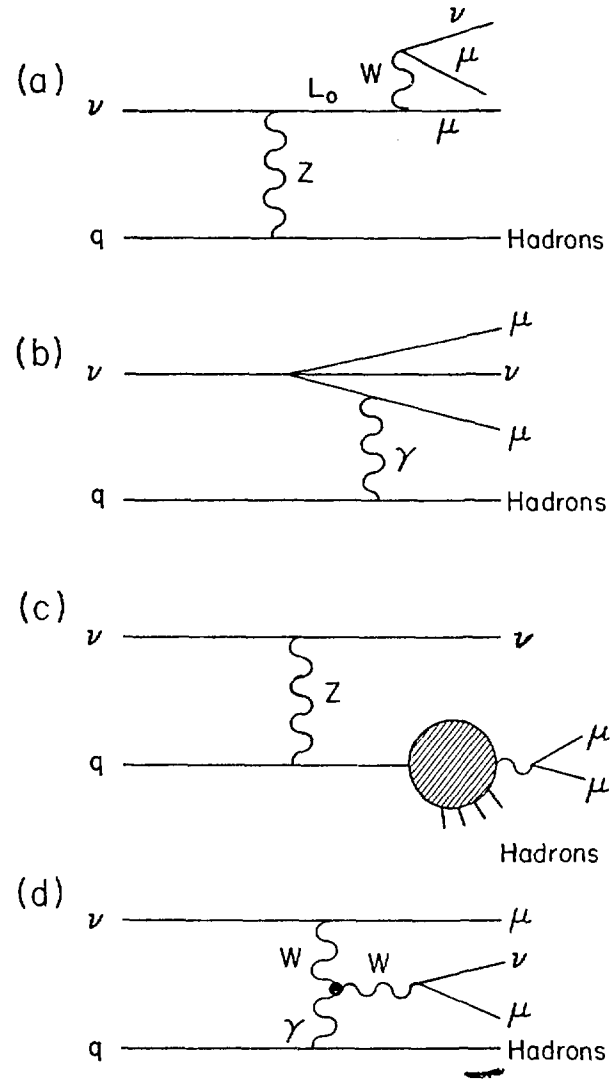

Fig. 1.7 Some possible sources of dimuons.

XBL 797-2118

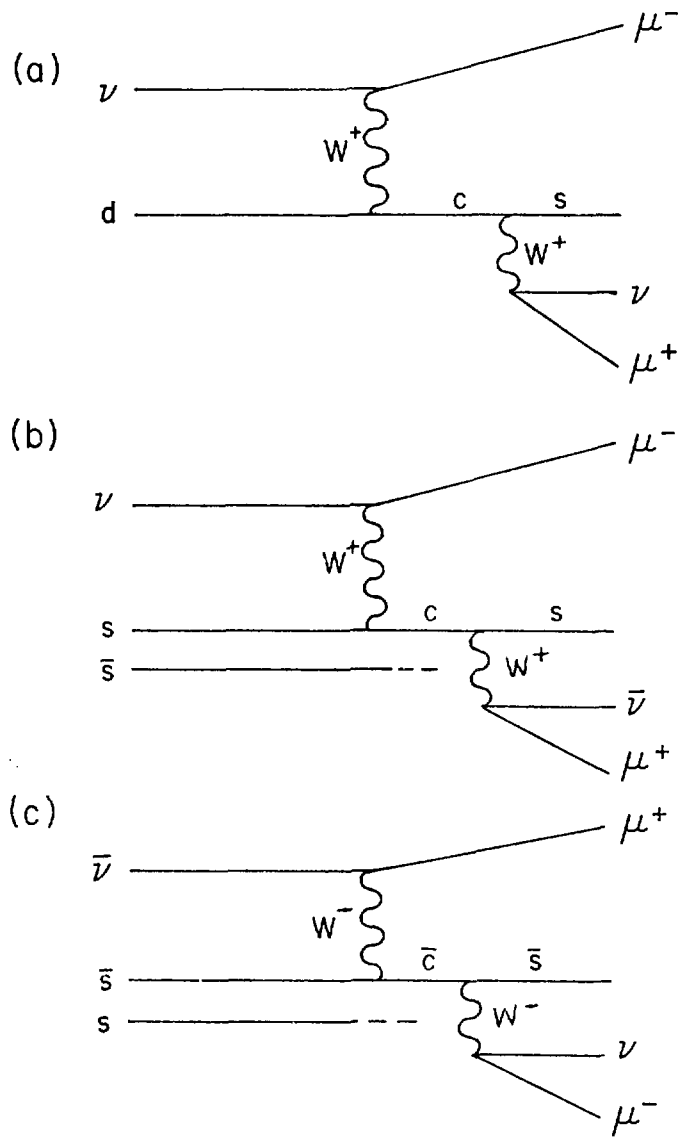

Fig. 1.8 Dimuon production by GIM mechanism.

XBL 797-2119

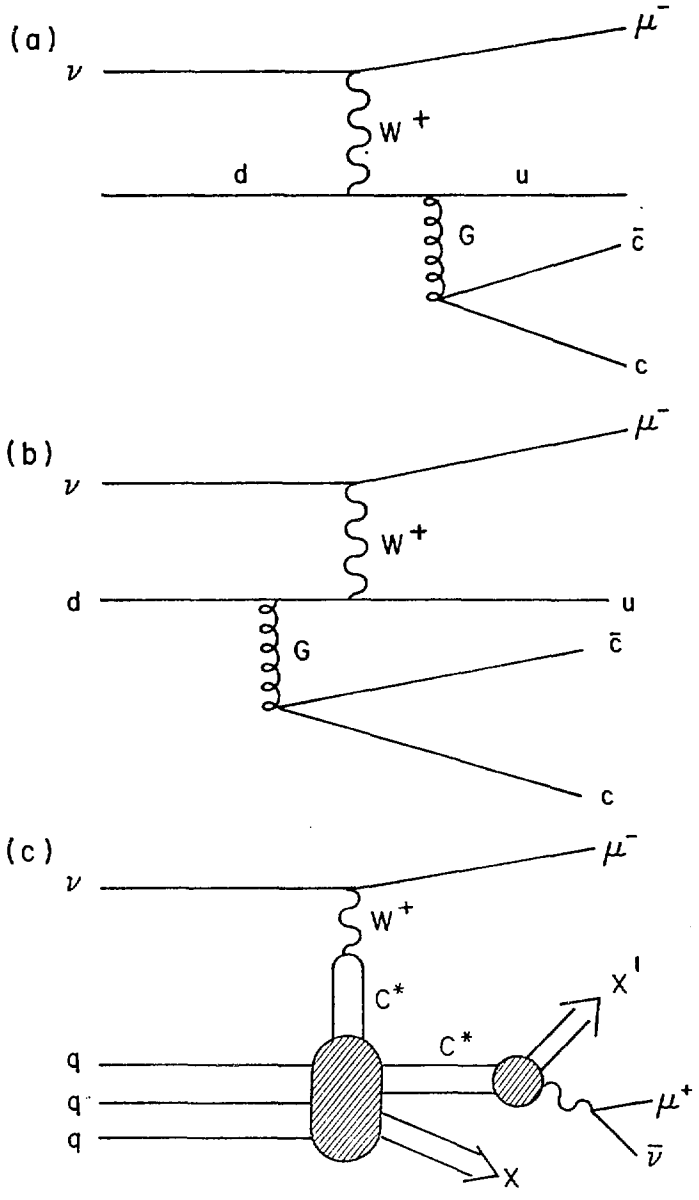

Fig. 1.9 Other mechanisms for charm production.

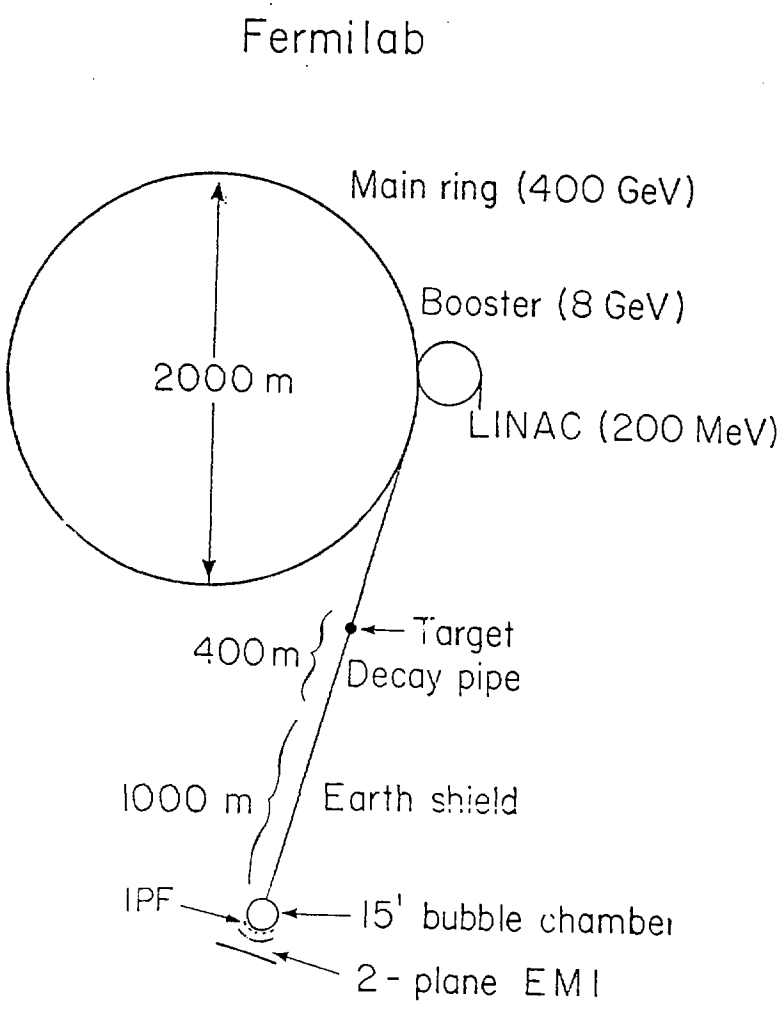

Fig. 2.1 Experimental apparatus used in E546 (EMI and bubble chamber not to scale).

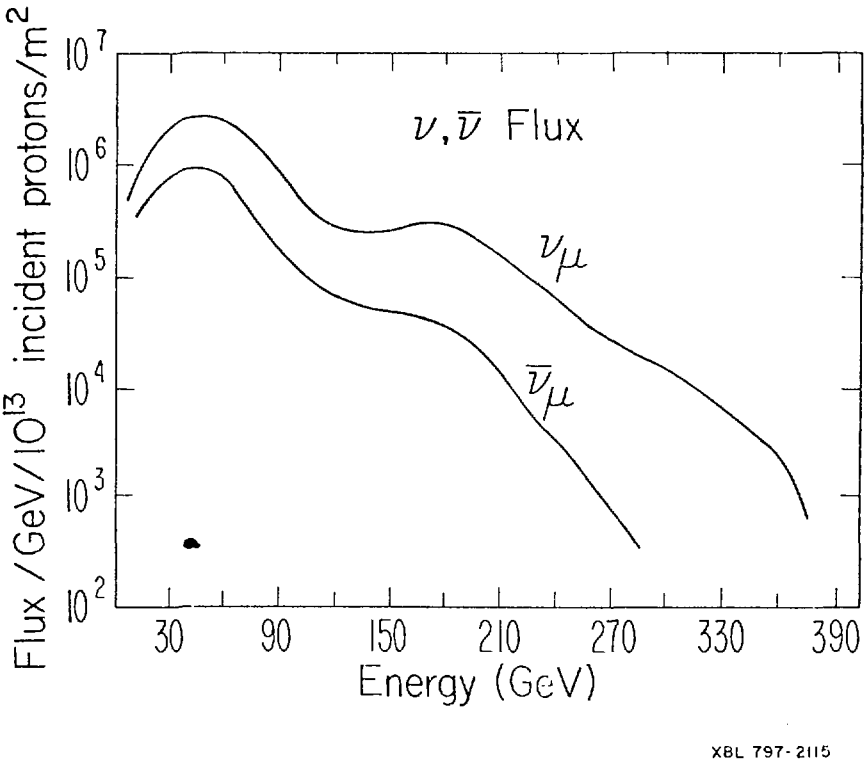

Fig. 2.2 Quadrupole triplet beam spectrum.

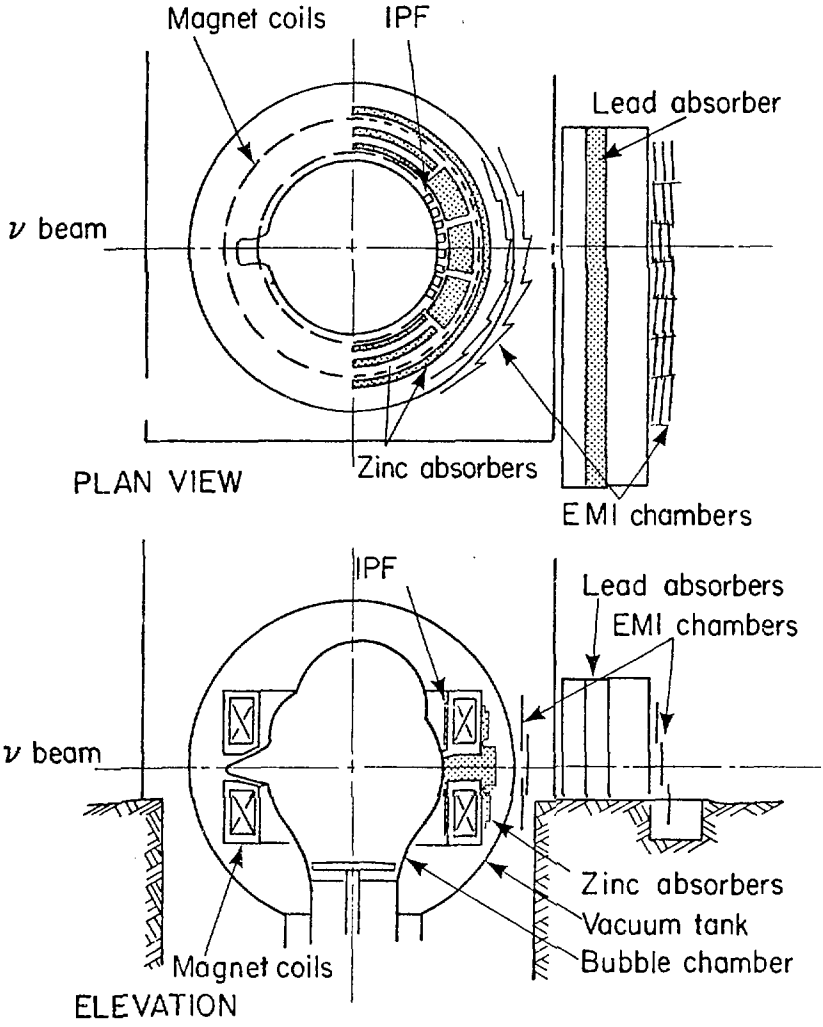

XBL797-2123

Fig. 2.3 Schematic of detector.

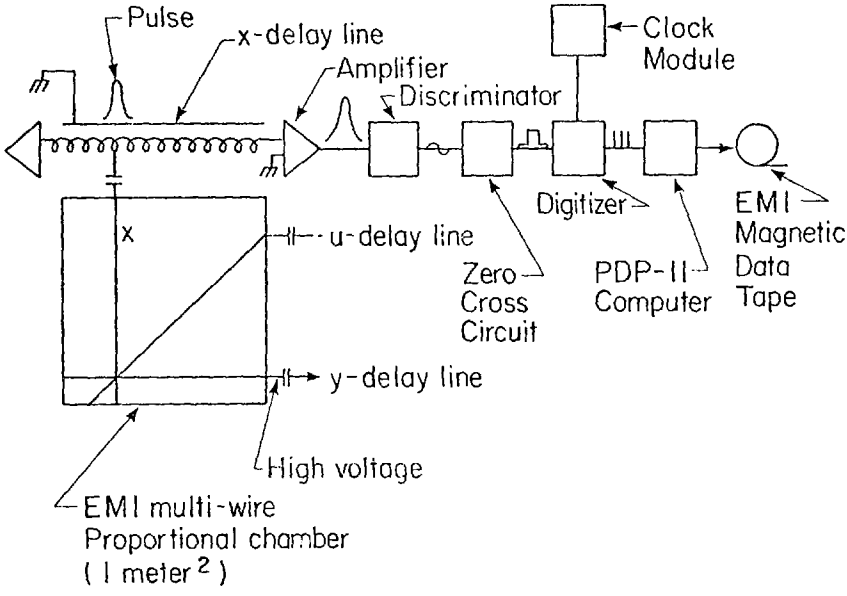

XBL 797-2122

Fig. 2.4 Schematic of an EMI MWPC and data readout system.

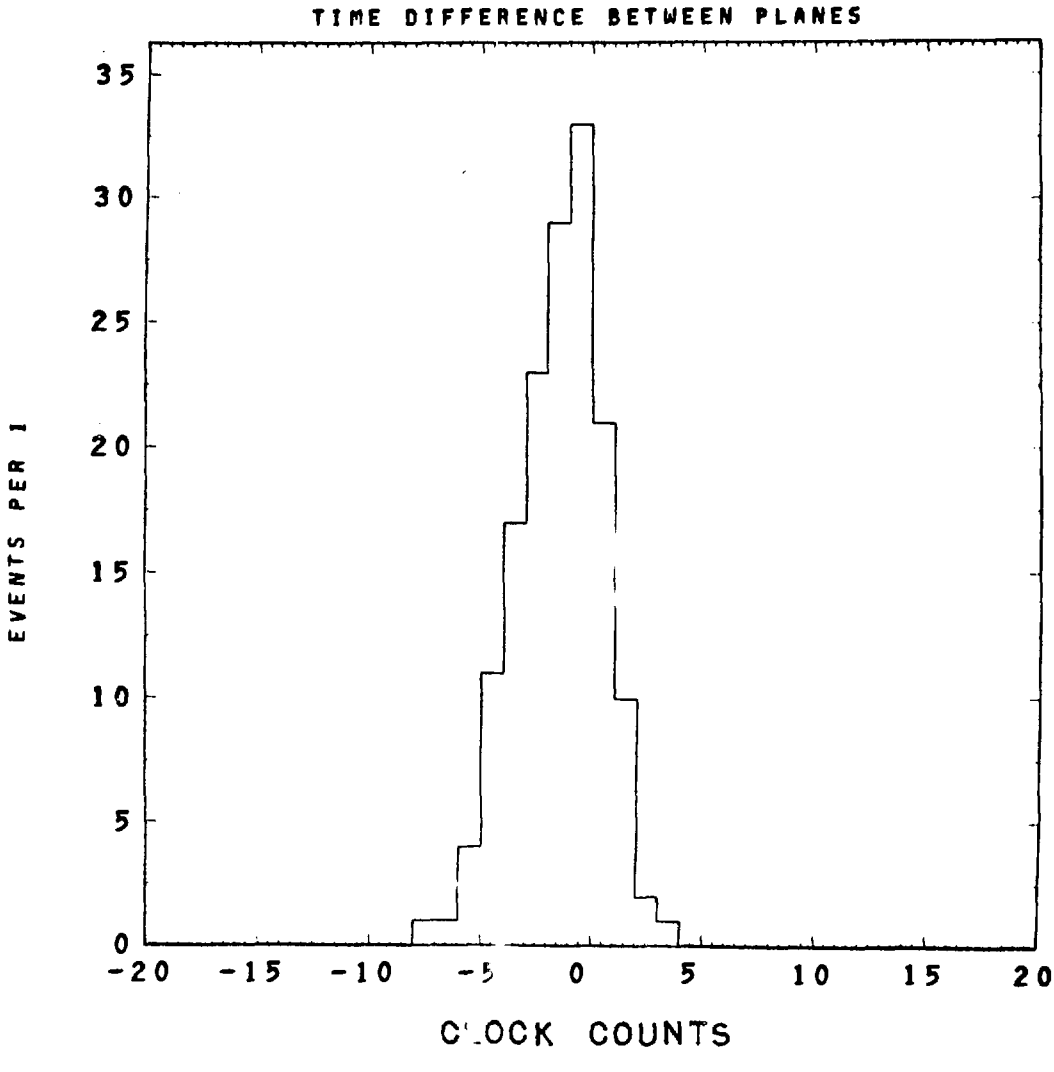
TIME DIFFERENCE BETWEEN PLANES
EVENTS PER 1
35
30
25
20
15
10
5
0
-20
-15
-10
-5
0
5
10
15
20
CLOCK COUNTS

Fig. 2.5

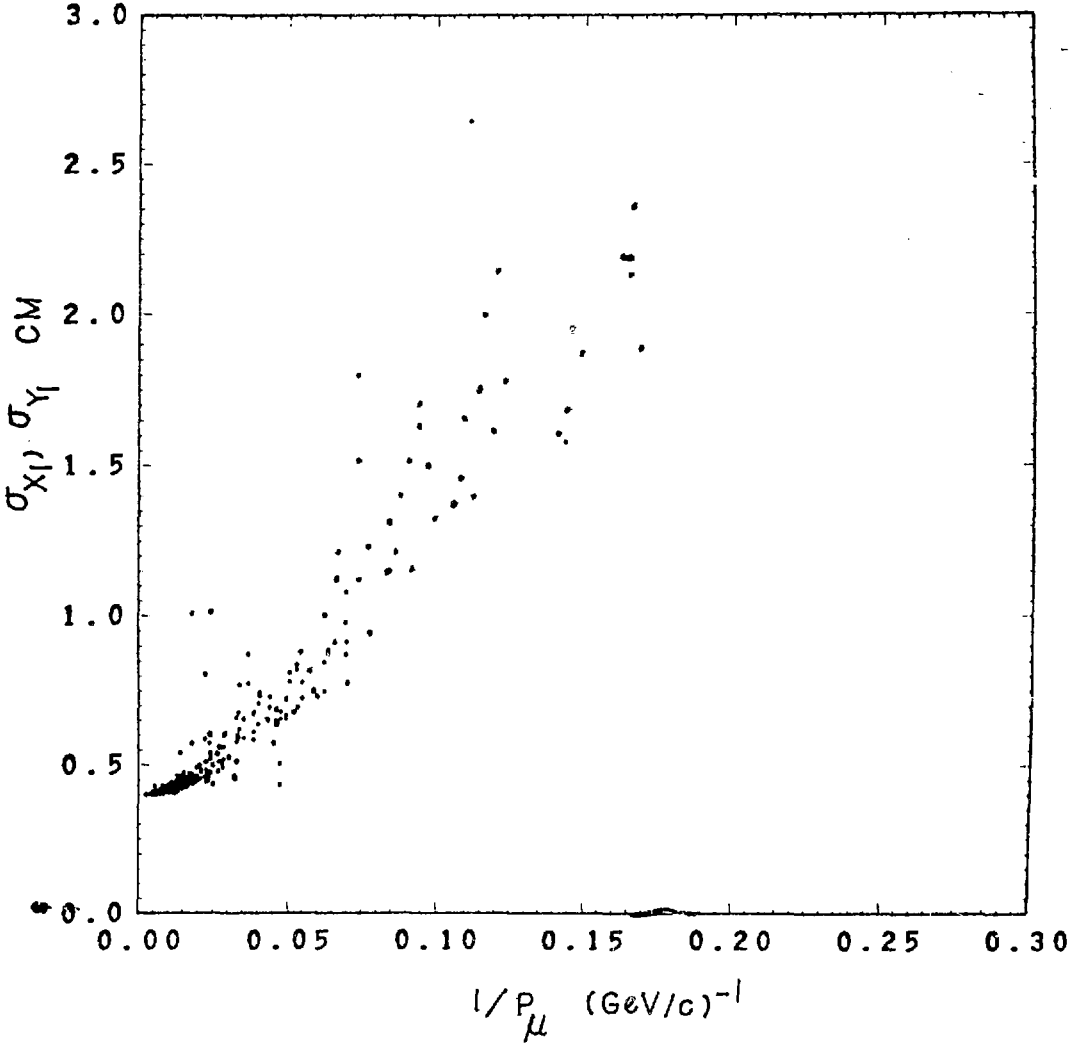
3.0
2.5
2.0
1.5
1.0
0.5
0.0
$\sigma_{X\ell}\ \sigma_{Y\ell}$ CM
0.00
0.05
0.10
0.15
0.20
0.25
0.30
$1/P_\mu$ (GeV/c)$^{-1}$

Fig. 3.1

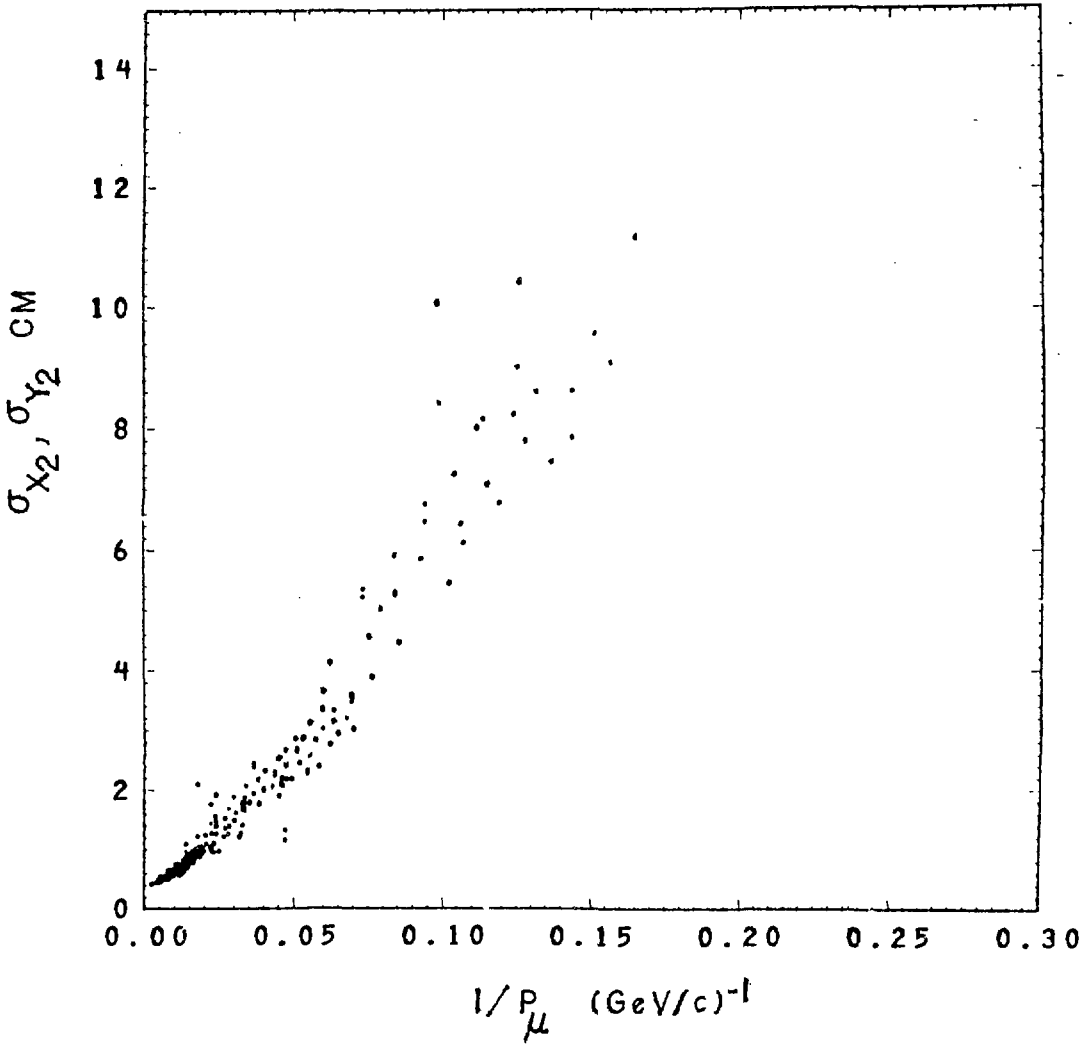
14
12
10
8
6
4
2
0
0.00
0.05
0.10
0.15
0.20
0.25
0.30
σ_{X2}, σ_{Y2} CM
$1/P_\mu$ (GeV/c)$^{-1}$

Fig. 3.2

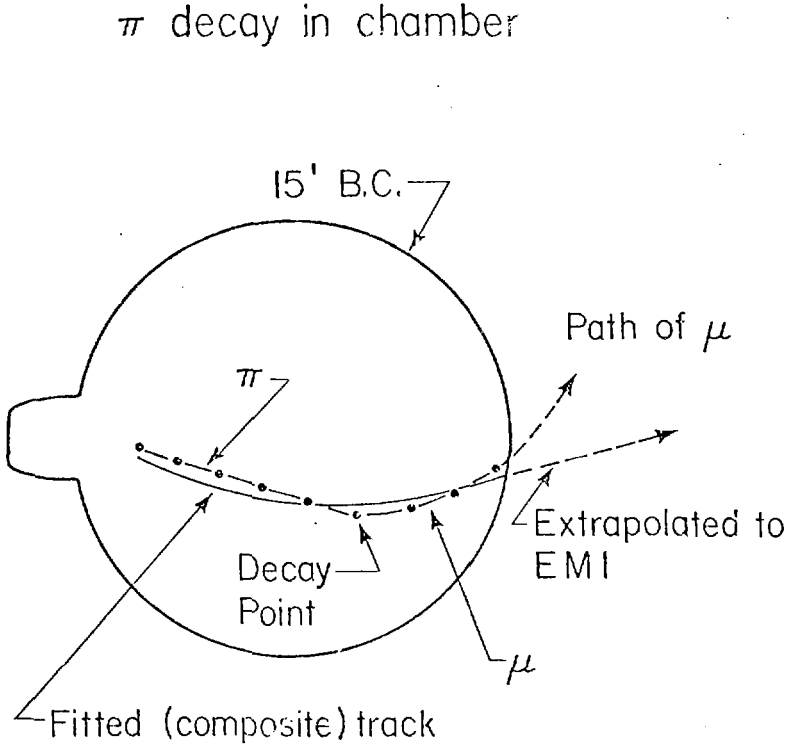

Fig. 4.1 Pion decay in flight can fake a muon if the composite track extrapolates to the same place in the EMI as the decay muon.

XBL 797-2124

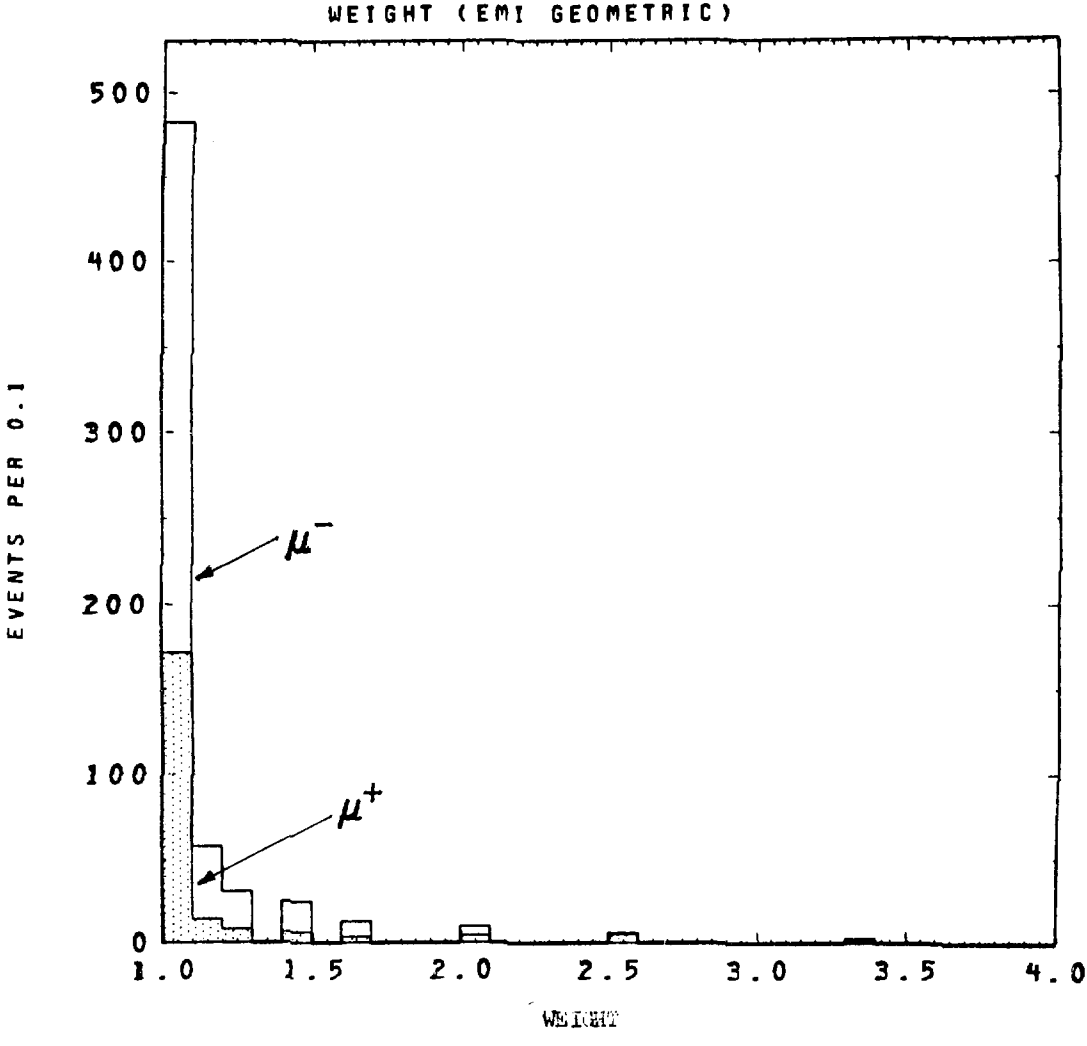
WEIGHT (EMI GEOMETRIC)
EVENTS PER 0.1
500
400
300
200
100
0
μ^-
μ^+
1.0
1.5
2.0
2.5
3.0
3.5
4.0
WEIGHT

Fig. 5.1

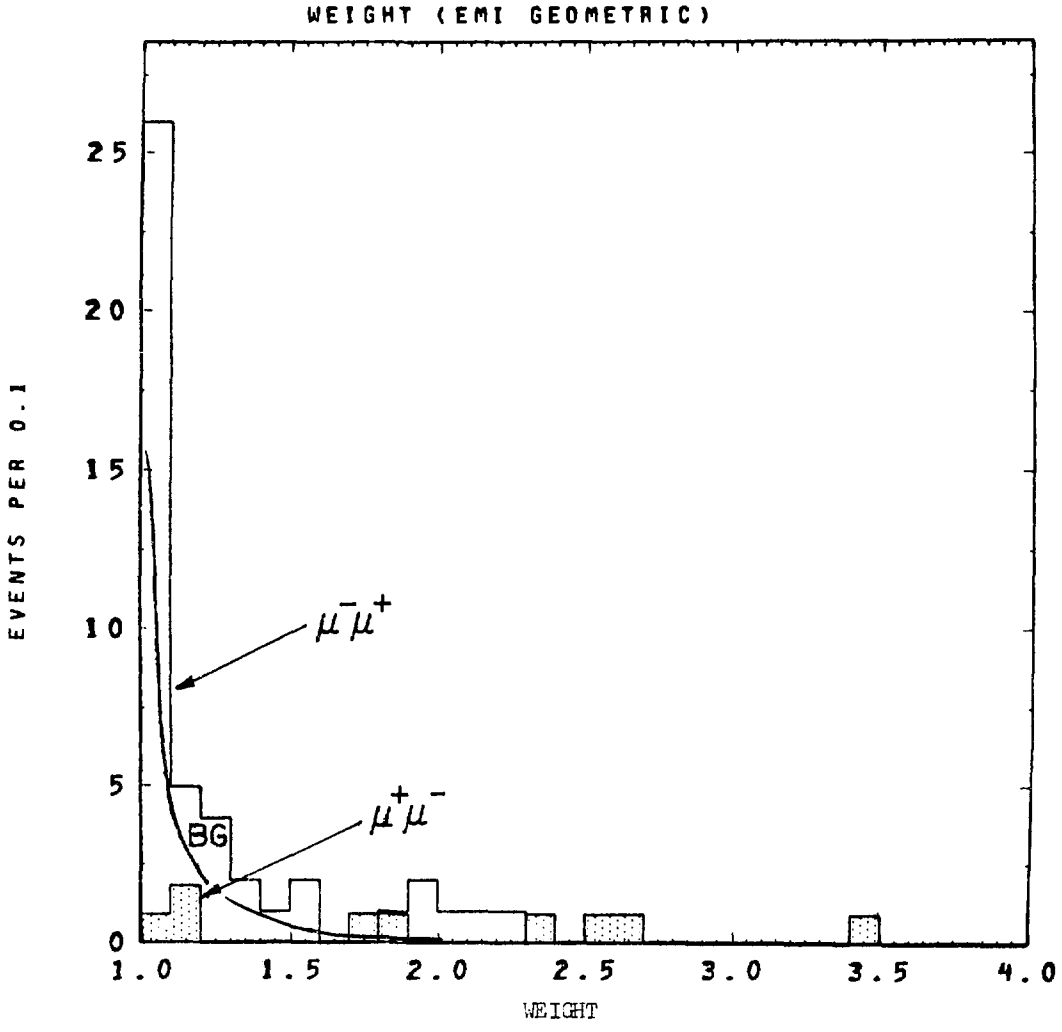
WEIGHT (EMI GEOMETRIC)
EVENTS PER 0.1
25
20
15
10
5
0
1.0
1.5
2.0
2.5
3.0
3.5
4.0
WEIGHT
$\mu^-\mu^+$
$\mu^+\mu^-$
BG

Fig. 5.2

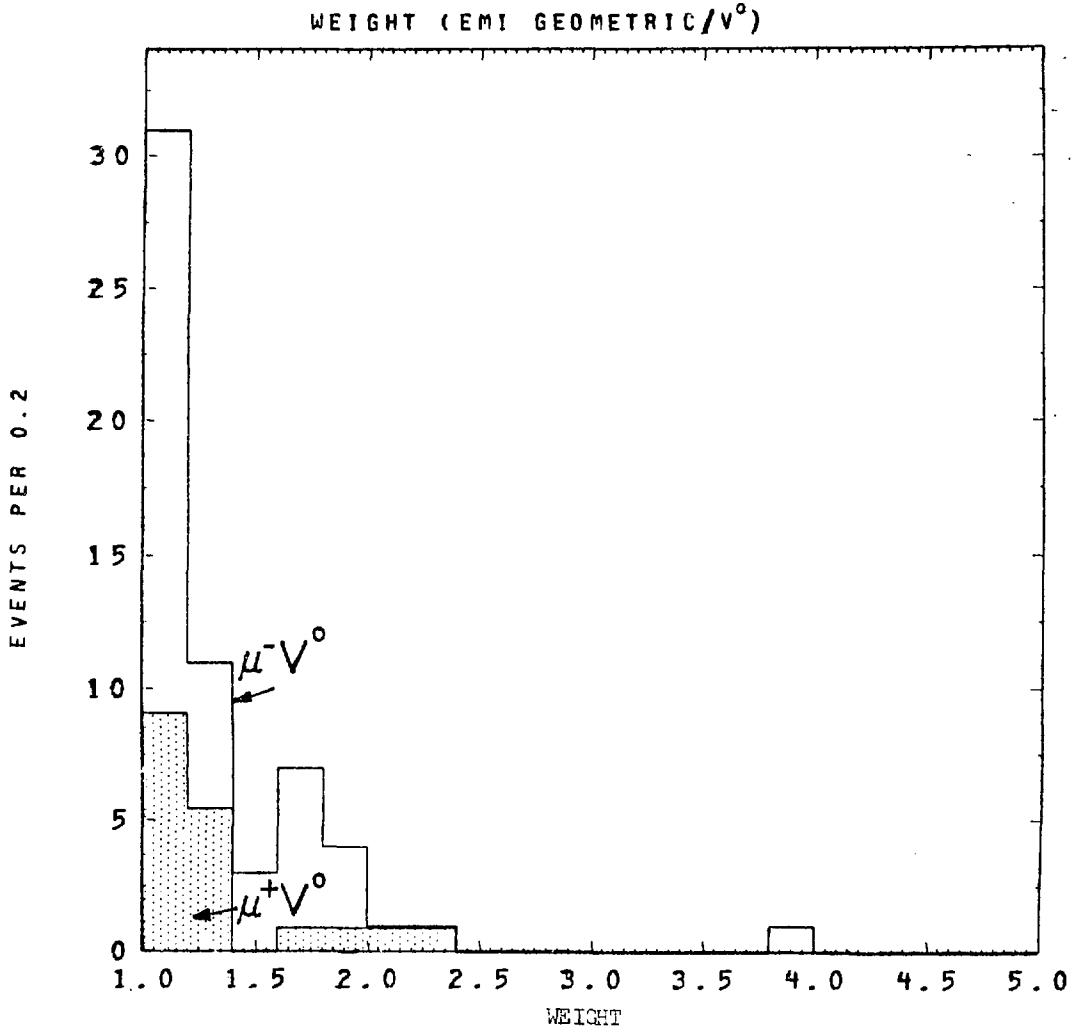
WEIGHT (EMI GEOMETRIC/V°)
EVENTS PER 0.2
30
25
20
15
10
5
0
μ⁻V°
μ⁺V°
1.0
1.5
2.0
2.5
3.0
3.5
4.0
4.5
5.0
WEIGHT

Fig. 5.3

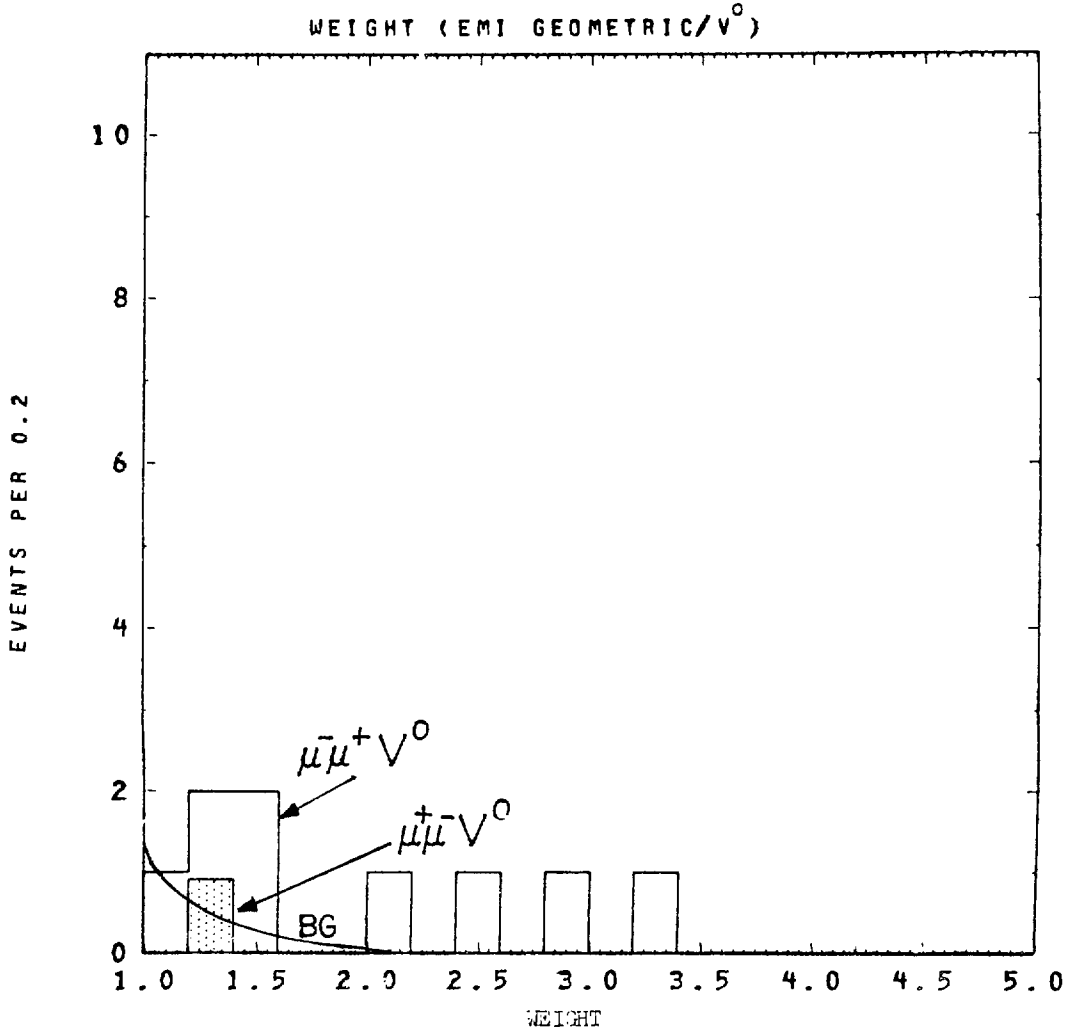
WEIGHT (EMI GEOMETRIC/V°)
EVENTS PER 0.2
10
8
6
4
2
0
μ⁻μ⁺V°
μ⁺μ⁻V°
BG
1.0
1.5
2.0
2.5
3.0
3.5
4.0
4.5
5.0
WEIGHT

Fig. 5.4

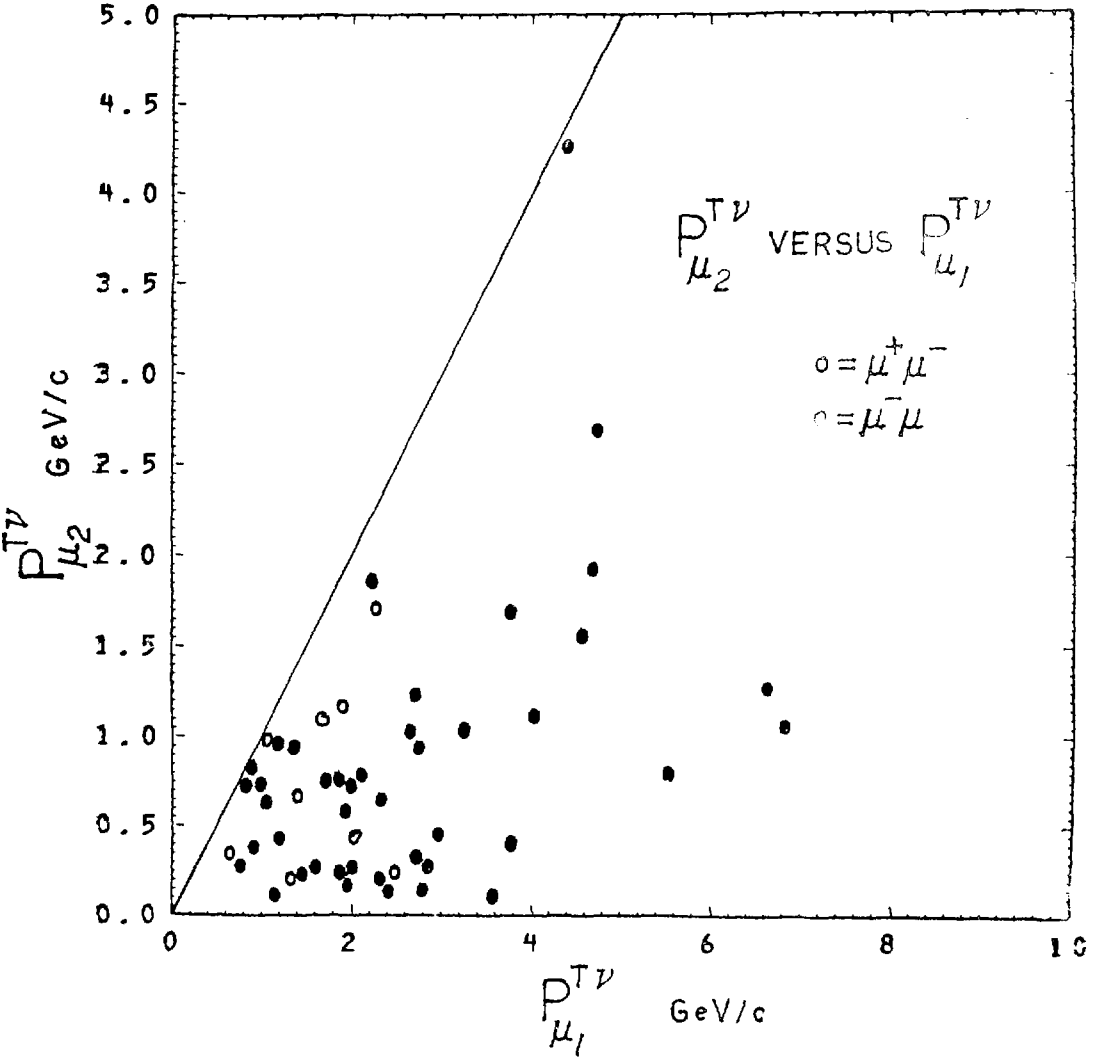
5.0
4.5
4.0
3.5
3.0
2.5
2.0
1.5
1.0
0.5
0.0
0
2
4
6
8
1 0
$P^{T\nu}_{\mu_2}$ GeV/c
$P^{T\nu}_{\mu_1}$ GeV/c
$P^{T\nu}_{\mu_2}$ VERSUS $P^{T\nu}_{\mu_1}$
o = $\mu^+\mu^-$
• = $\mu^-\mu$

Fig. 6.1

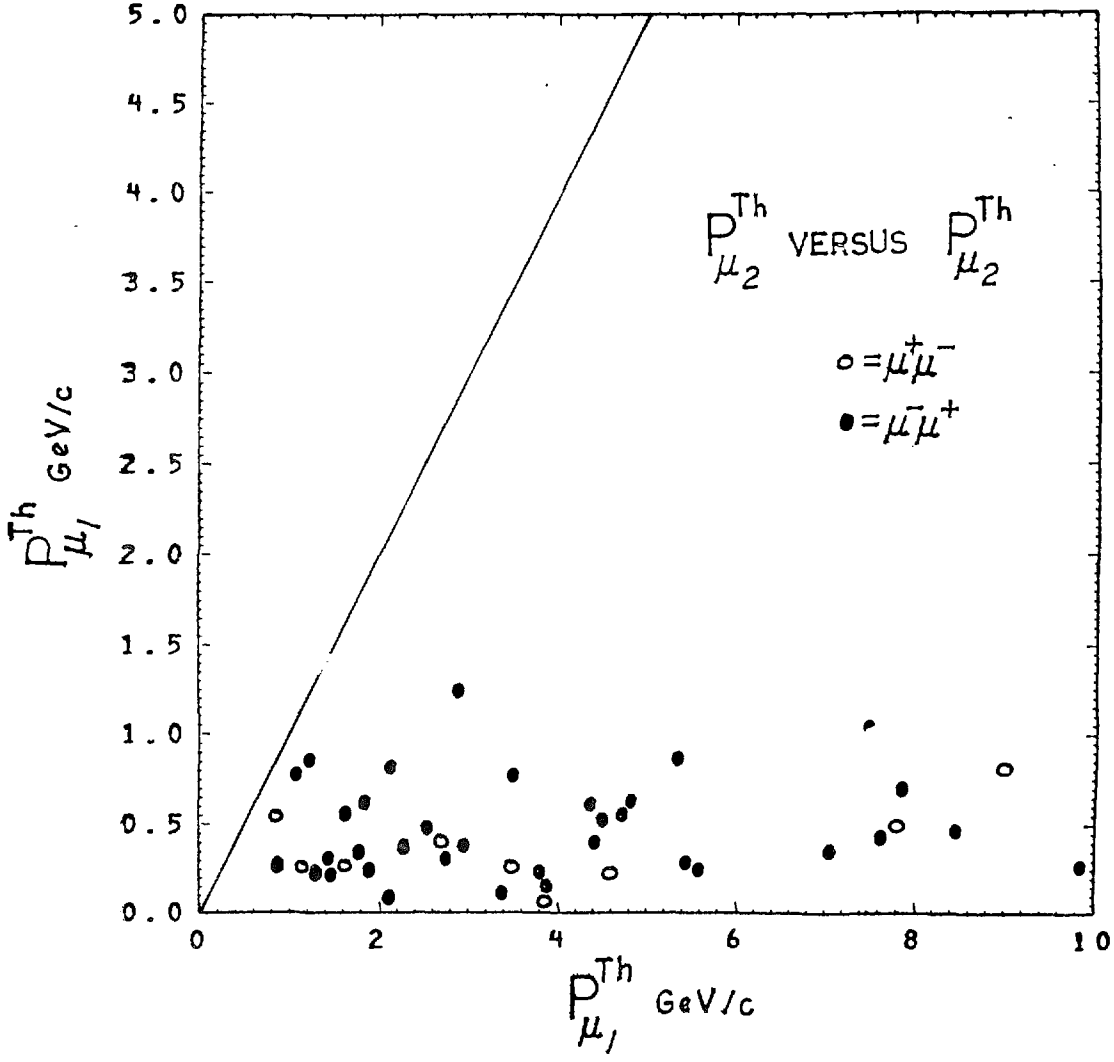
$P^{Th}_{\mu_2}$ VERSUS $P^{Th}_{\mu_2}$
o = $\mu^+\mu^-$
● = $\mu^-\mu^+$
$P^{Th}_{\mu_1}$ GeV/c
$P^{Th}_{\mu_1}$ GeV/c
0.0
0.5
1.0
1.5
2.0
2.5
3.0
3.5
4.0
4.5
5.0
0
2
4
6
8
10

Fig. 6.2

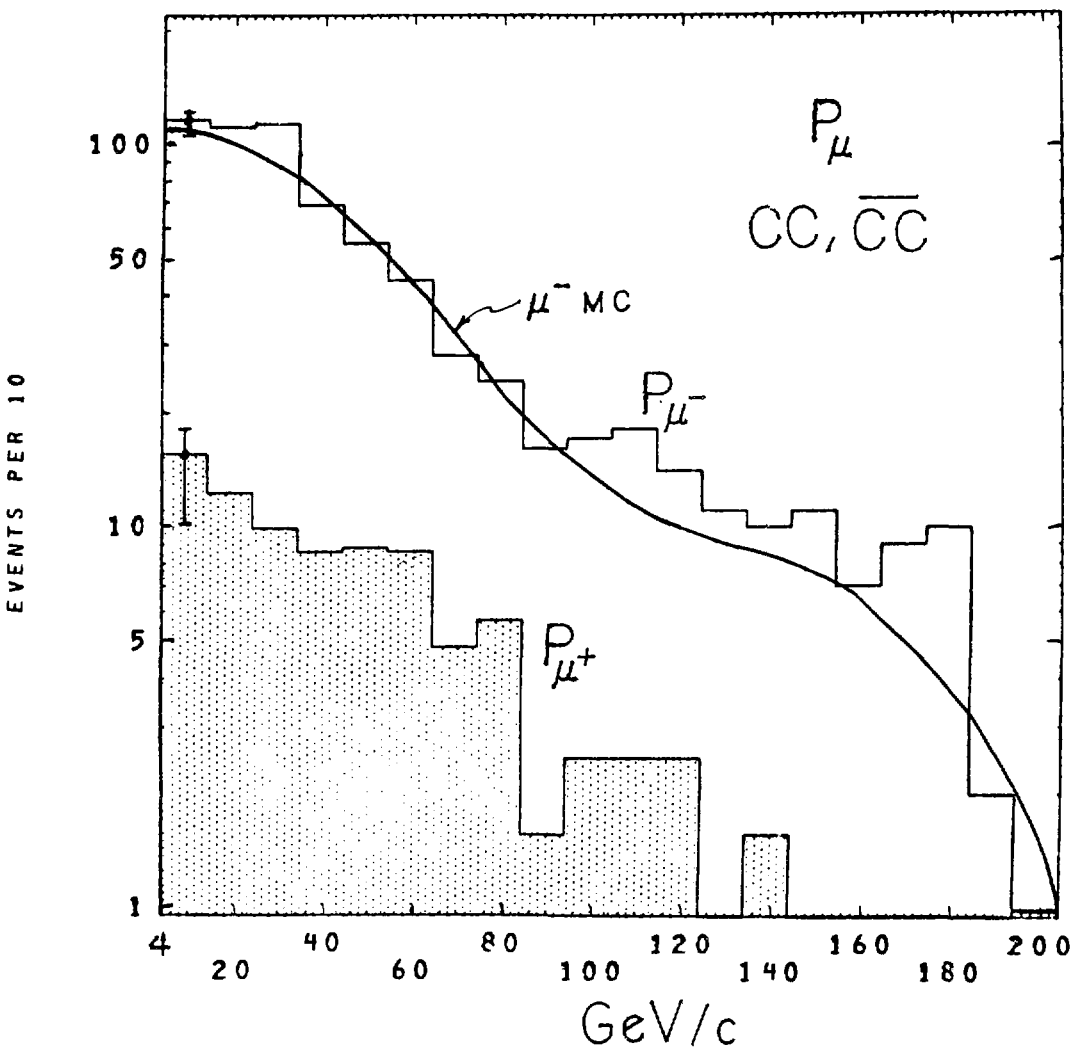
EVENTS PER 10
100
50
10
5
1
4
20
40
60
80
100
120
140
160
180
200
GeV/c
P_μ
CC, $\overline{CC}$
μ^- MC
P_{μ^-}
P_{μ^+}

Fig. 7.1

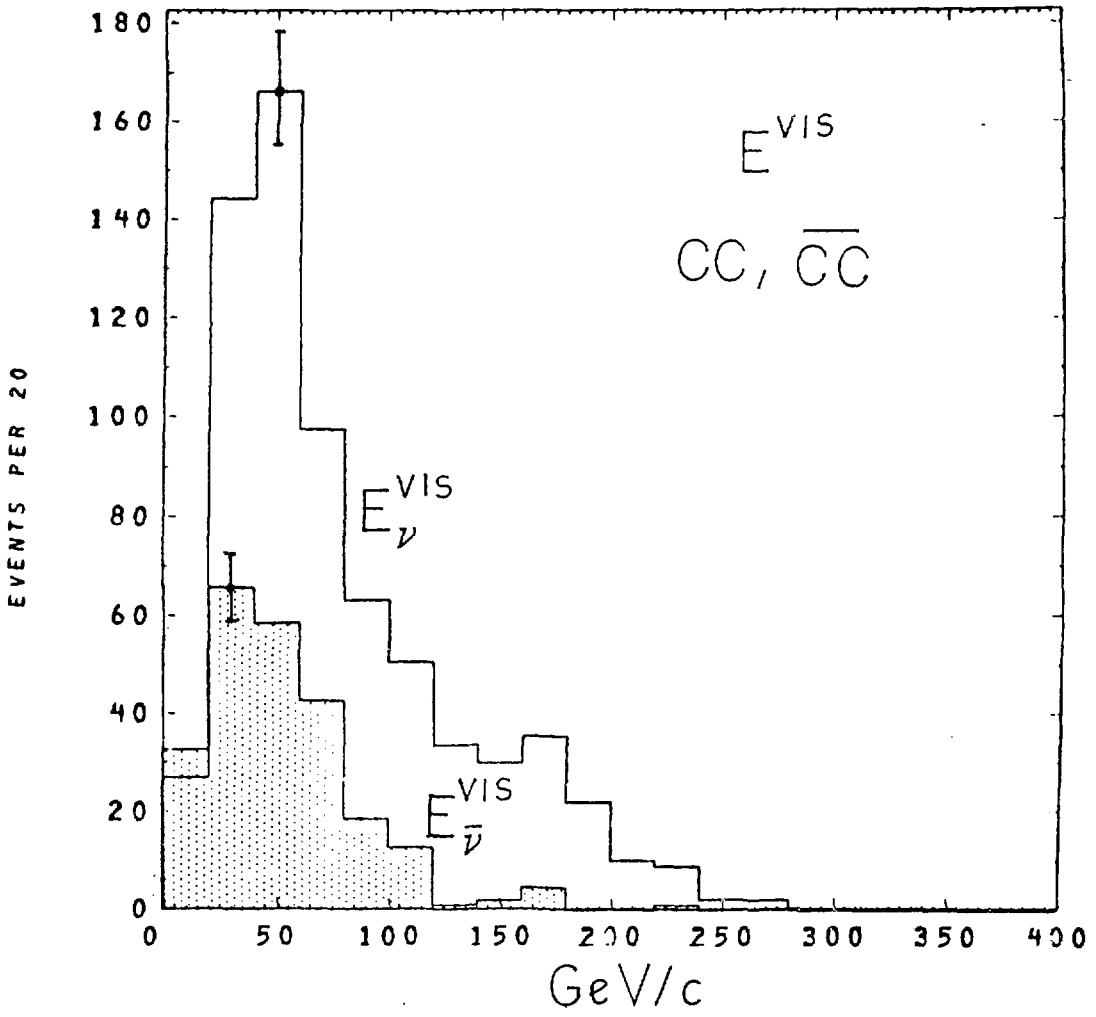
EVENTS PER 20
180
160
140
120
100
80
60
40
20
0
0
50
100
150
200
250
300
350
400
GeV/c
E^{VIS}
CC, $\overline{CC}$
E^{VIS}_{ν}
$E^{VIS}_{\bar{\nu}}$

Fig. 7.2a

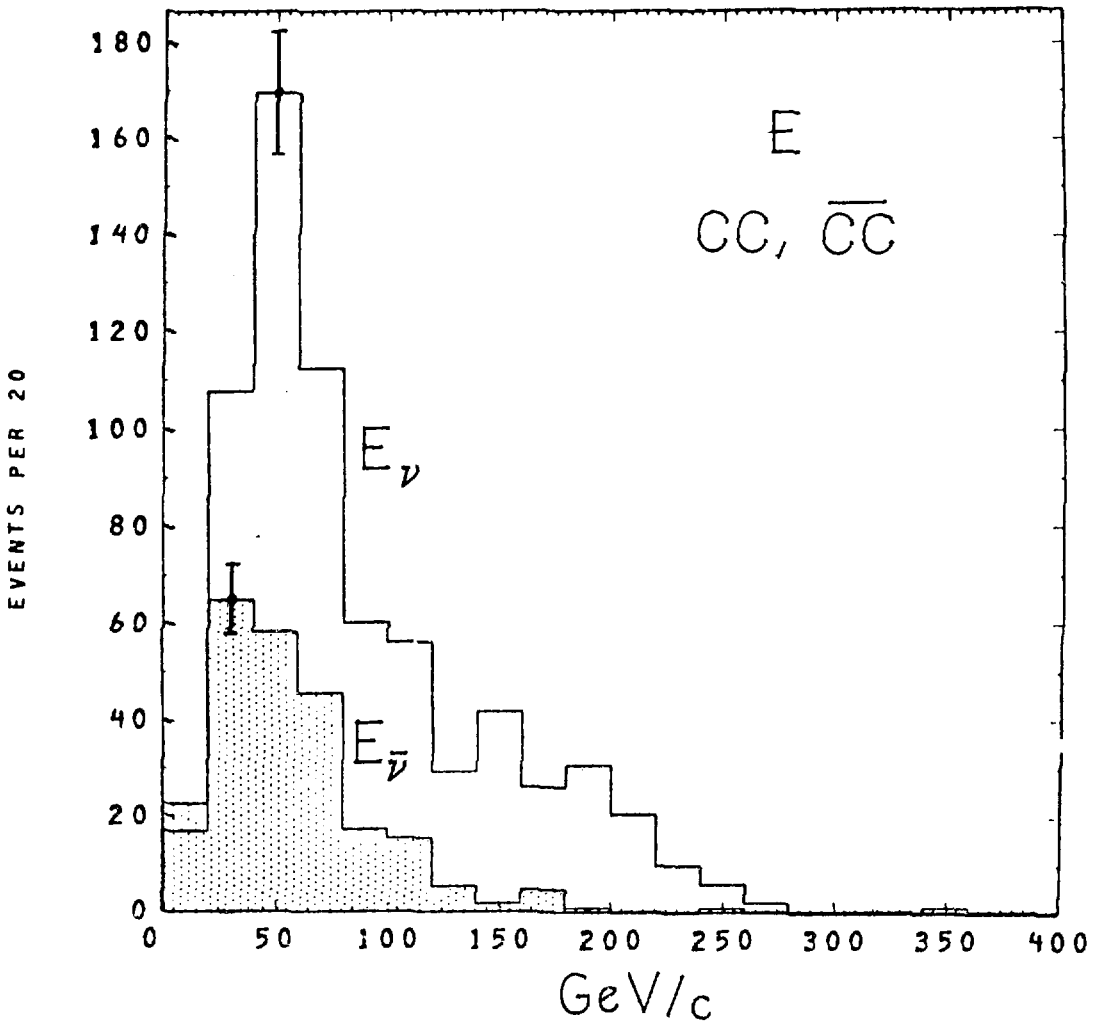
E
CC, $\overline{CC}$
E_ν
$E_{\bar{\nu}}$
EVENTS PER 20
0
20
40
60
80
100
120
140
160
180
0
50
100
150
200
250
300
350
400
GeV/c

Fig. 7.2b

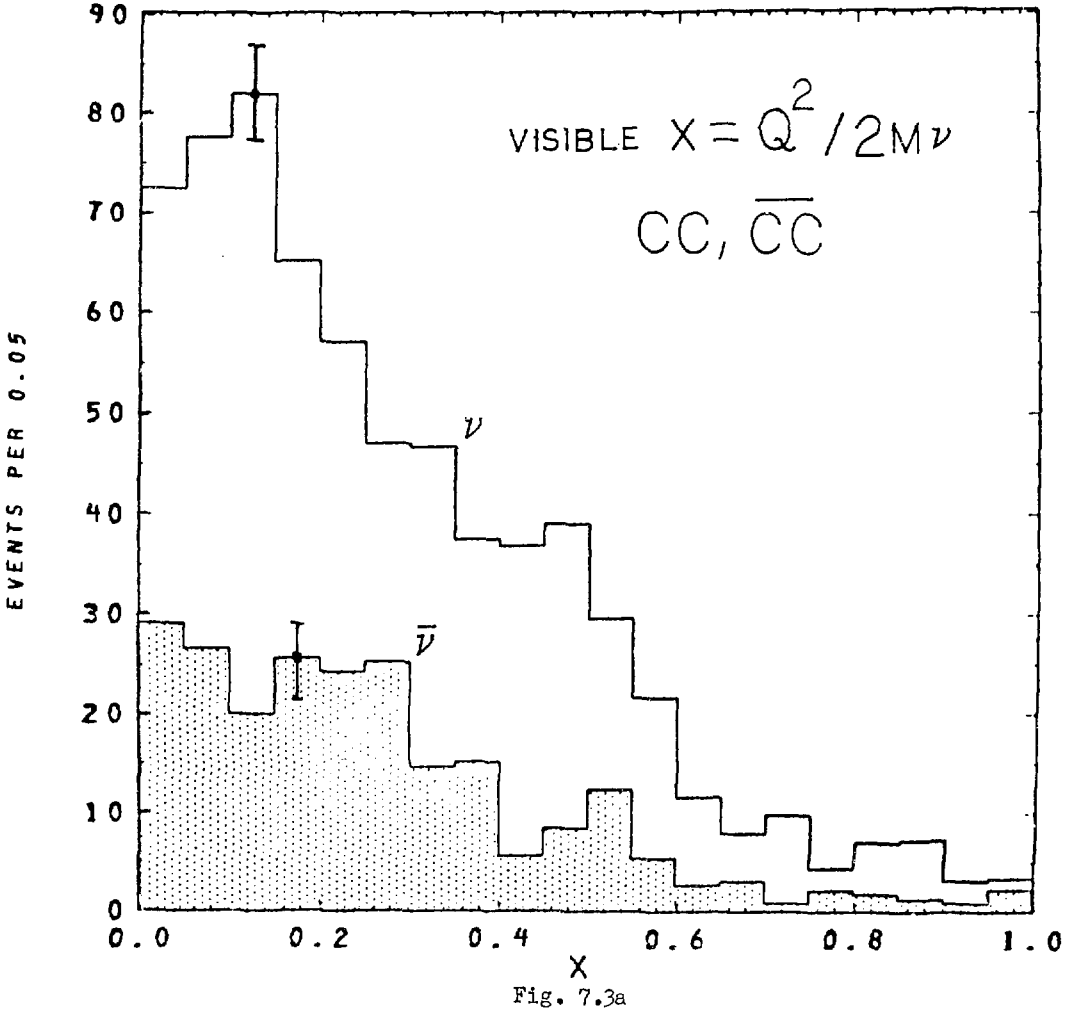
VISIBLE $X = Q^2/2M\nu$
$CC, \overline{CC}$
ν
$\bar{\nu}$
EVENTS PER 0.05
X
0.0
0.2
0.4
0.6
0.8
1.0
0
10
20
30
40
50
60
70
80
90

Fig. 7.3a

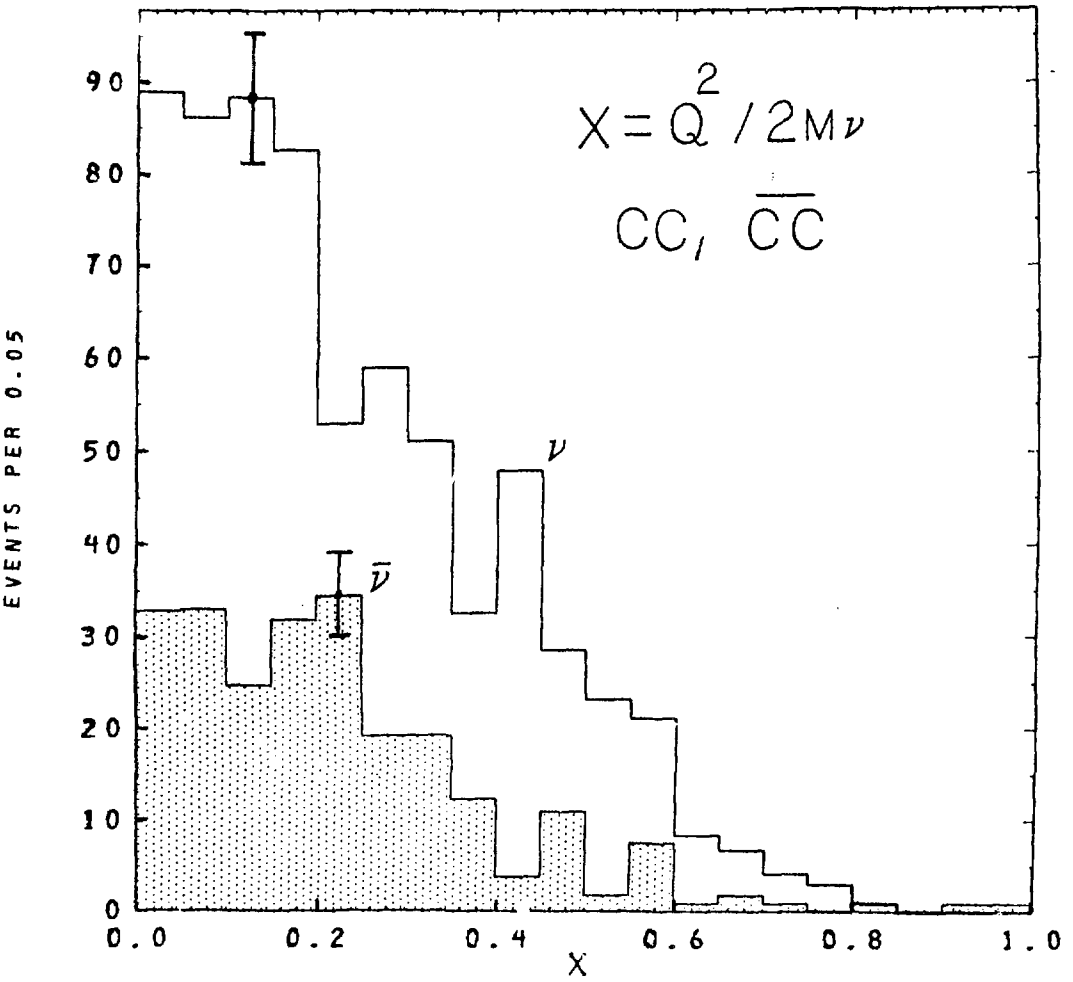
$X = Q^2 / 2M\nu$
CC, $\overline{CC}$
ν
$\bar{\nu}$
EVENTS PER 0.05
X
0
10
20
30
40
50
60
70
80
90
0.0
0.2
0.4
0.6
0.8
1.0

Fig. 7.3b

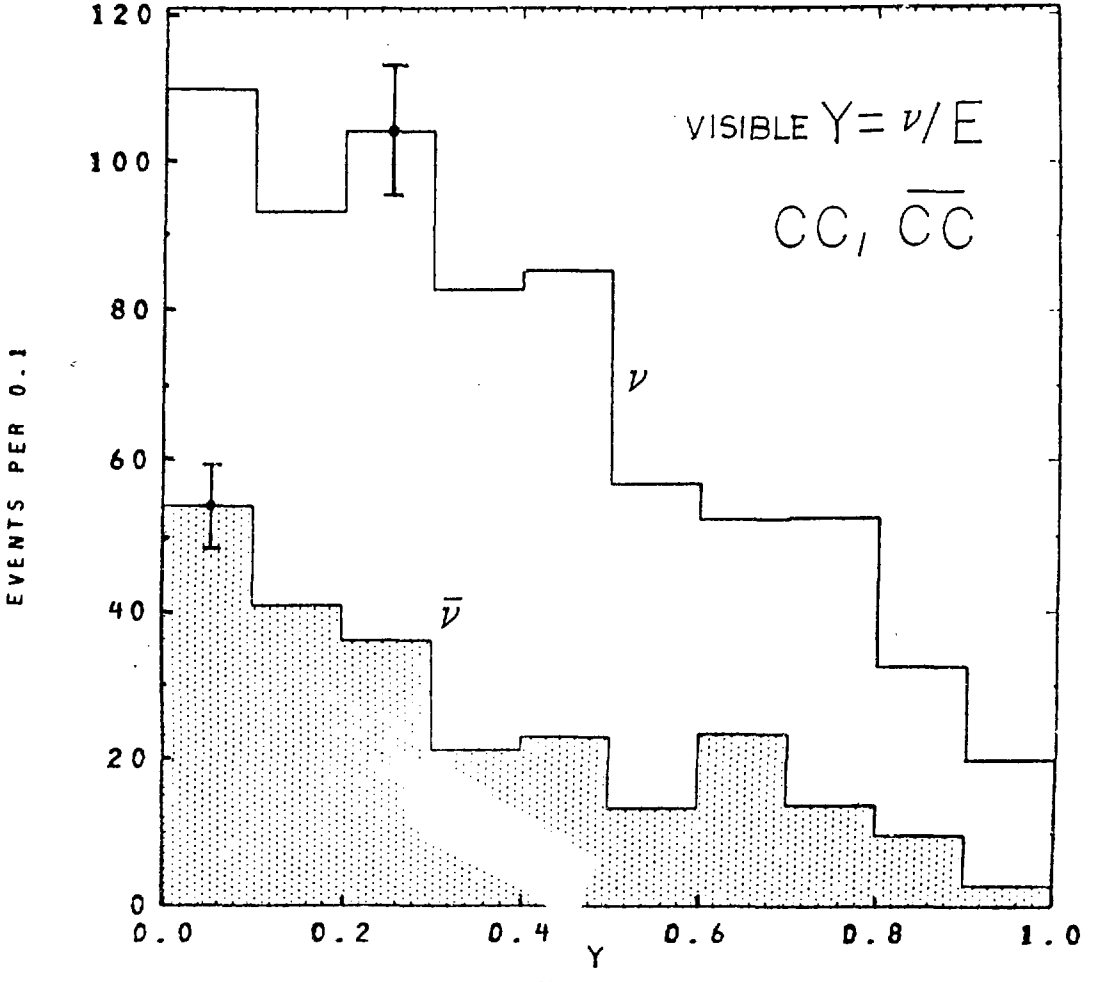
120
100
80
60
40
20
0
EVENTS PER 0.1
VISIBLE Y = ν/E
CC, $\overline{CC}$
ν
$\bar{\nu}$
0.0
0.2
0.4
0.6
0.8
1.0
Y

Fig. 7.4a

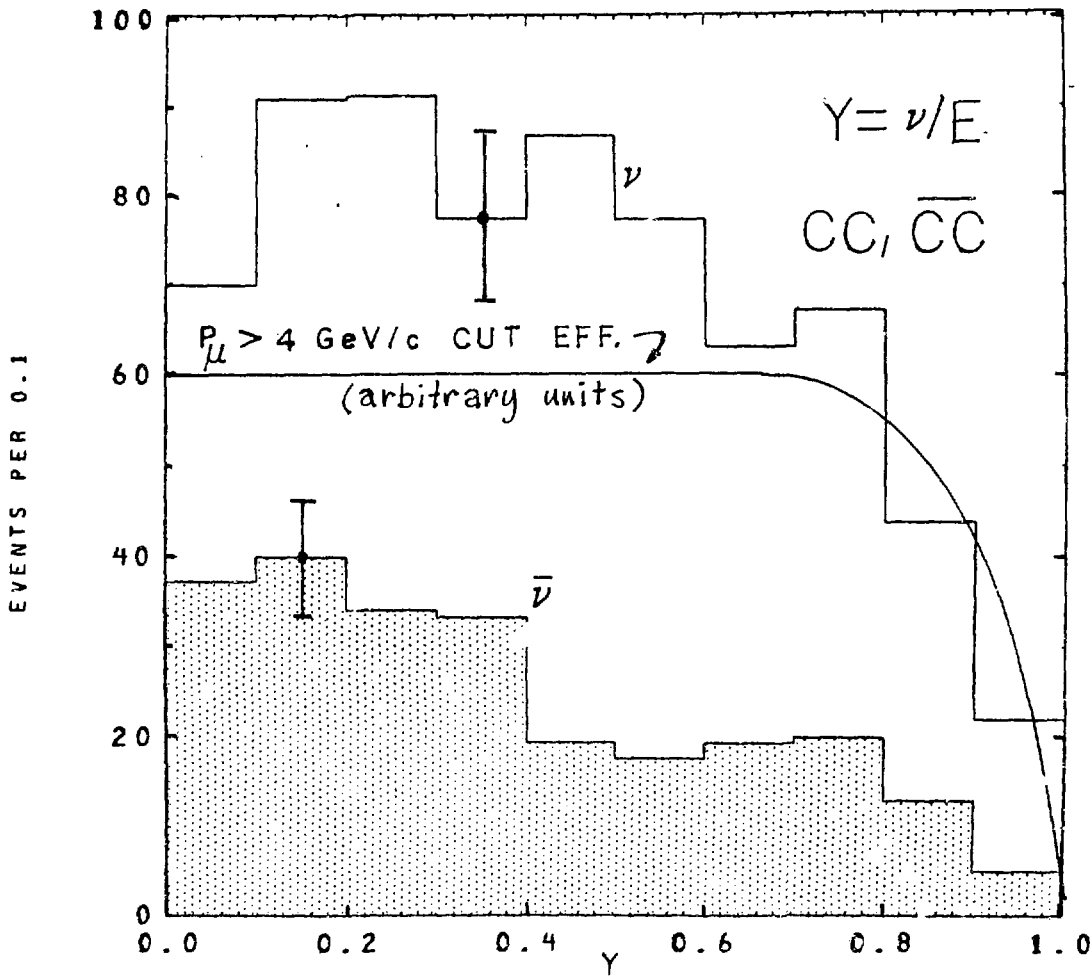
100
80
60
40
20
0
0.0
0.2
0.4
0.6
0.8
1.0
Y
EVENTS PER 0.1
Y = ν/E
CC, $\overline{CC}$
ν
$\bar{\nu}$
$P_\mu > 4$ GeV/c CUT EFF. ?
(arbitrary units)

Fig. 7.4b

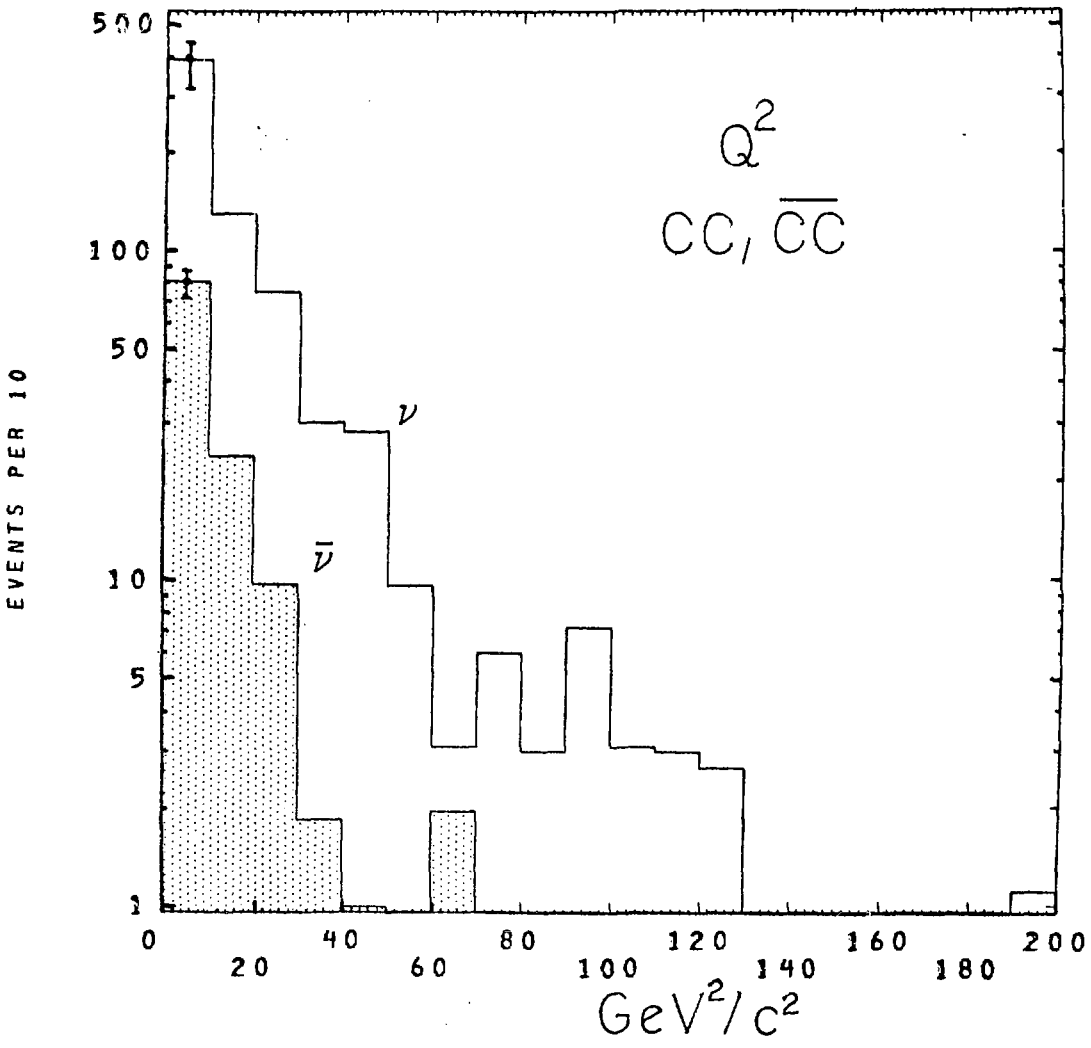
500
100
50
10
5
1
EVENTS PER 10
Q^2
CC, $\overline{CC}$
ν
$\bar{\nu}$
0
20
40
60
80
100
120
140
160
180
200
GeV^2/c^2

Fig. 7.5

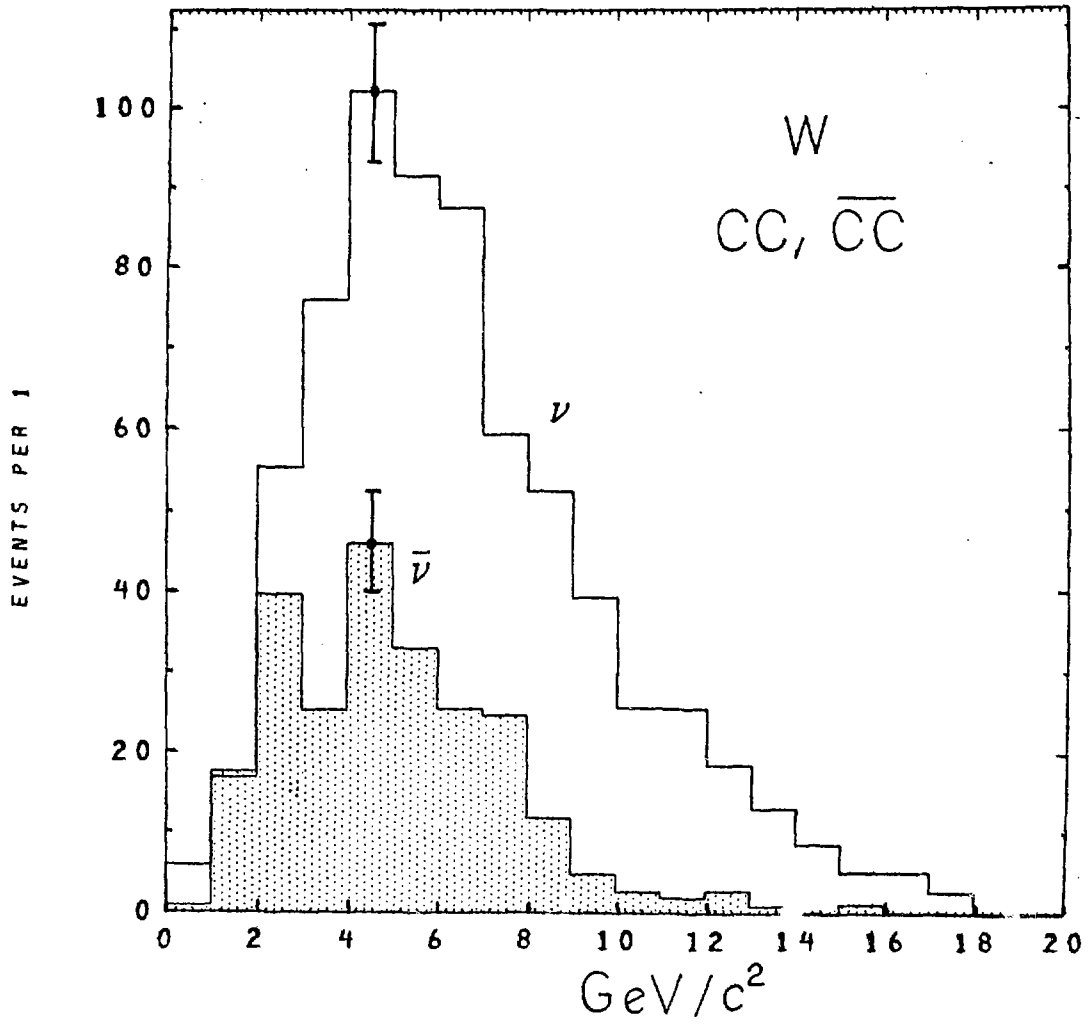
W
CC, $\overline{CC}$
ν
$\bar{\nu}$
EVENTS PER 1
0
20
40
60
80
100
0
2
4
6
8
10
12
14
16
18
20
GeV/c^2

Fig. 7.6

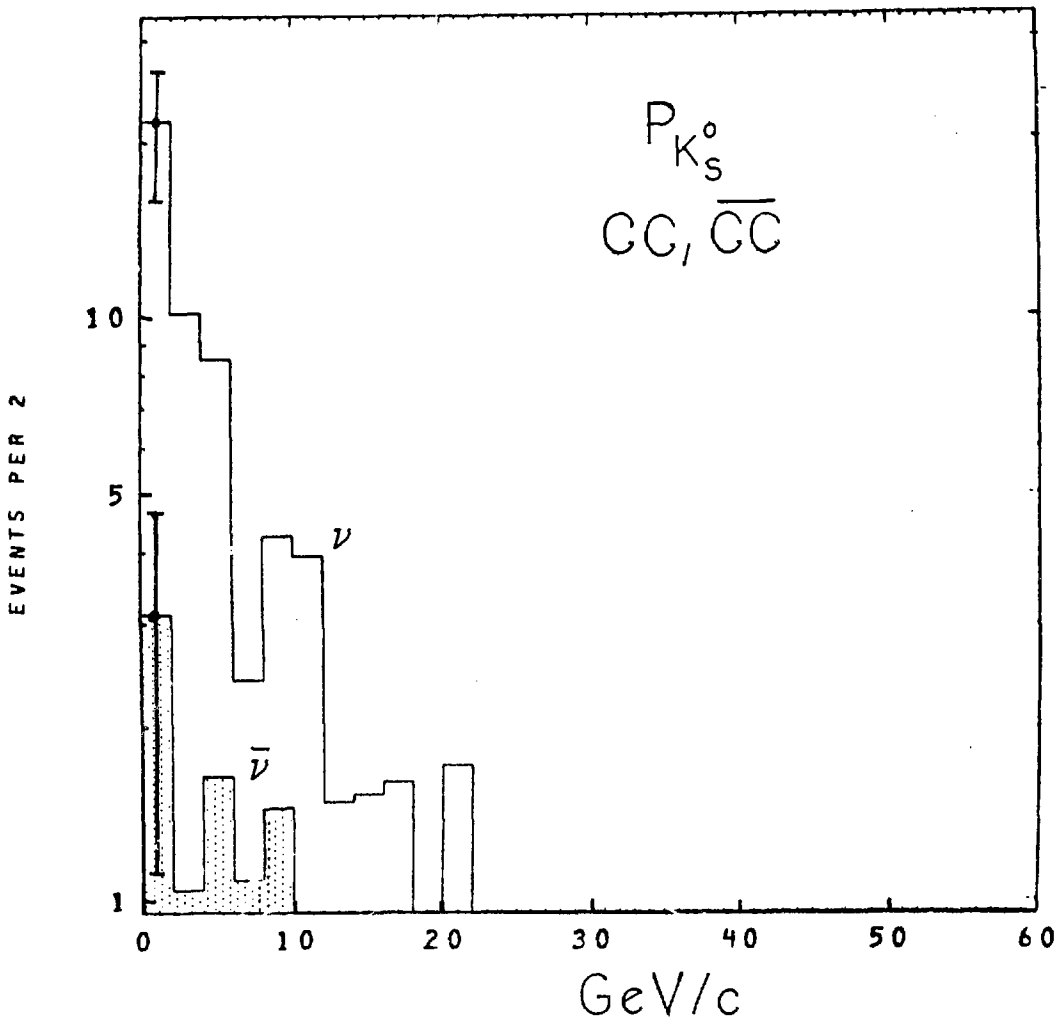
$P_{K^0_S}$
CC, $\overline{CC}$
EVENTS PER 2
10
5
1
ν
$\bar{\nu}$
0
10
20
30
40
50
60
GeV/c

Fig. 7.7a

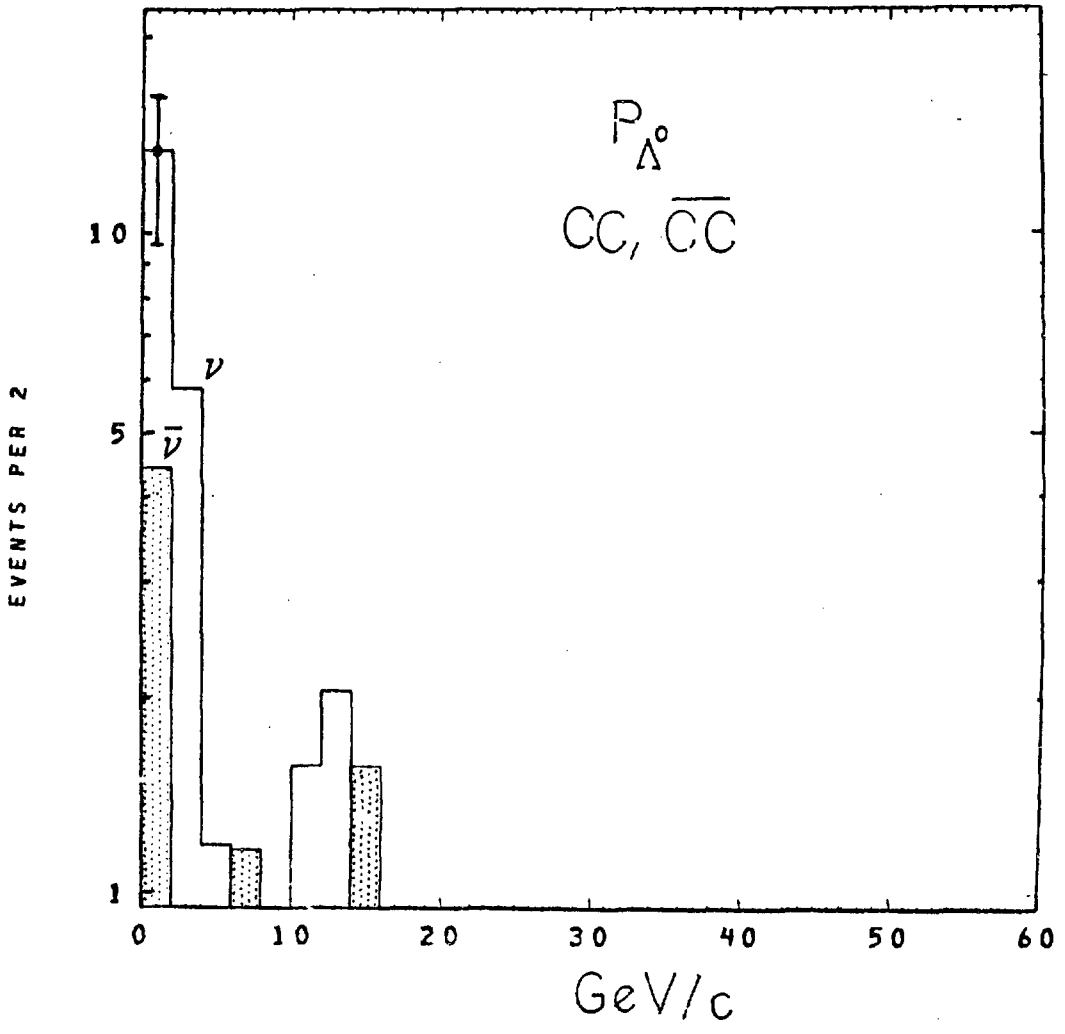
P_{Λ^0}
CC, $\overline{CC}$
ν
$\bar{\nu}$
EVENTS PER 2
10
5
1
0
10
20
30
40
50
60
GeV/c

Fig. 7.7b

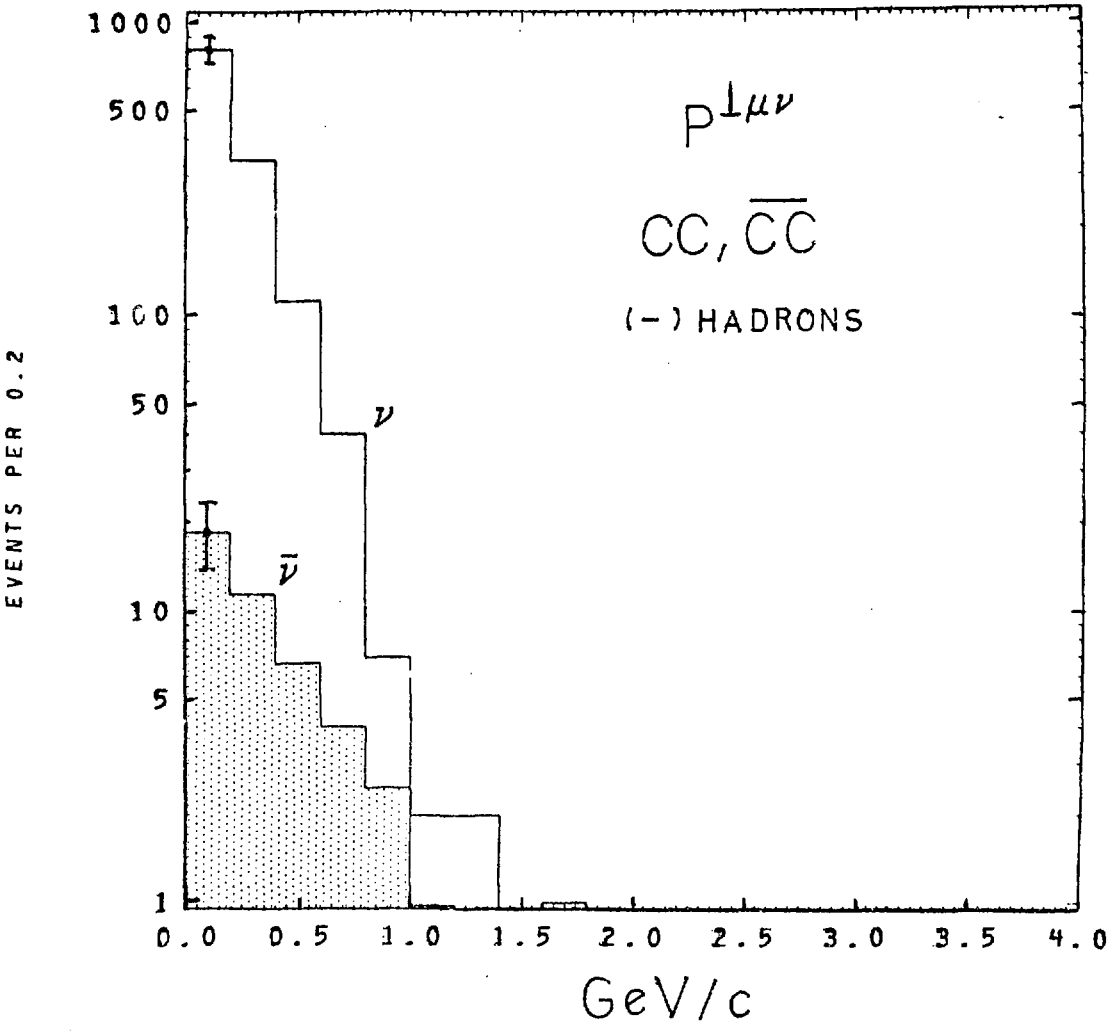
1000
500
100
50
10
5
1
EVENTS PER 0.2
$p^{\perp\mu\nu}$
CC, $\overline{CC}$
(-) HADRONS
ν
$\bar{\nu}$
0.0
0.5
1.0
1.5
2.0
2.5
3.0
3.5
4.0
GeV/c

Fig. 7.8b

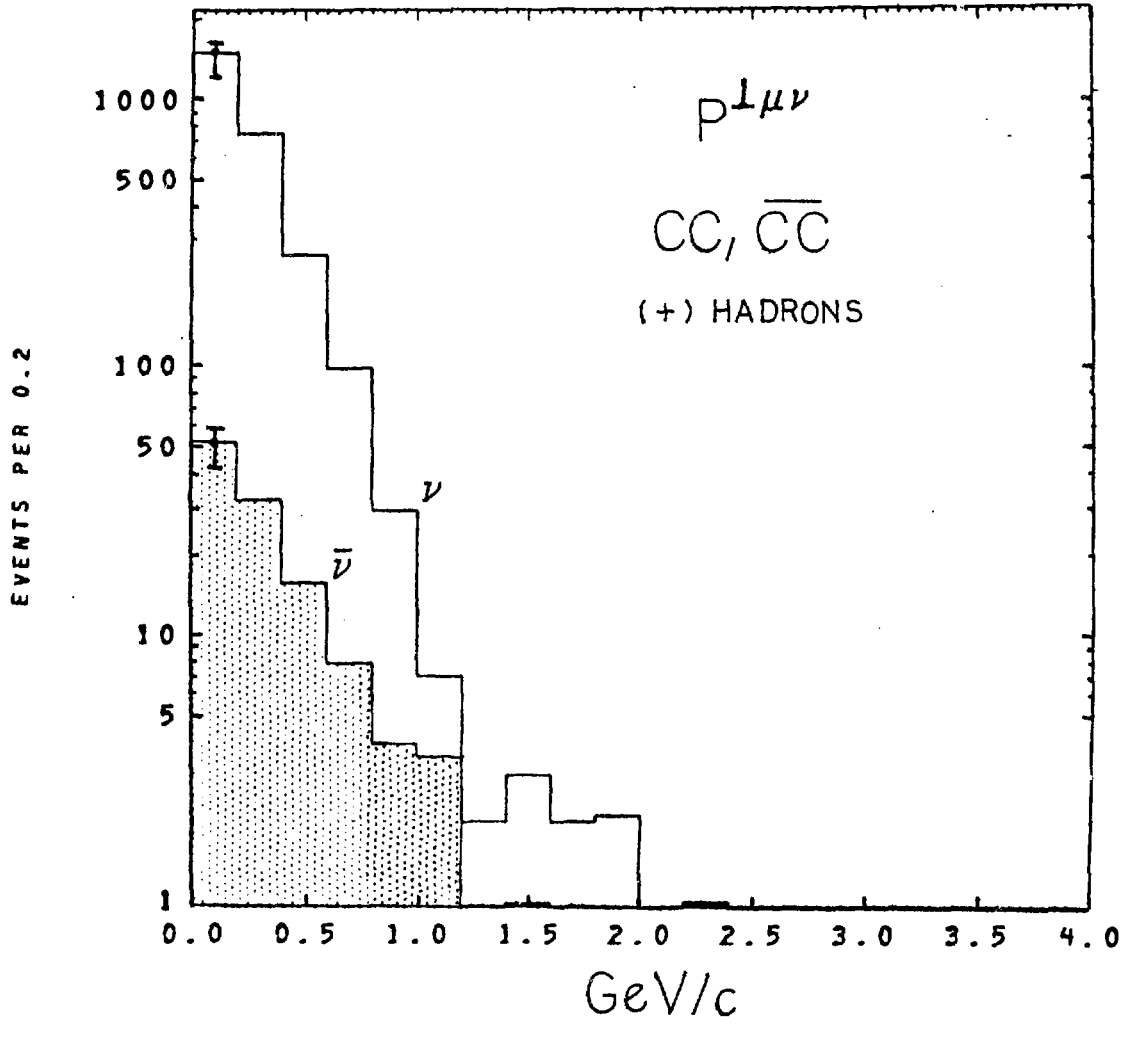
$p^{\perp}\mu\nu$
CC, $\overline{CC}$
(+) HADRONS
ν
$\bar{\nu}$
EVENTS PER 0.2
1000
500
100
50
10
5
1
0.0
0.5
1.0
1.5
2.0
2.5
3.0
3.5
4.0
GeV/c

Fig. 7.8a

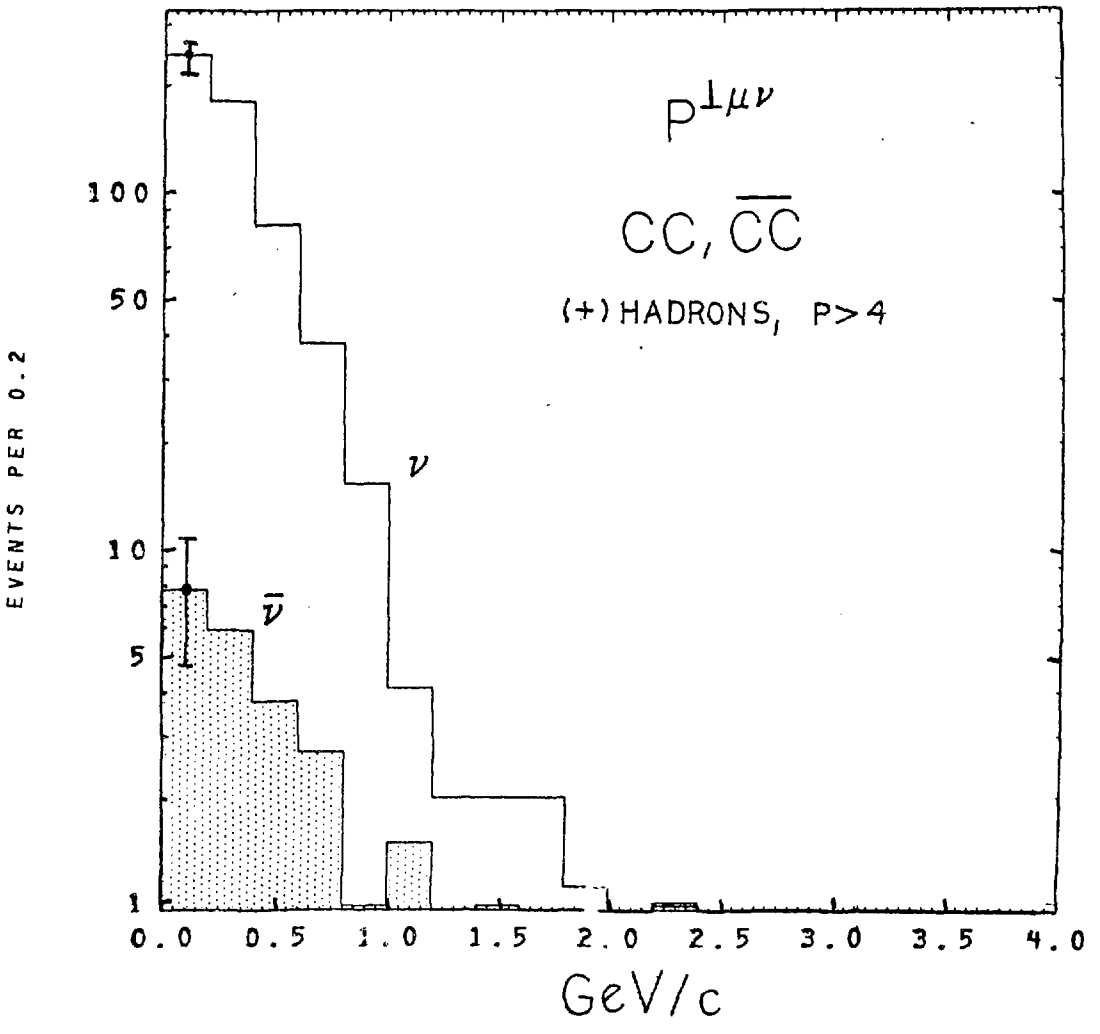
$P^{\perp\mu\nu}$
CC, $\overline{CC}$
(+) HADRONS, P>4
ν
$\bar{\nu}$
EVENTS PER 0.2
100
50
10
5
1
0.0
0.5
1.0
1.5
2.0
2.5
3.0
3.5
4.0
GeV/c

Fig. 7.8c

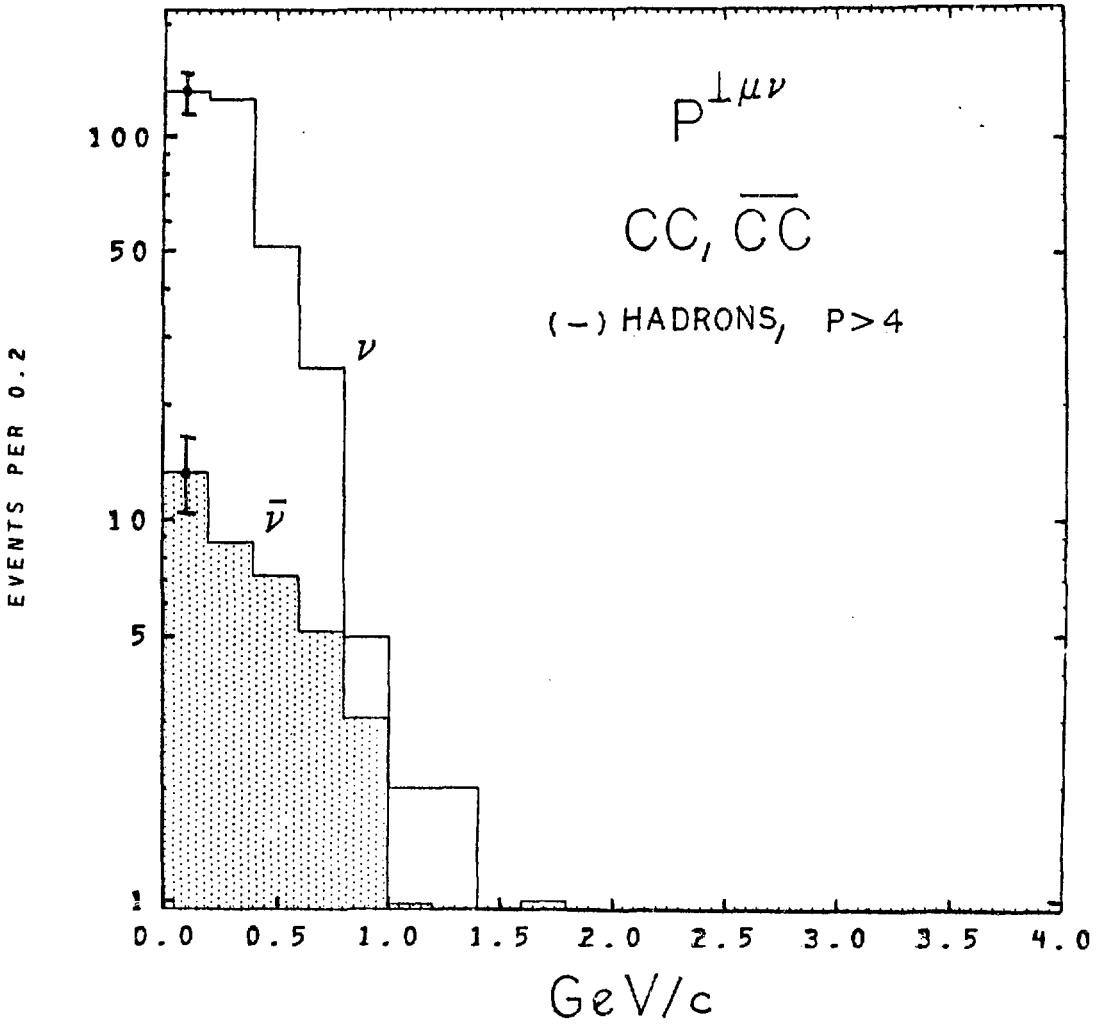
$P^{\perp\mu\nu}$
CC, $\overline{CC}$
(−) HADRONS, P>4
ν
$\bar{\nu}$
EVENTS PER 0.2
100
50
10
5
1
0.0
0.5
1.0
1.5
2.0
2.5
3.0
3.5
4.0
GeV/c

Fig. 7.8d

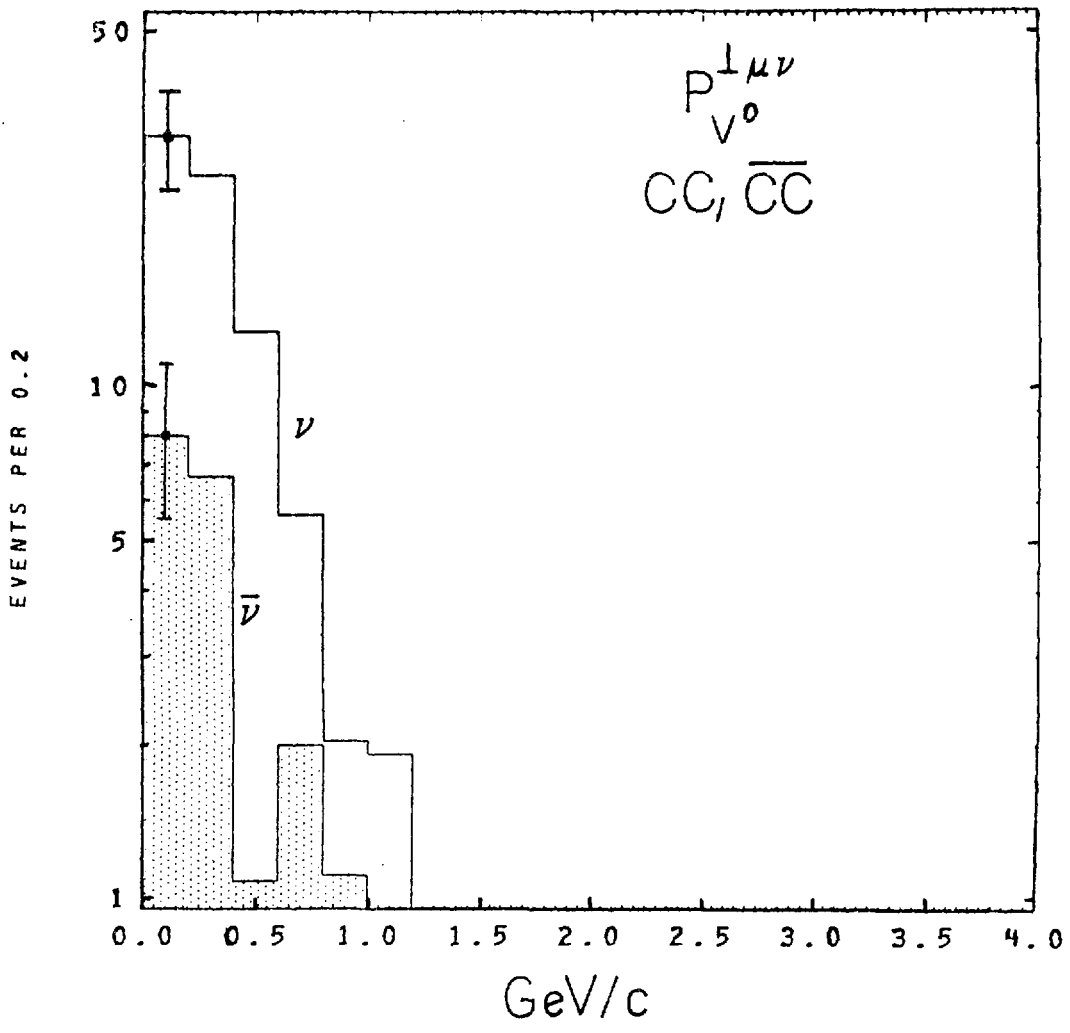
50
10
5
1
EVENTS PER 0.2
$P_{V^0}^{\perp \mu\nu}$
CC, $\overline{CC}$
ν
$\bar{\nu}$
0.0
0.5
1.0
1.5
2.0
2.5
3.0
3.5
4.0
GeV/c

Fig. 7.8e

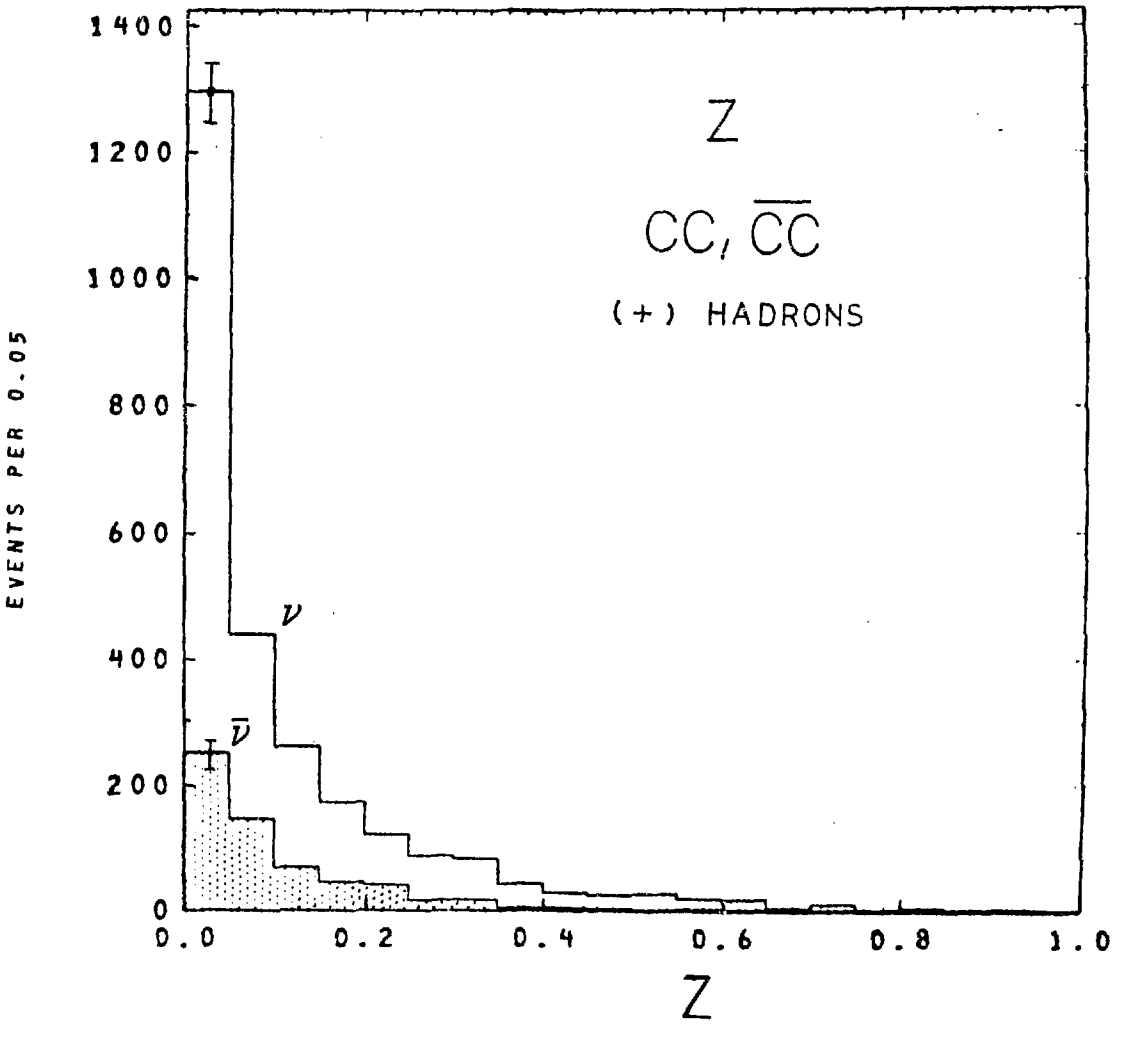
1400
1200
1000
800
600
400
200
0
EVENTS PER 0.05
Z
CC, $\overline{CC}$
(+) HADRONS
ν
$\bar{\nu}$
0.0
0.2
0.4
0.6
0.8
1.0
Z

Fig. 7.9a

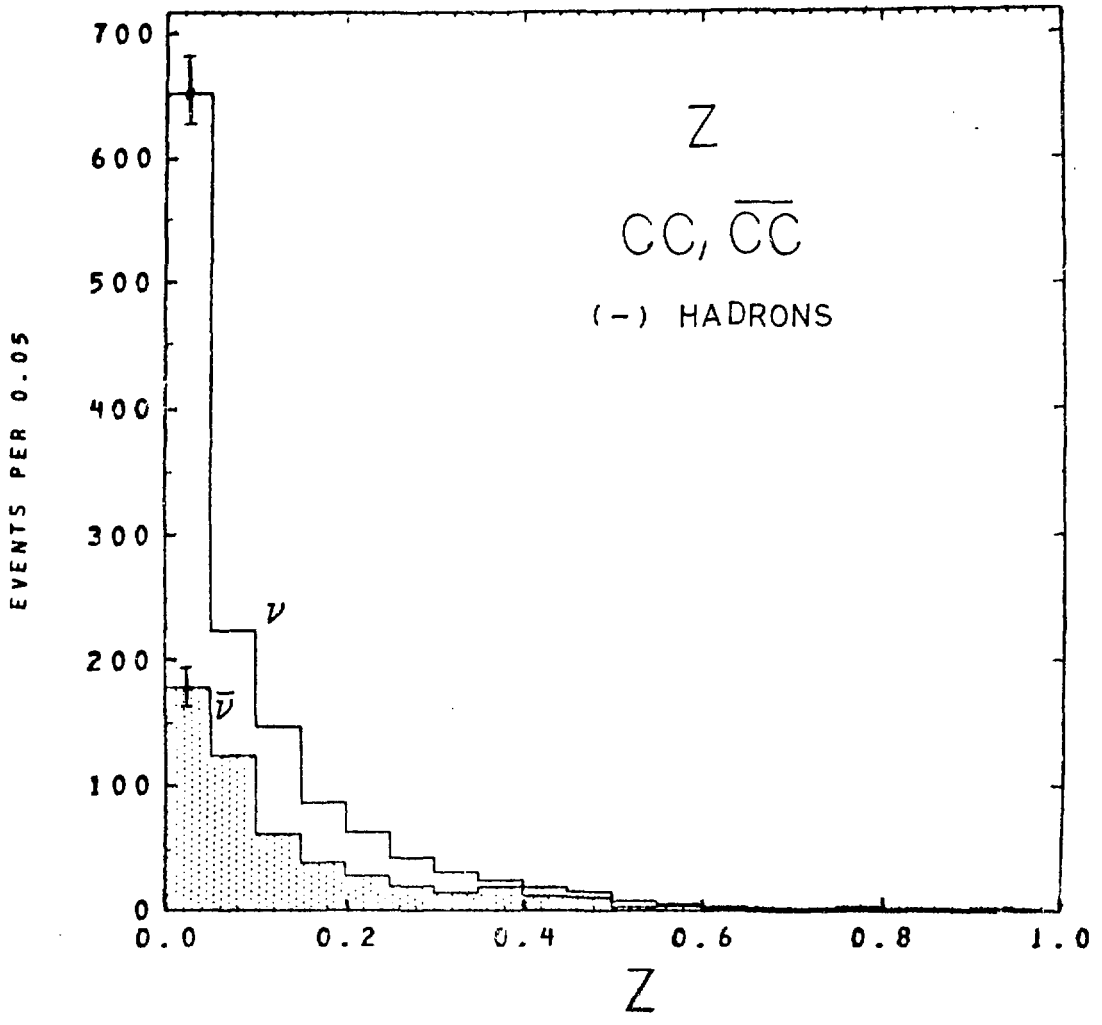
Z
CC, $\overline{CC}$
(-) HADRONS
ν
$\bar{\nu}$
EVENTS PER 0.05
700
600
500
400
300
200
100
0
0.0
0.2
0.4
0.6
0.8
1.0
Z

Fig. 7.9b

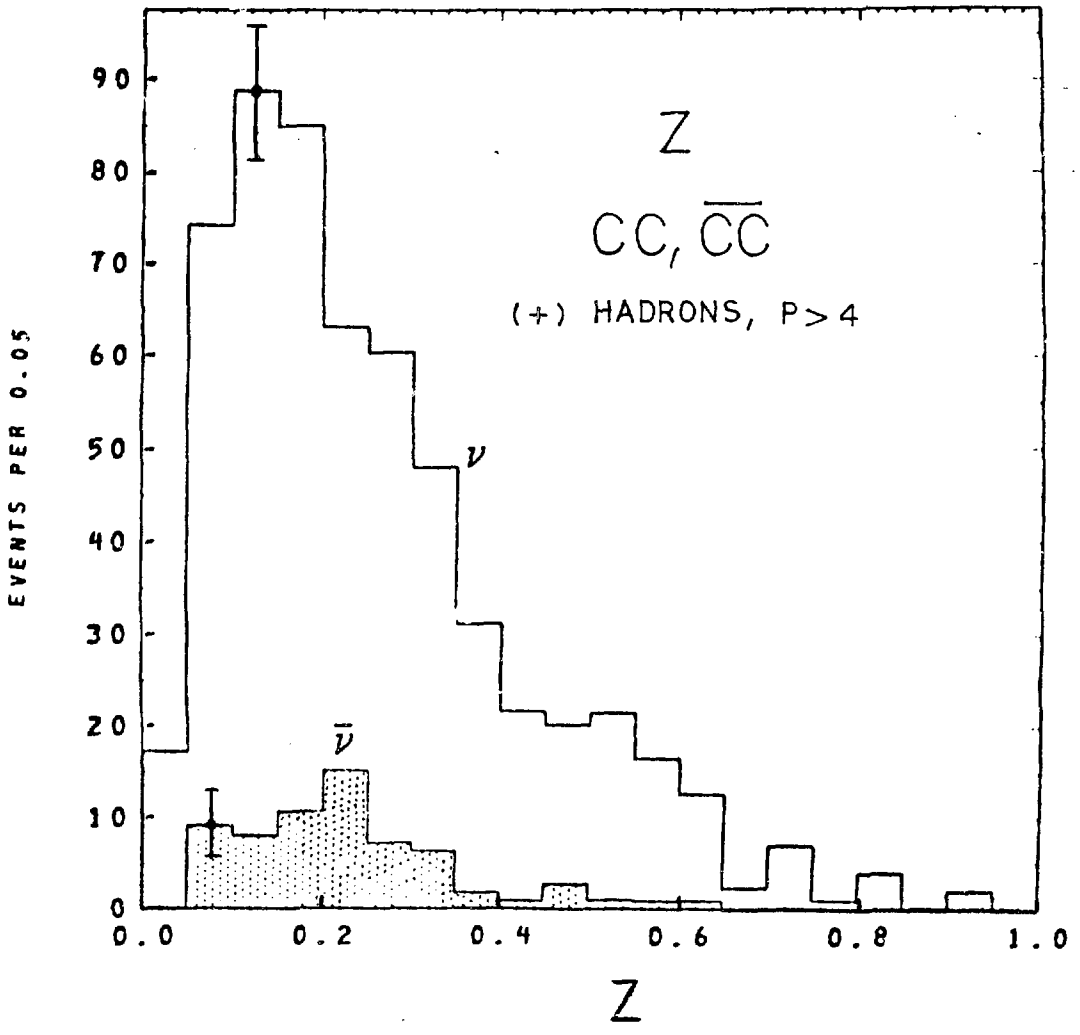
Z
CC, $\overline{CC}$
(+) HADRONS, P>4
ν
$\bar{\nu}$
EVENTS PER 0.05
0
10
20
30
40
50
60
70
80
90
0.0
0.2
0.4
0.6
0.8
1.0
Z

Fig. 7.9c

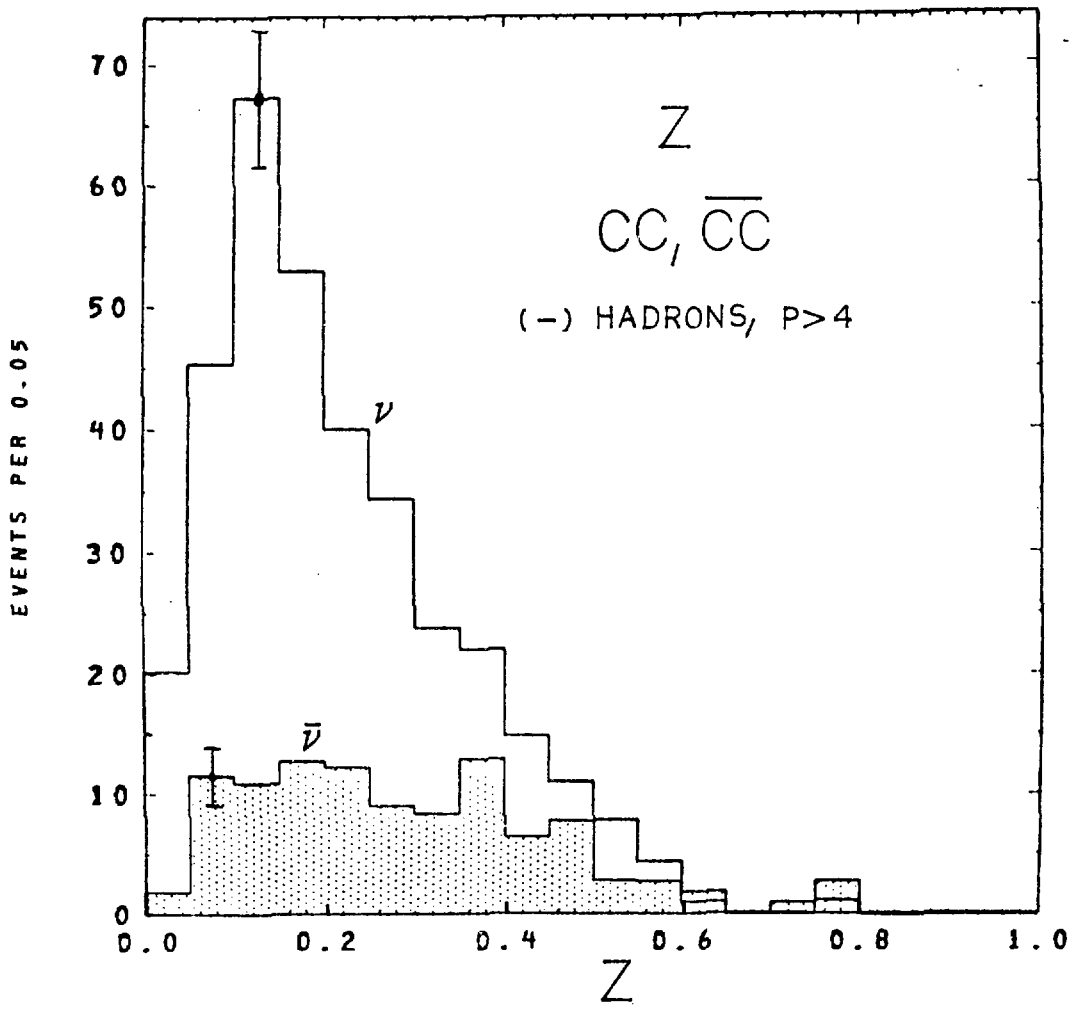
Z
CC, $\overline{CC}$
(-) HADRONS, P>4
ν
$\bar{\nu}$
EVENTS PER 0.05
0
10
20
30
40
50
60
70
0.0
0.2
0.4
0.6
0.8
1.0
Z

Fig. 7.9d

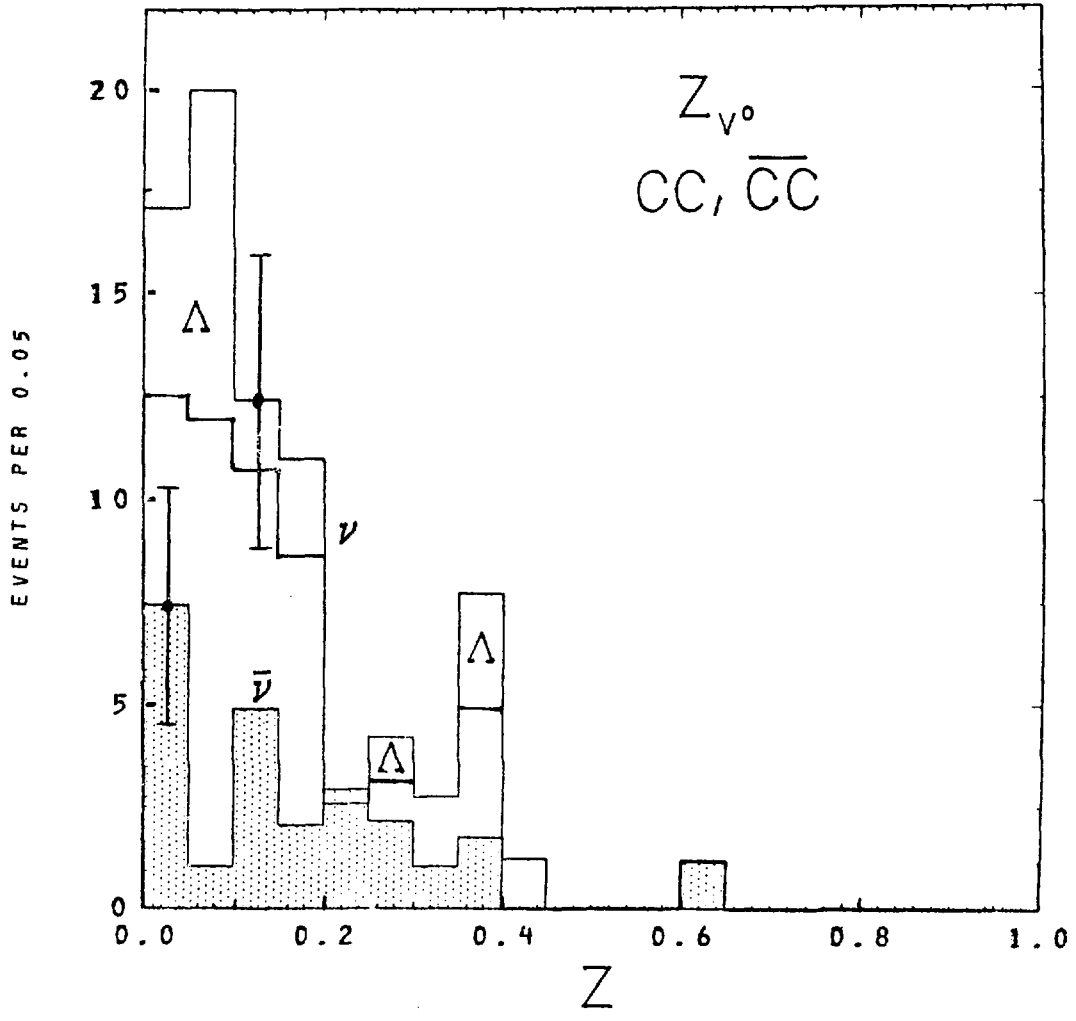
Z_{V^0}
$CC, \overline{CC}$
Λ
ν
$\bar{\nu}$
Λ
Λ
EVENTS PER 0.05
20
15
10
5
0
0.0
0.2
0.4
0.6
0.8
1.0
Z

Fig. 7.9e

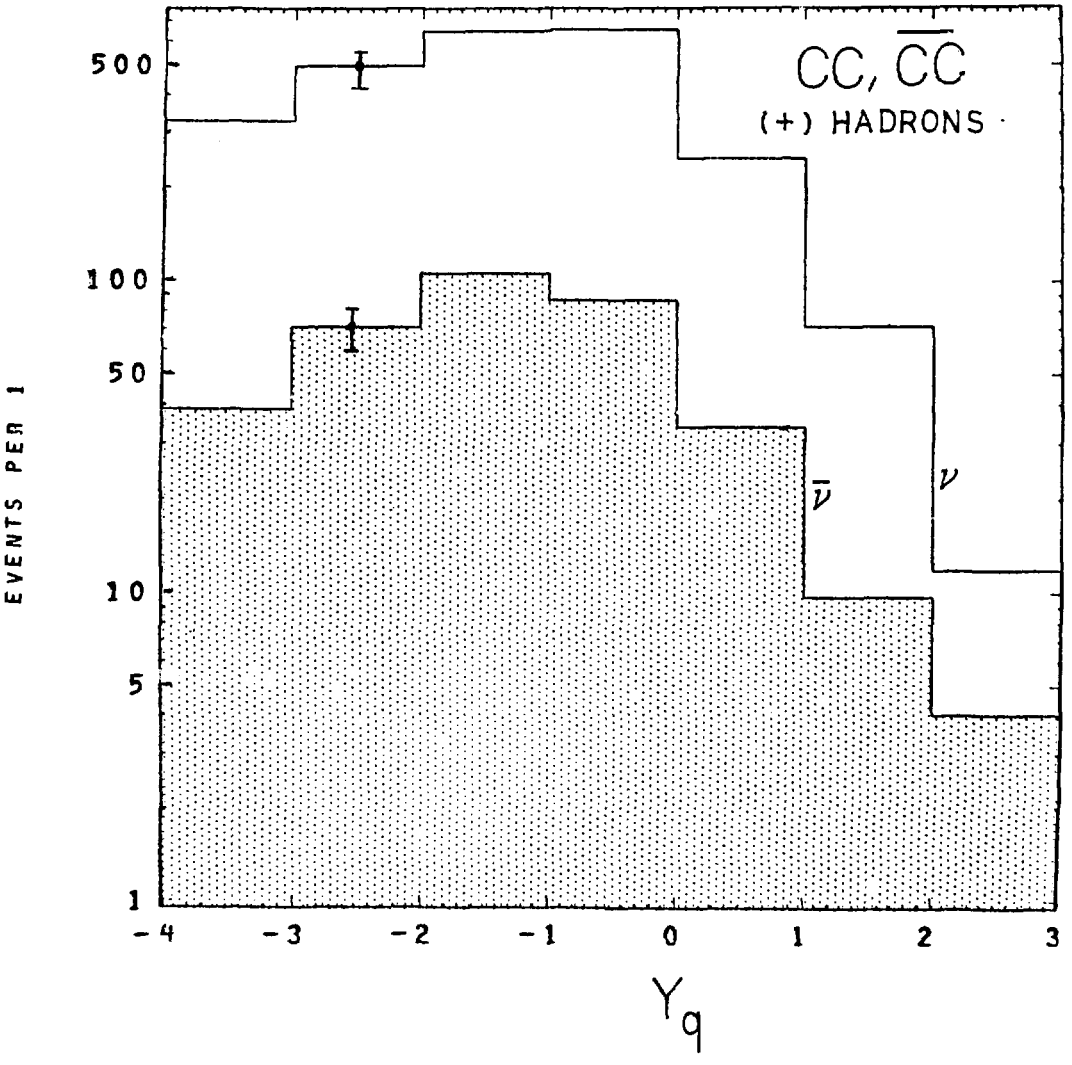
CC, $\overline{CC}$
(+) HADRONS
$\bar{\nu}$
ν
EVENTS PER 1
500
100
50
10
5
1
-4
-3
-2
-1
0
1
2
3
Y_q

Fig. 7.10a

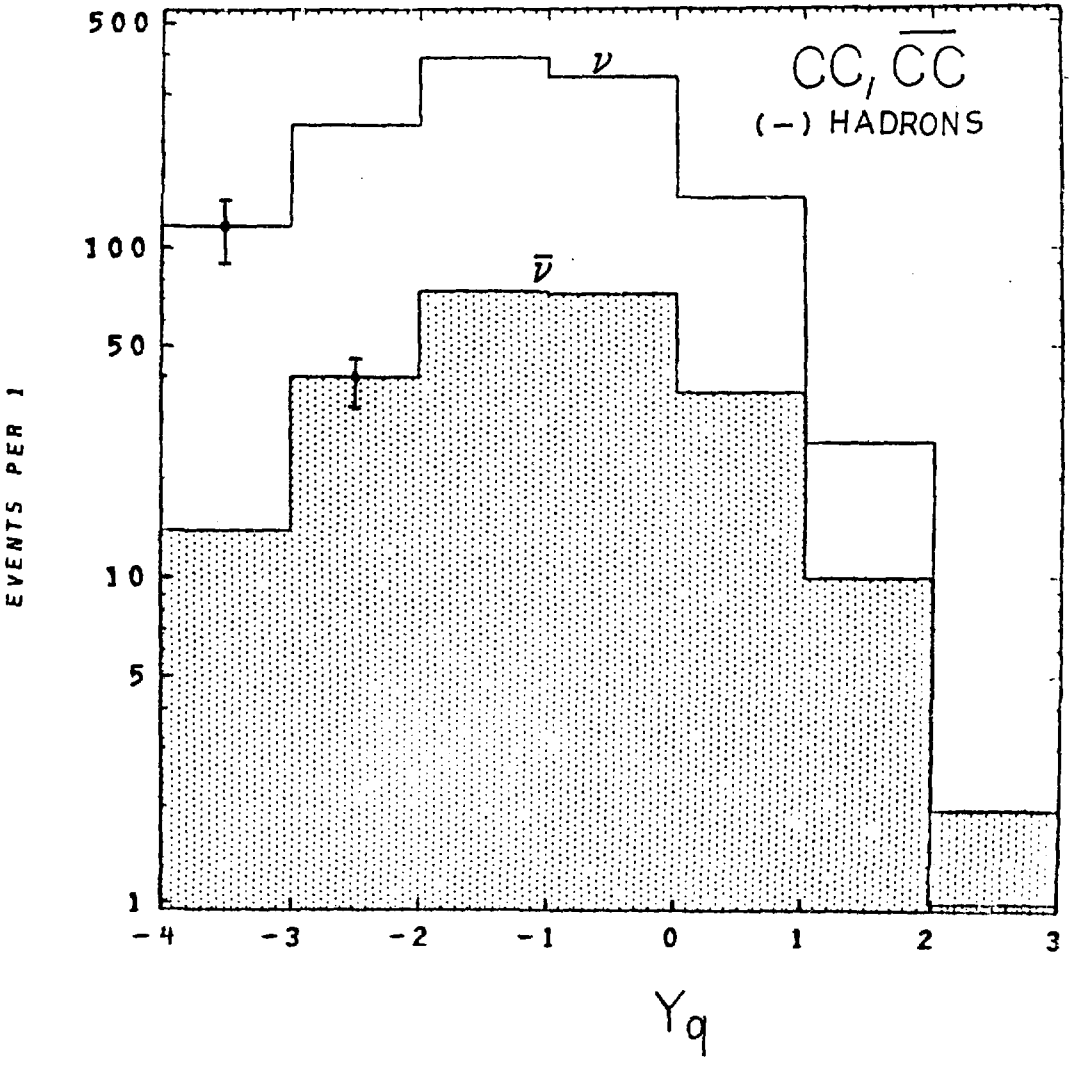

Fig. 7.10b

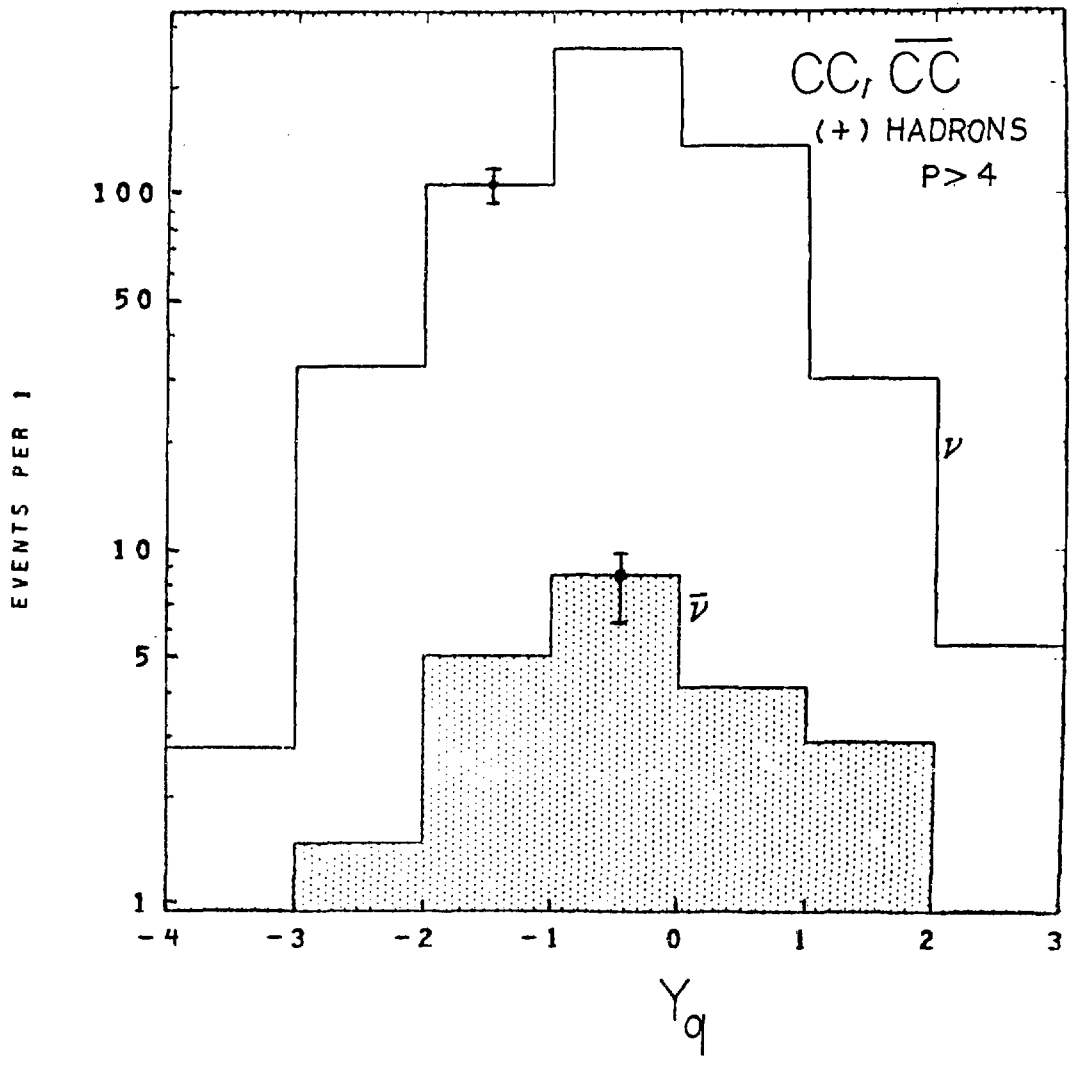
CC, $\overline{CC}$
(+) HADRONS
P> 4
ν
$\bar{\nu}$
EVENTS PER 1
100
50
10
5
1
-4
-3
-2
-1
0
1
2
3
Y_q

Fig. 7.10c

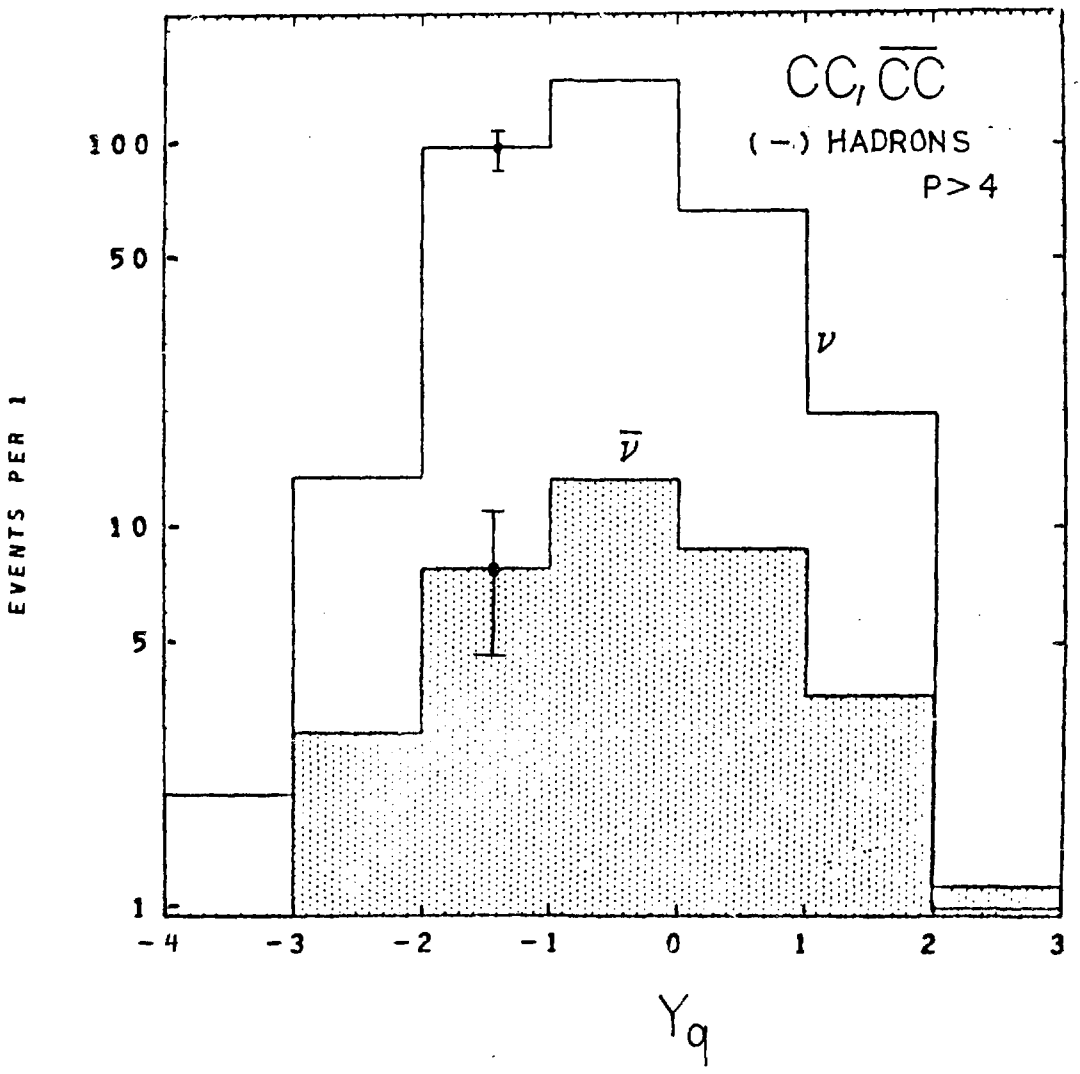
CC, $\overline{CC}$
(−) HADRONS
P>4
ν
$\overline{\nu}$
EVENTS PER 1
100
50
10
5
1
−4
−3
−2
−1
0
1
2
3
Y_q

Fig. 7.10d

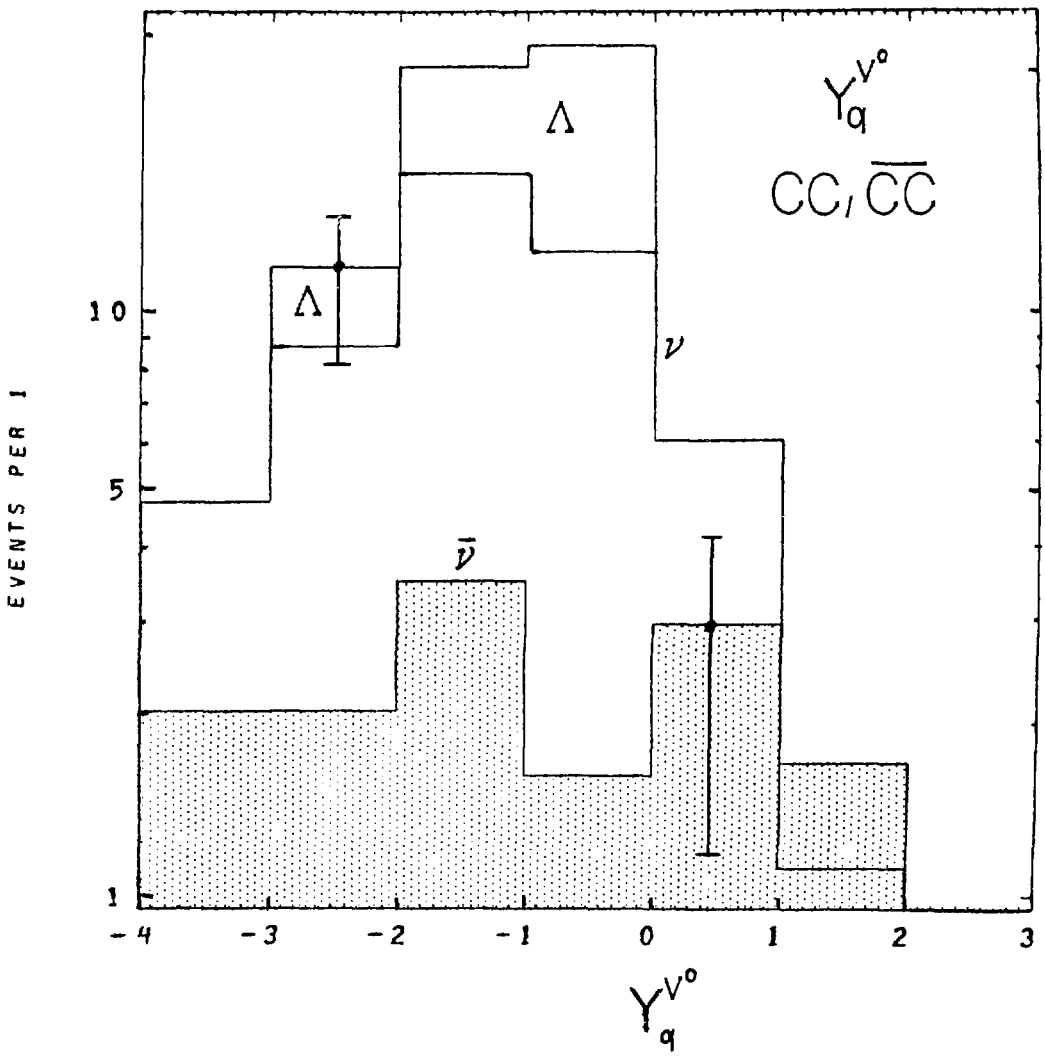

Fig. 7.10e

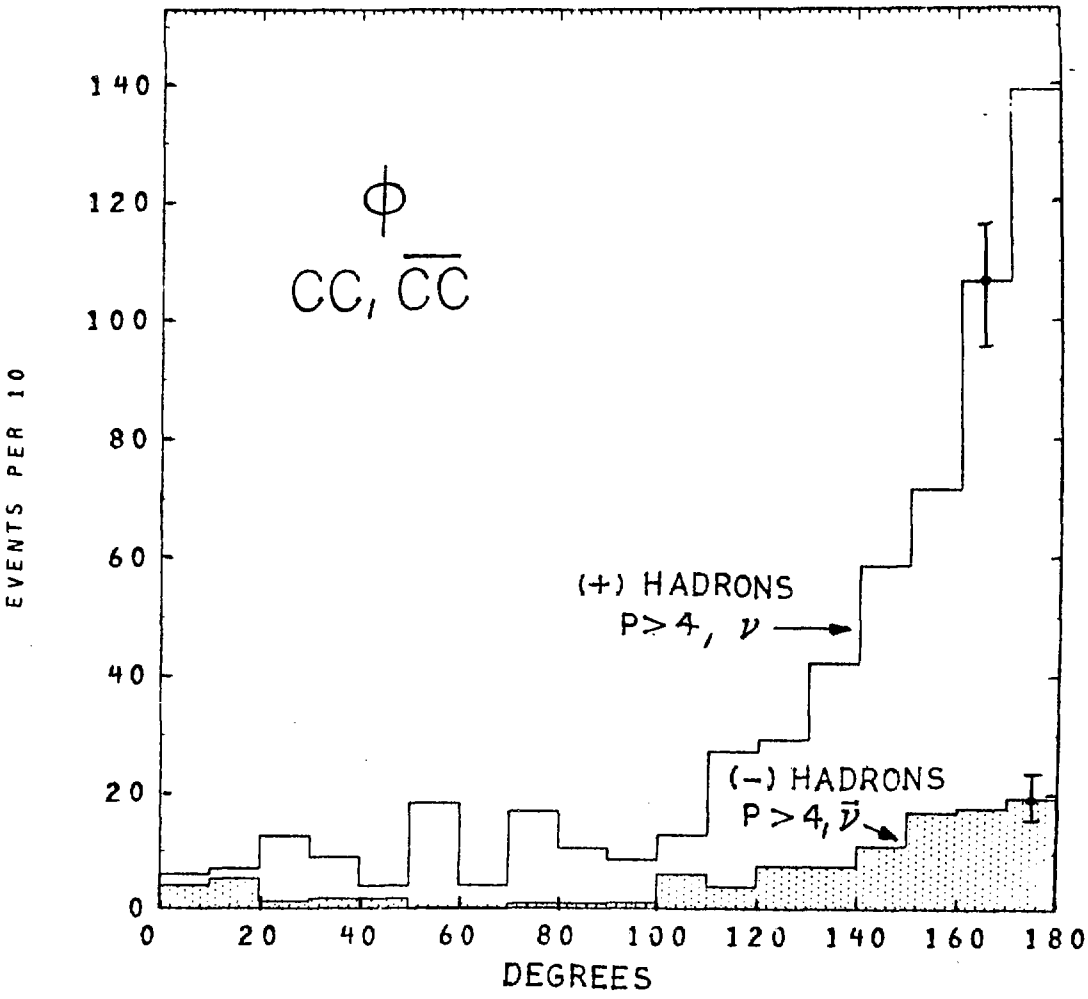
EVENTS PER 10
140
120
100
80
60
40
20
0
φ
CC, $\overline{CC}$
(+) HADRONS
P>4, ν
(-) HADRONS
P>4, $\bar{\nu}$
0
20
40
60
80
100
120
140
160
180
DEGREES

Fig. 7.11

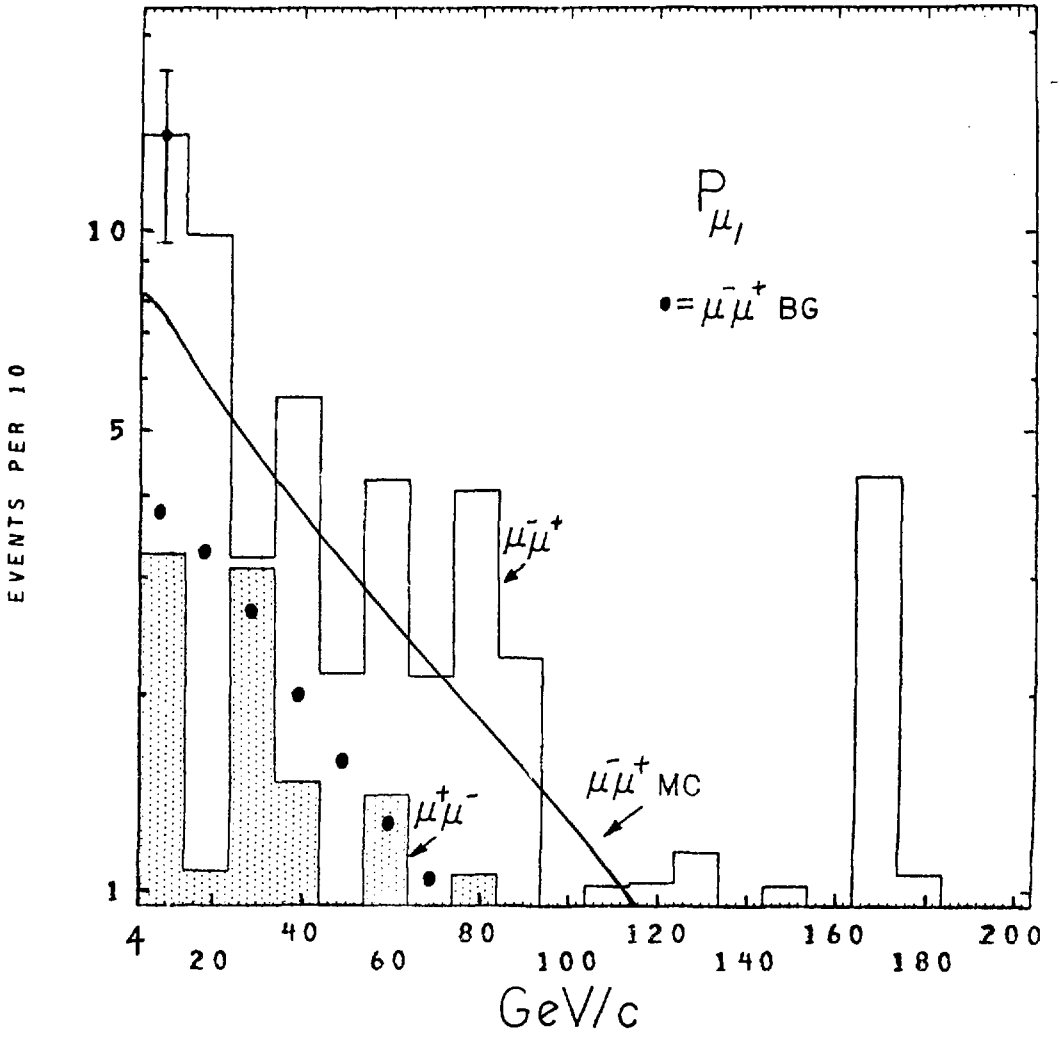
EVENTS PER 10
10
5
1
4
20
40
60
80
100
120
140
160
180
200
GeV/c
P_{μ_1}
• = $\mu^-\mu^+$ BG
$\mu^-\mu^+$
$\mu^-\mu^+$ MC
$\mu^+\mu^-$

Fig. 7.12

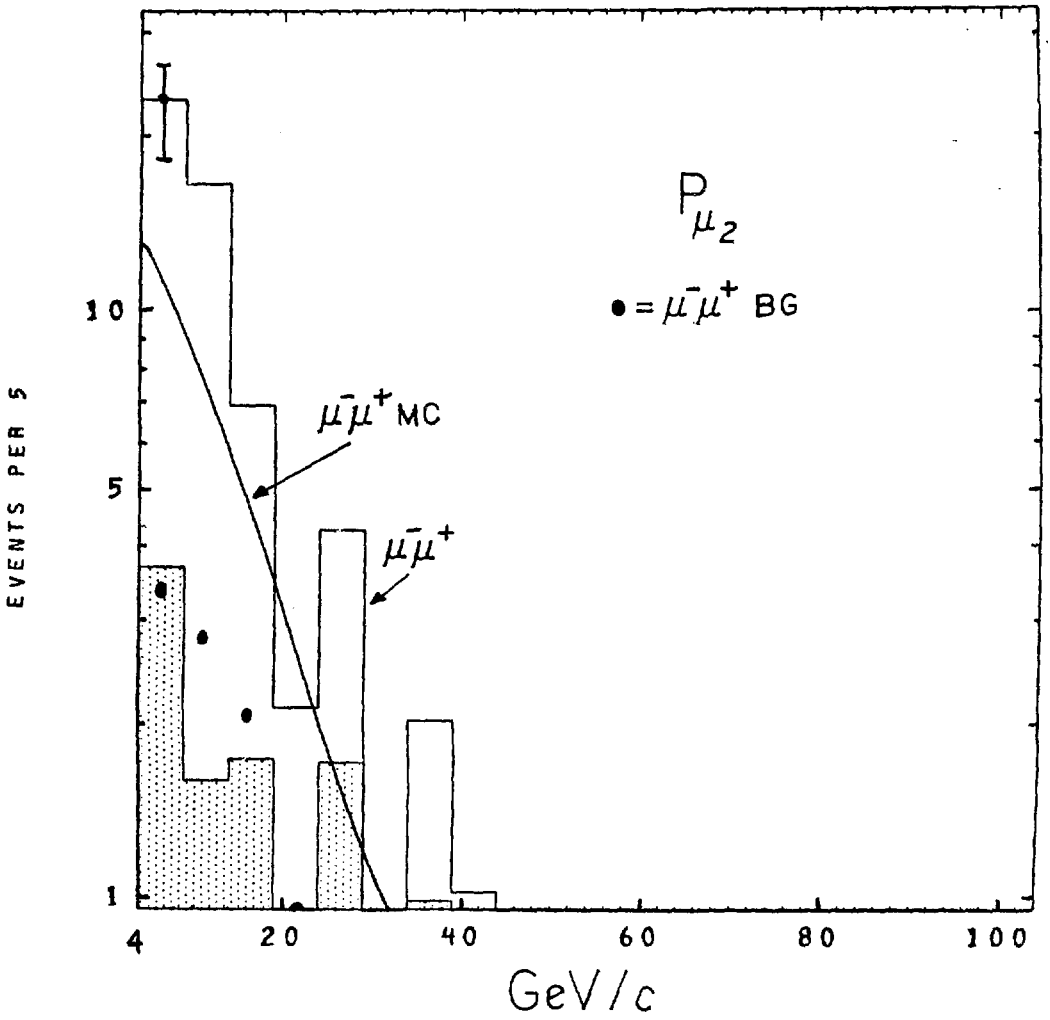
EVENTS PER 5
10
5
1
4
20
40
60
80
100
GeV/c
P_{μ_2}
● = $\mu^-\mu^+$ BG
$\mu^-\mu^+$ MC
$\mu^-\mu^+$

Fig. 7.13

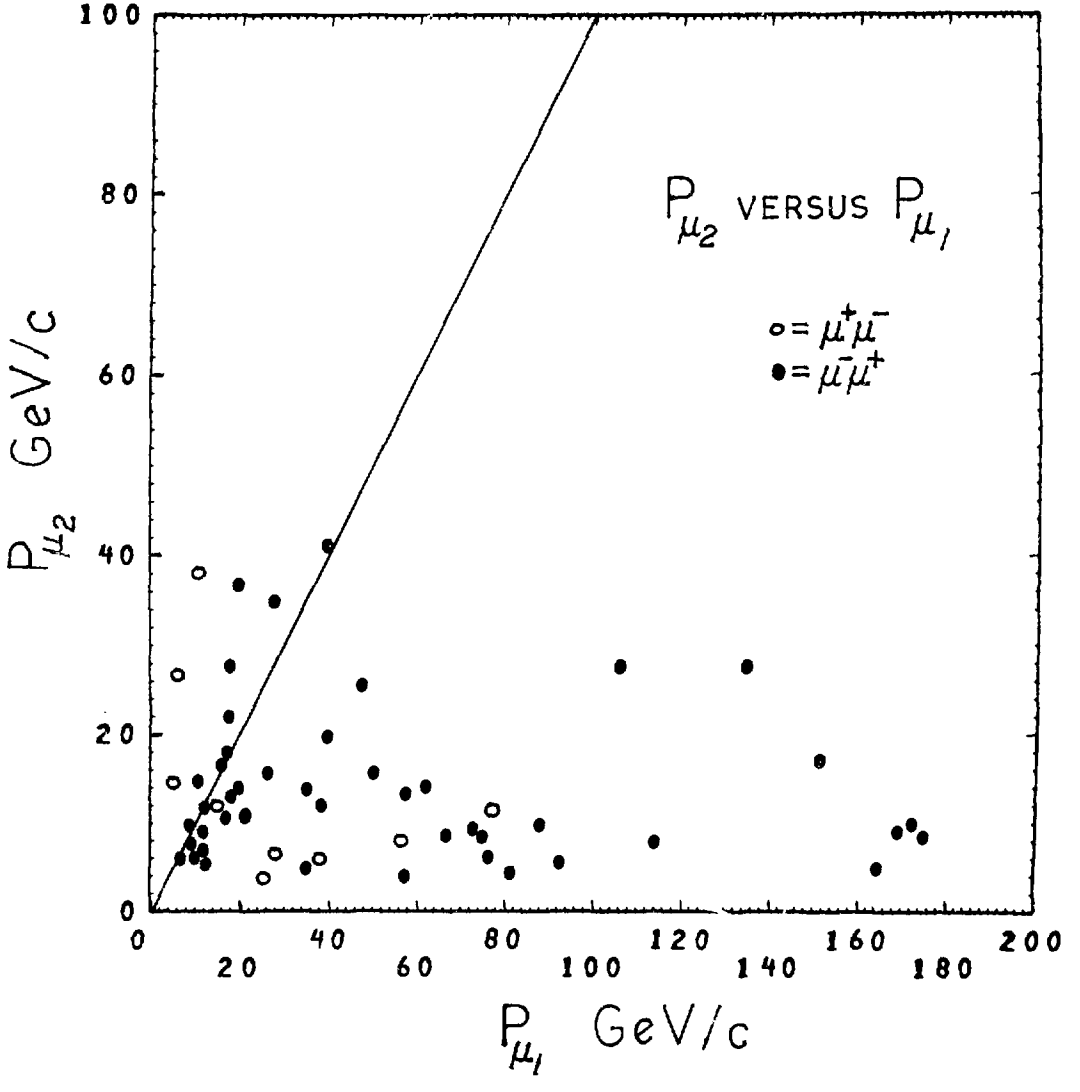
100
80
60
40
20
0
0
20
40
60
80
100
120
140
160
180
200
P_{μ_2} GeV/c
P_{μ_1} GeV/c
P_{μ_2} VERSUS P_{μ_1}
o = $\mu^+\mu^-$
● = $\mu^-\mu^+$

Fig. 7.14

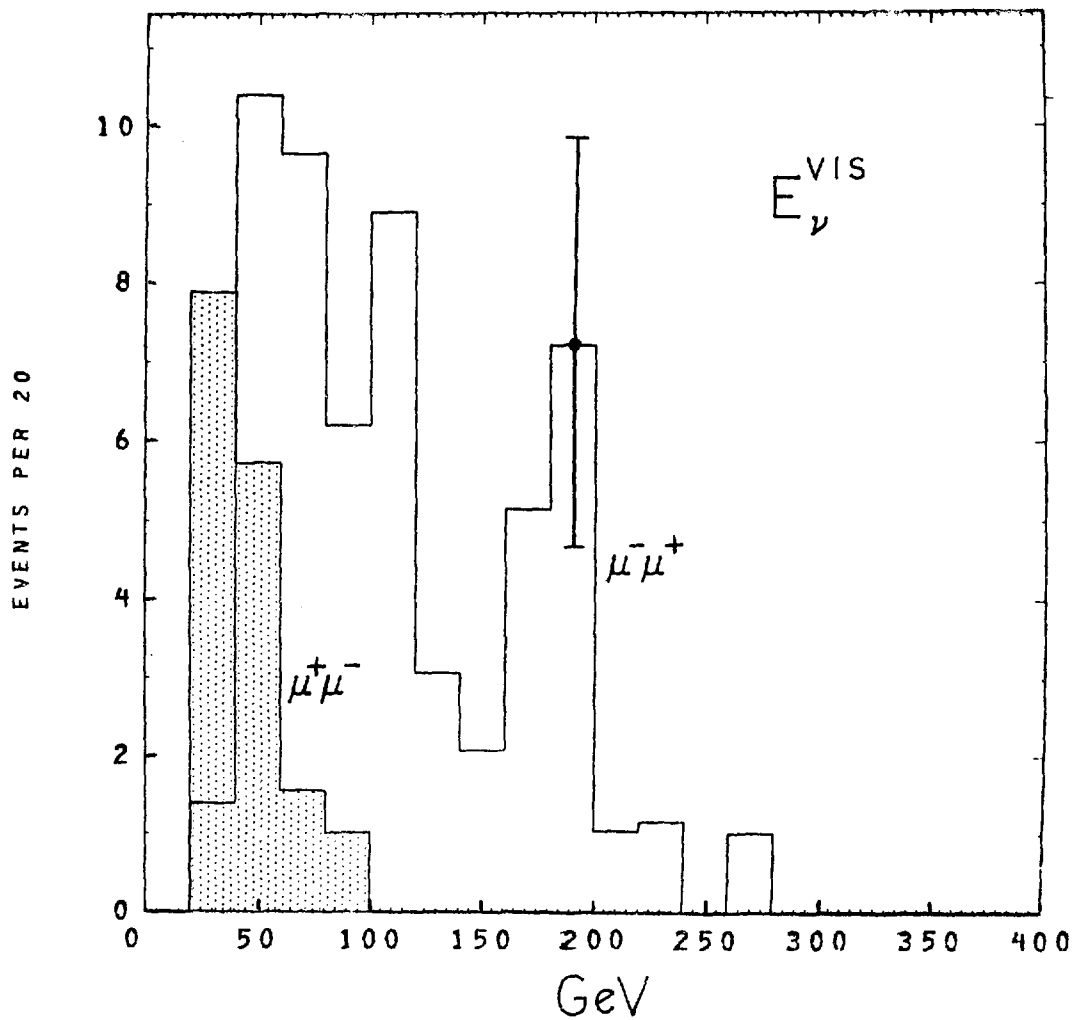
EVENTS PER 20
10
8
6
4
2
0
0
50
100
150
200
250
300
350
400
GeV
E_ν^{VIS}
$\mu^-\mu^+$
$\mu^+\mu^-$

Fig. 7.15a

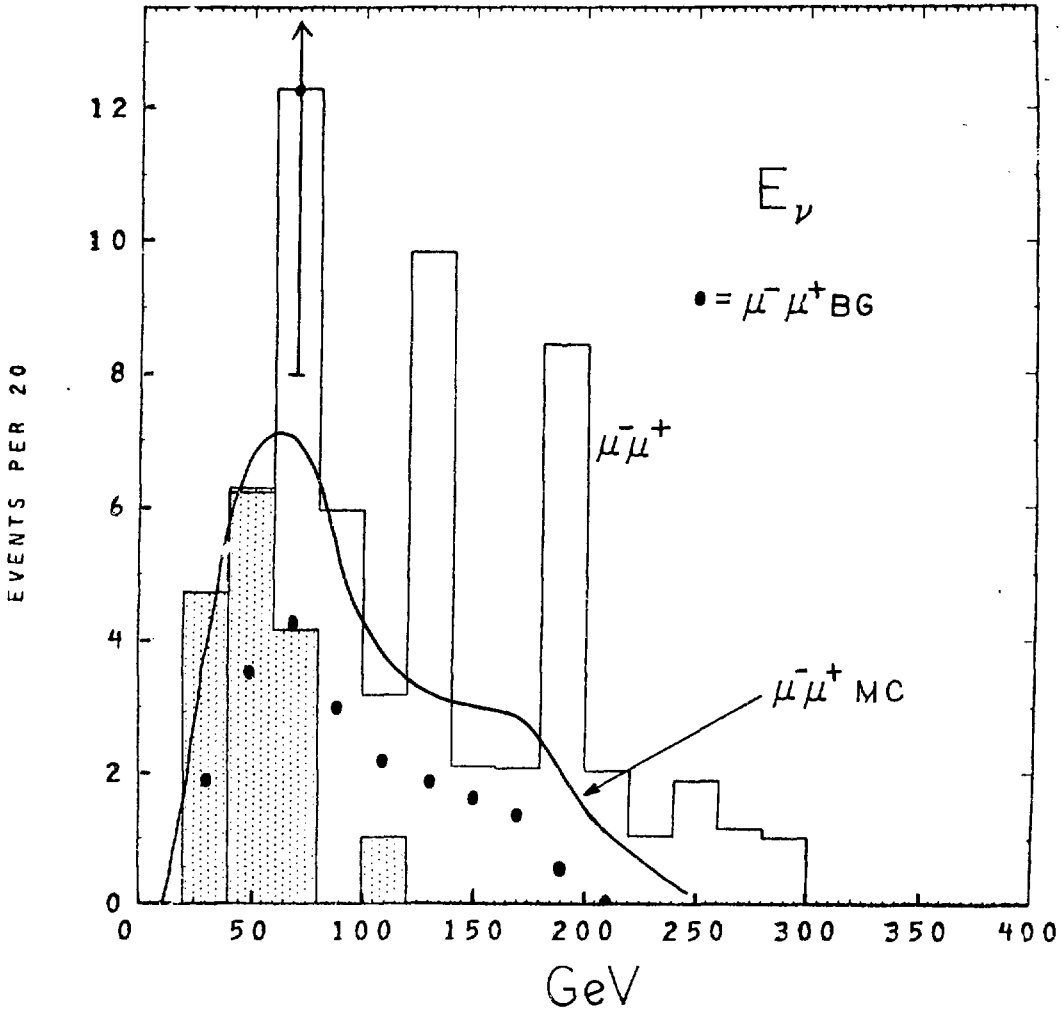
EVENTS PER 20
12
10
8
6
4
2
0
0
50
100
150
200
250
300
350
400
GeV
E_ν
• = $\mu^-\mu^+$ BG
$\mu^-\mu^+$
$\mu^-\mu^+$ MC

Fig. 7.15b

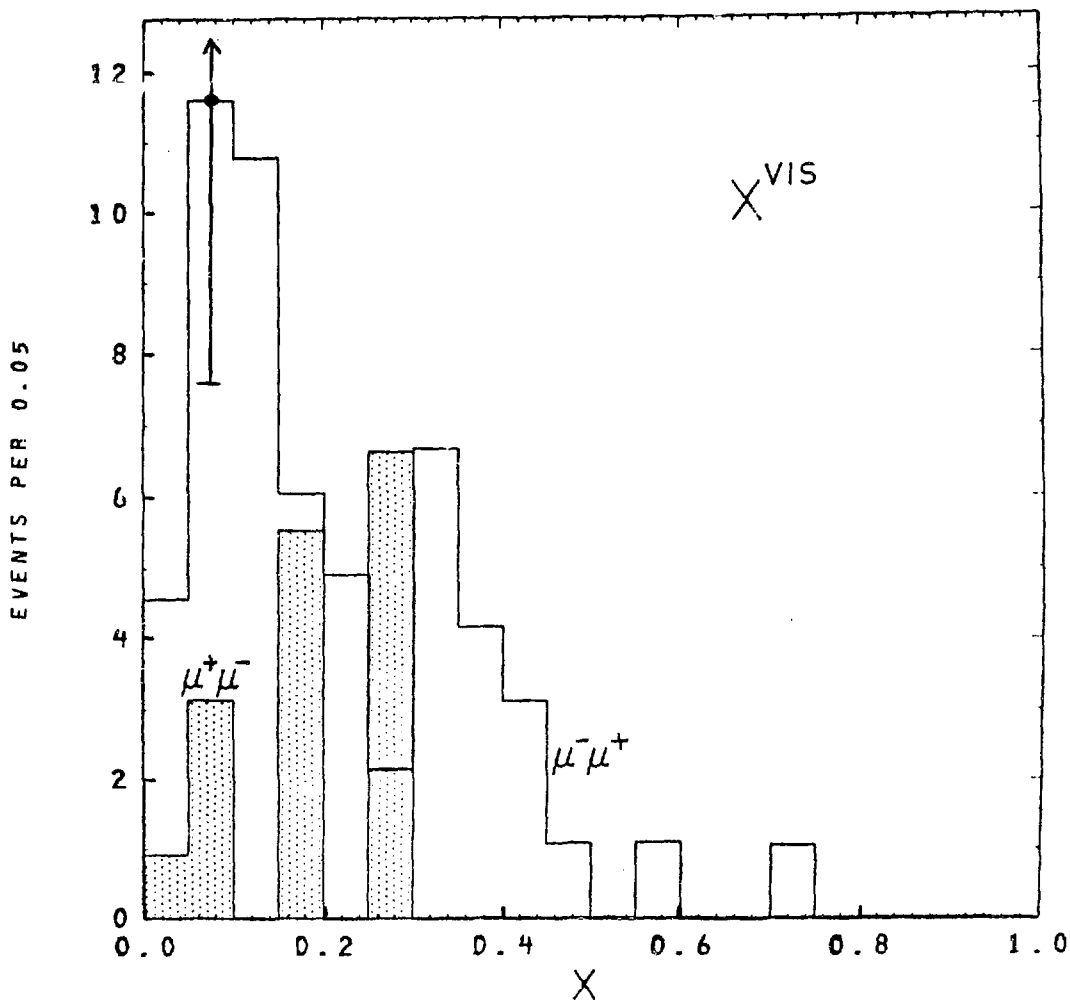

Fig. 7.16a

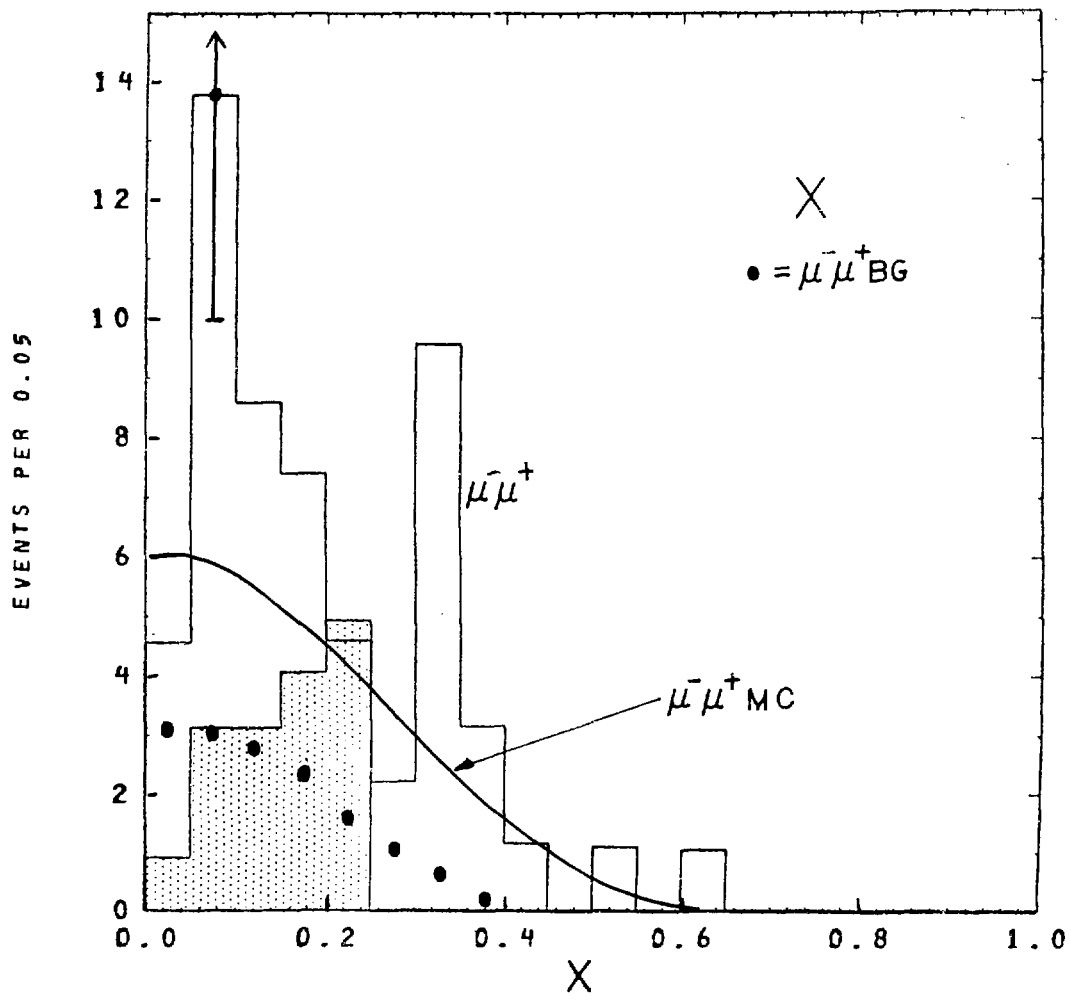

Fig. 7.16b

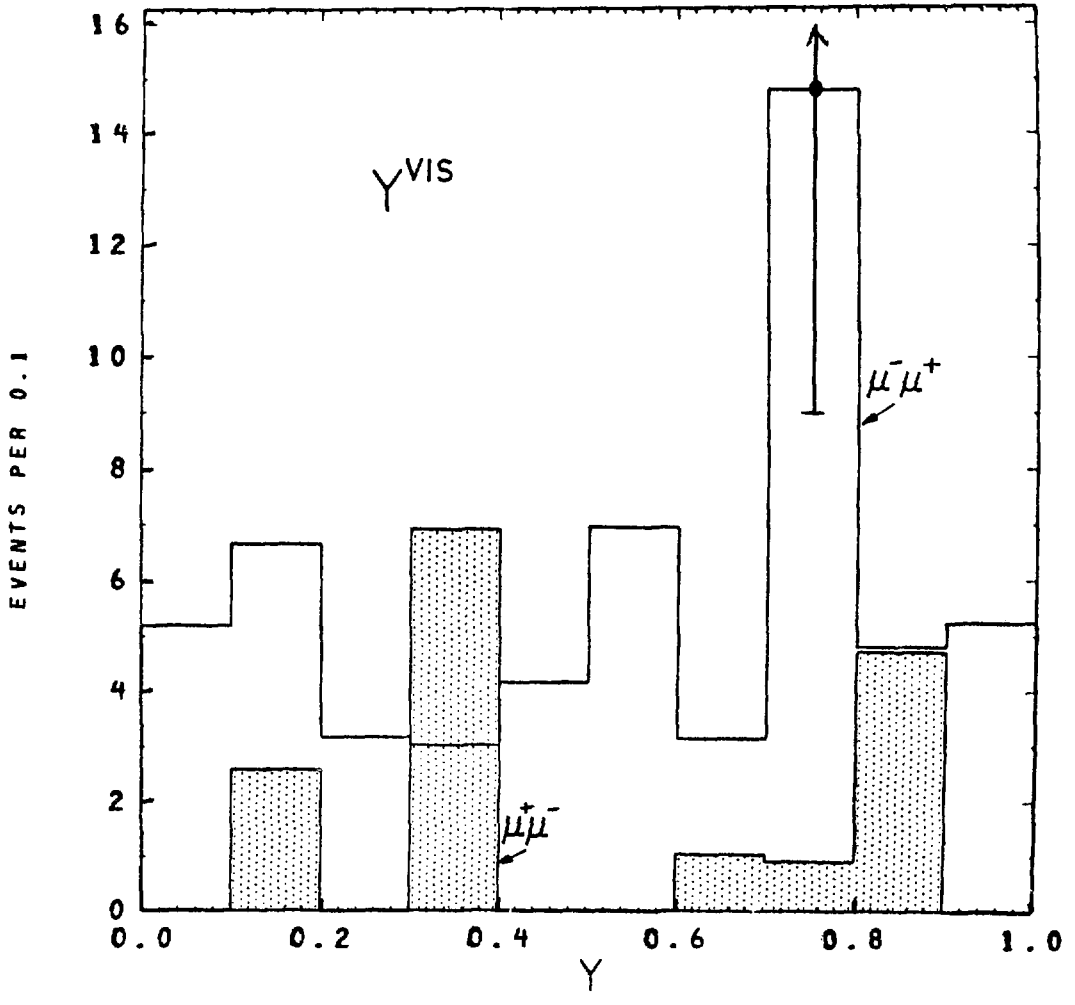

Fig. 7.17a

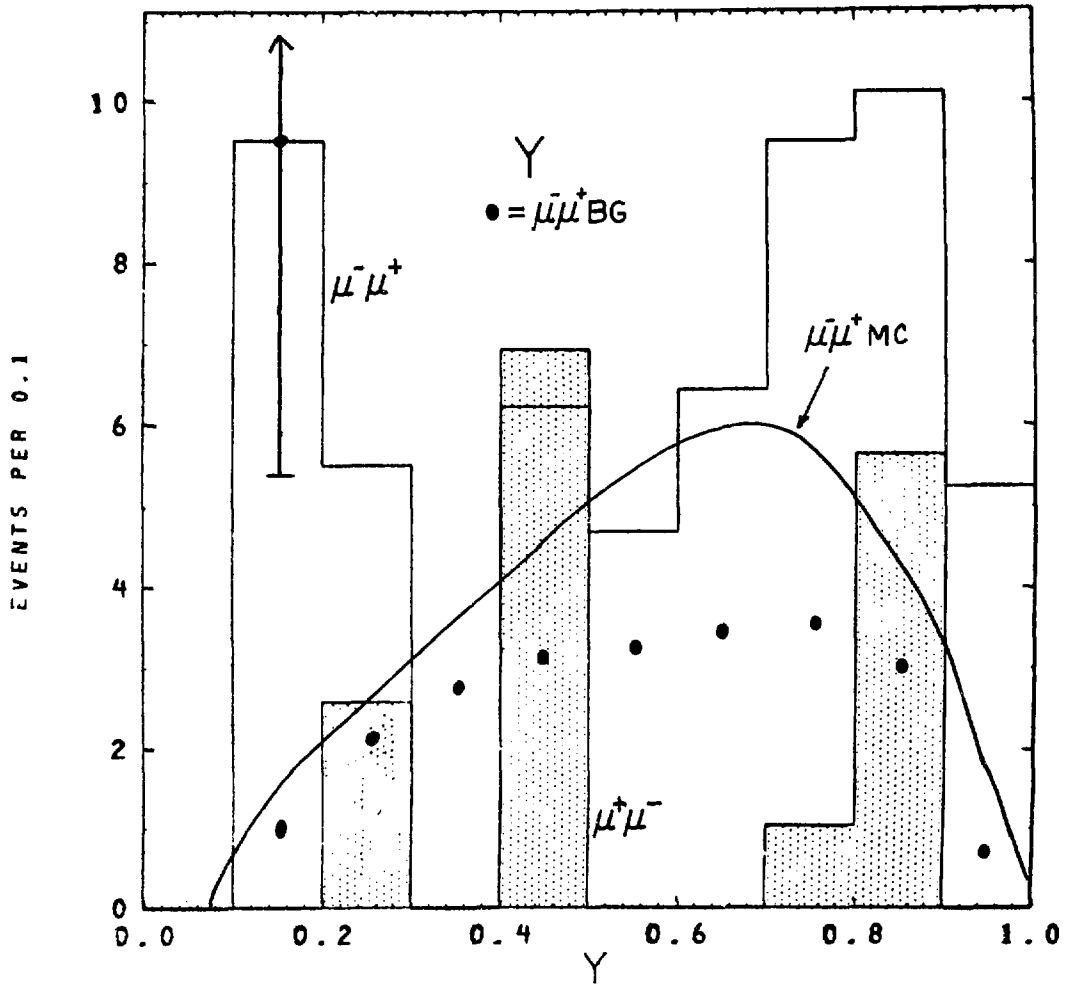

Fig. 7.17b

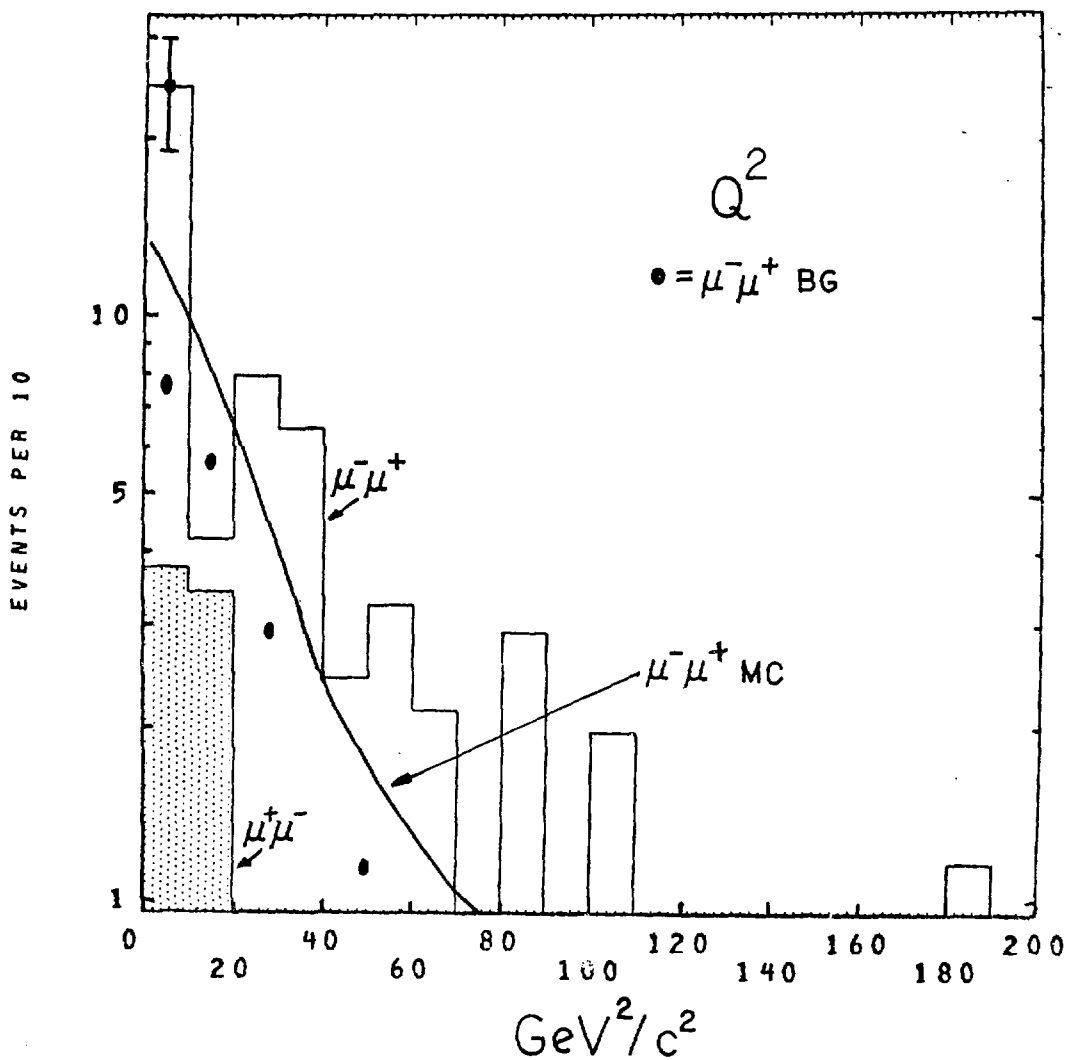
Q^2
● = $\mu^-\mu^+$ BG
$\mu^-\mu^+$
$\mu^-\mu^+$ MC
$\mu^+\mu^-$
EVENTS PER 10
10
5
1
0
20
40
60
80
100
120
140
160
180
200
GeV^2/c^2

Fig. 7.18

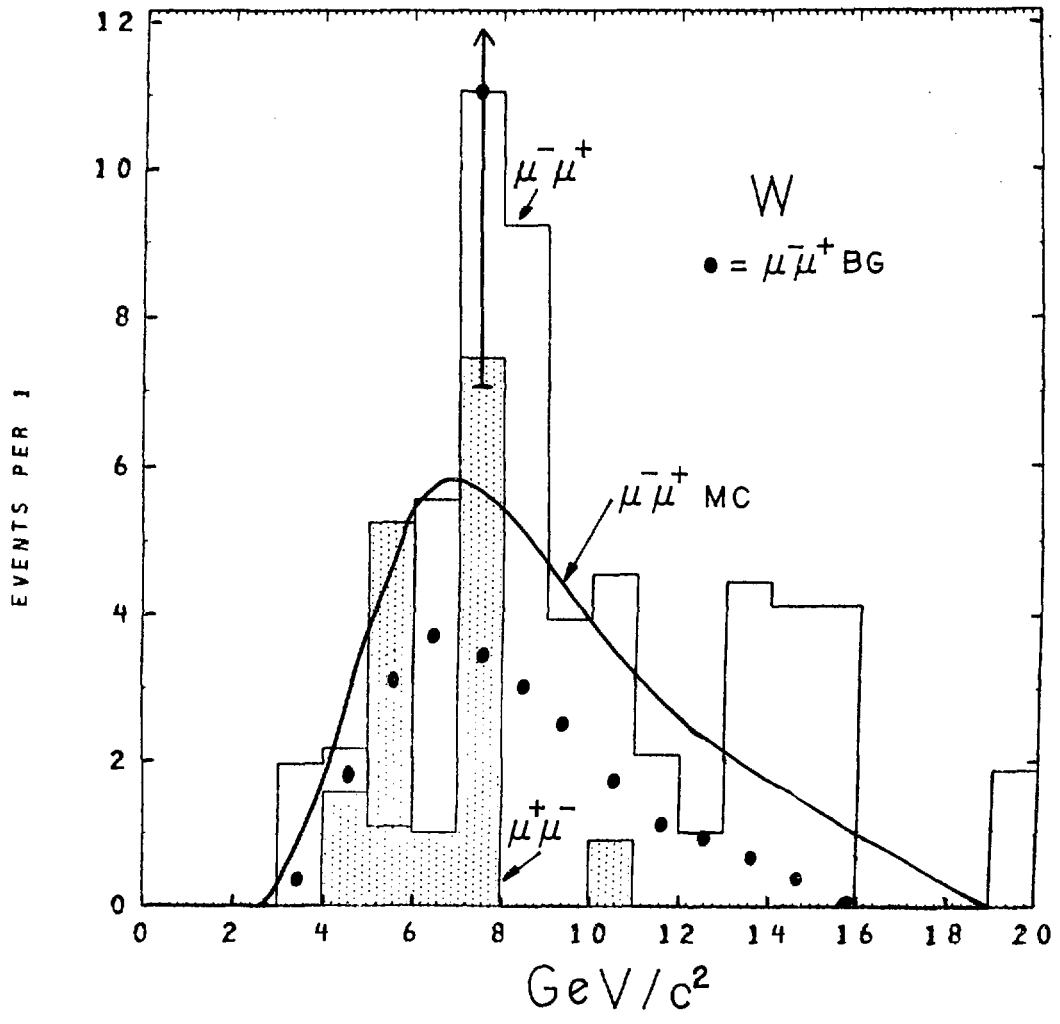
EVENTS PER 1
12
10
8
6
4
2
0
0
2
4
6
8
10
12
14
16
18
20
GeV/c²
μ⁻μ⁺
W
● = μ⁻μ⁺ BG
μ⁻μ⁺ MC
μ⁺μ⁻

Fig. 7.19

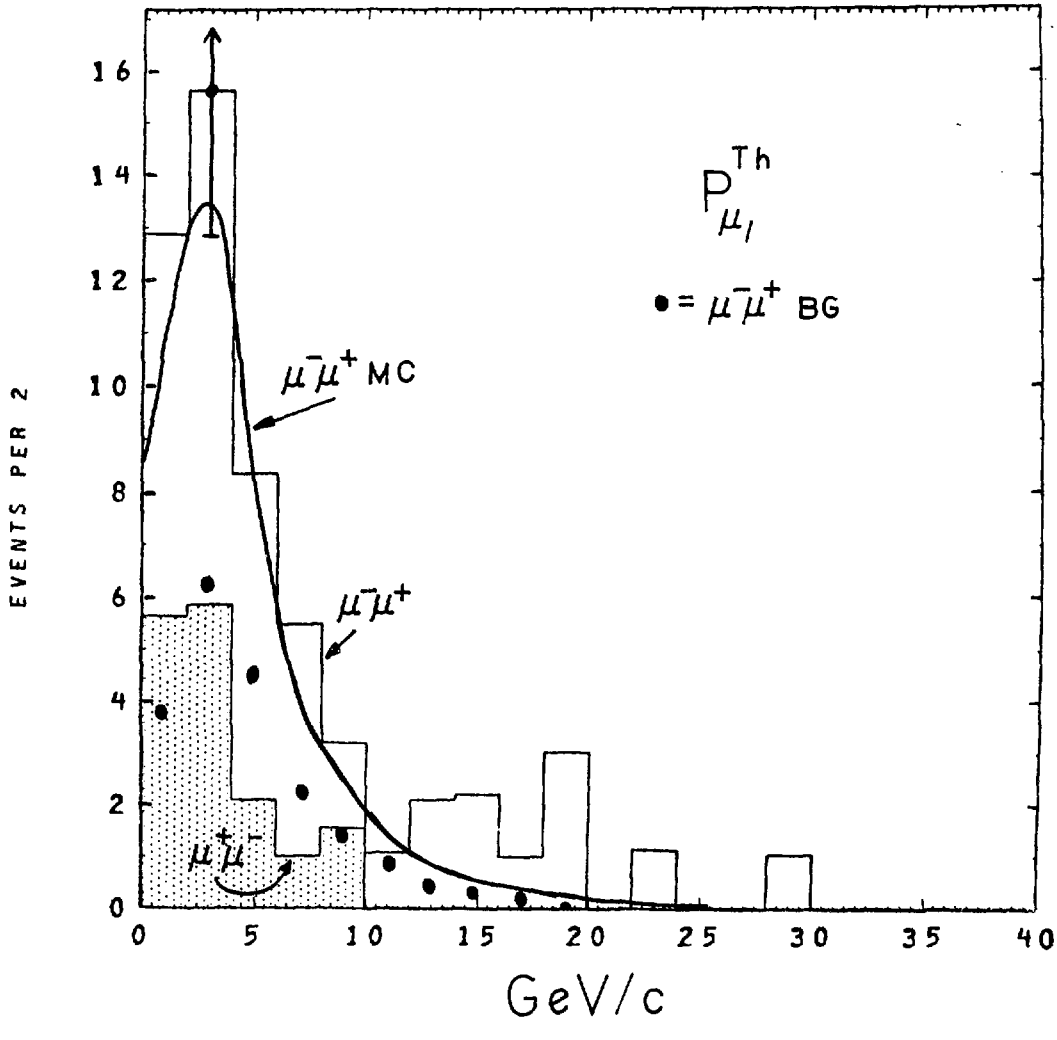
EVENTS PER 2
16
14
12
10
8
6
4
2
0
0
5
10
15
20
25
30
35
40
GeV/c
$P^{Th}_{\mu_1}$
● = $\mu^-\mu^+$ BG
$\mu^-\mu^+$ MC
$\mu^-\mu^+$
$\mu^+\mu^-$

Fig. 7.20

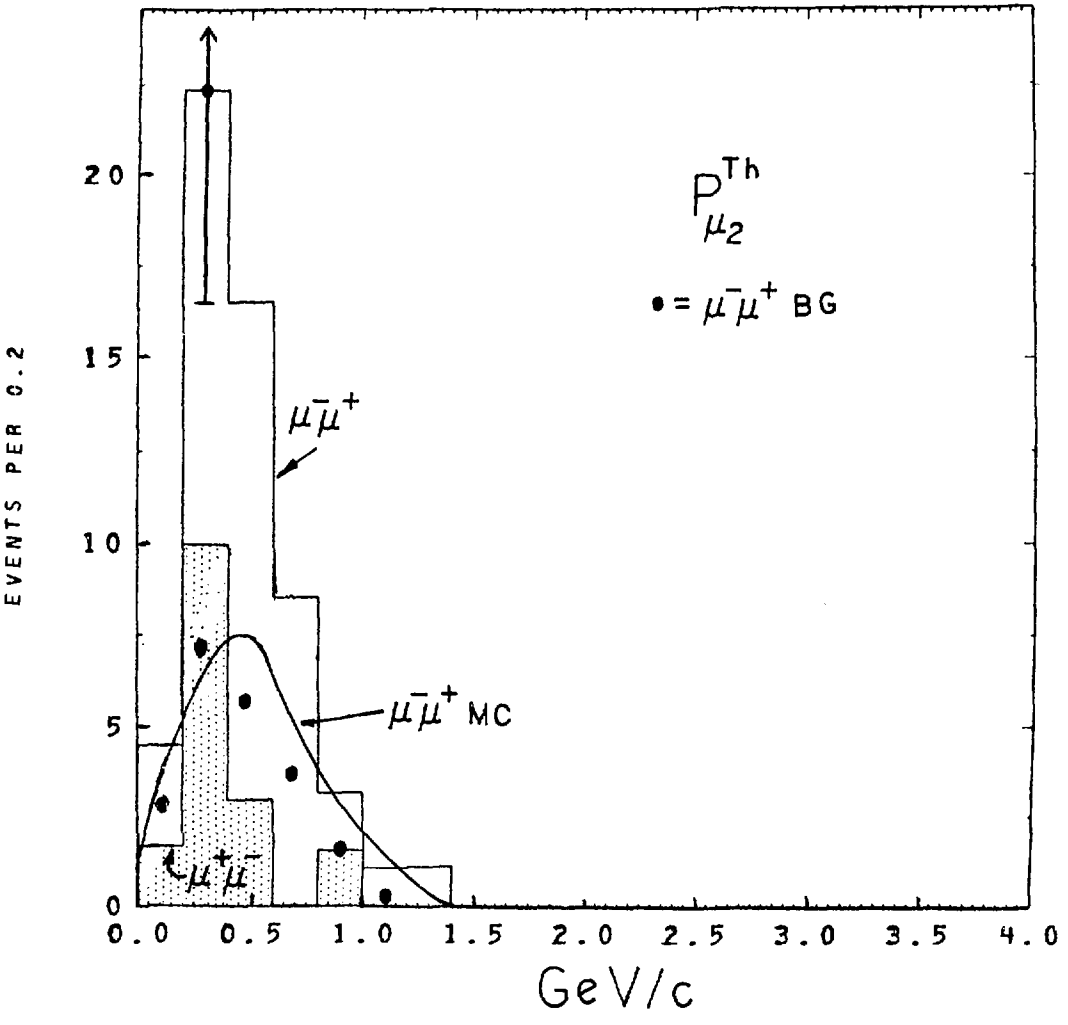
EVENTS PER 0.2
20
15
10
5
0
0.0
0.5
1.0
1.5
2.0
2.5
3.0
3.5
4.0
GeV/c
$P^{Th}_{\mu_2}$
• = $\mu^-\mu^+$ BG
$\mu^-\mu^+$
$\mu^-\mu^+$ MC
$\mu^+\mu^-$

Fig. 7.21

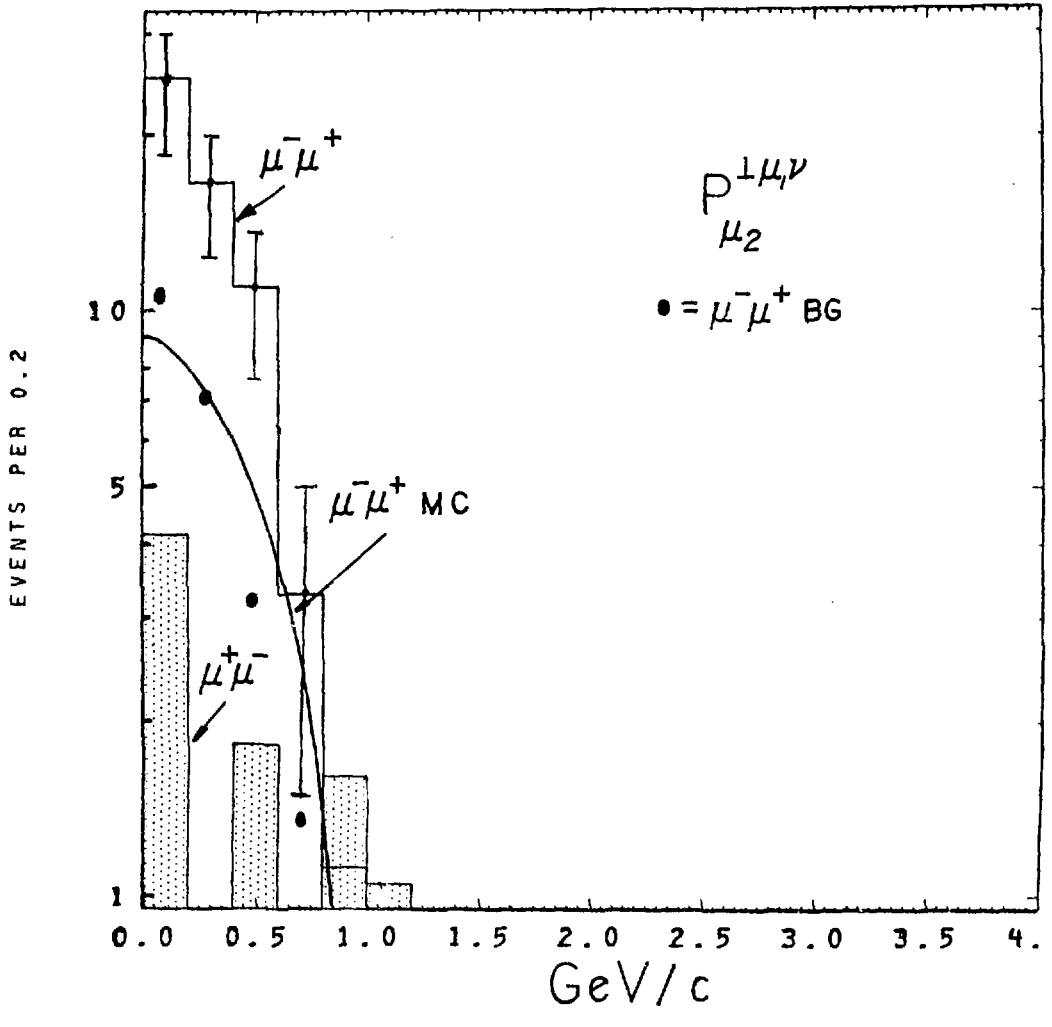
EVENTS PER 0.2
10
5
1
$\mu^-\mu^+$
$\mu^-\mu^+$ MC
$\mu^+\mu^-$
$P^{\perp\mu,\nu}_{\mu_2}$
• = $\mu^-\mu^+$ BG
0.0
0.5
1.0
1.5
2.0
2.5
3.0
3.5
4.0
GeV/c

Fig. 7.22

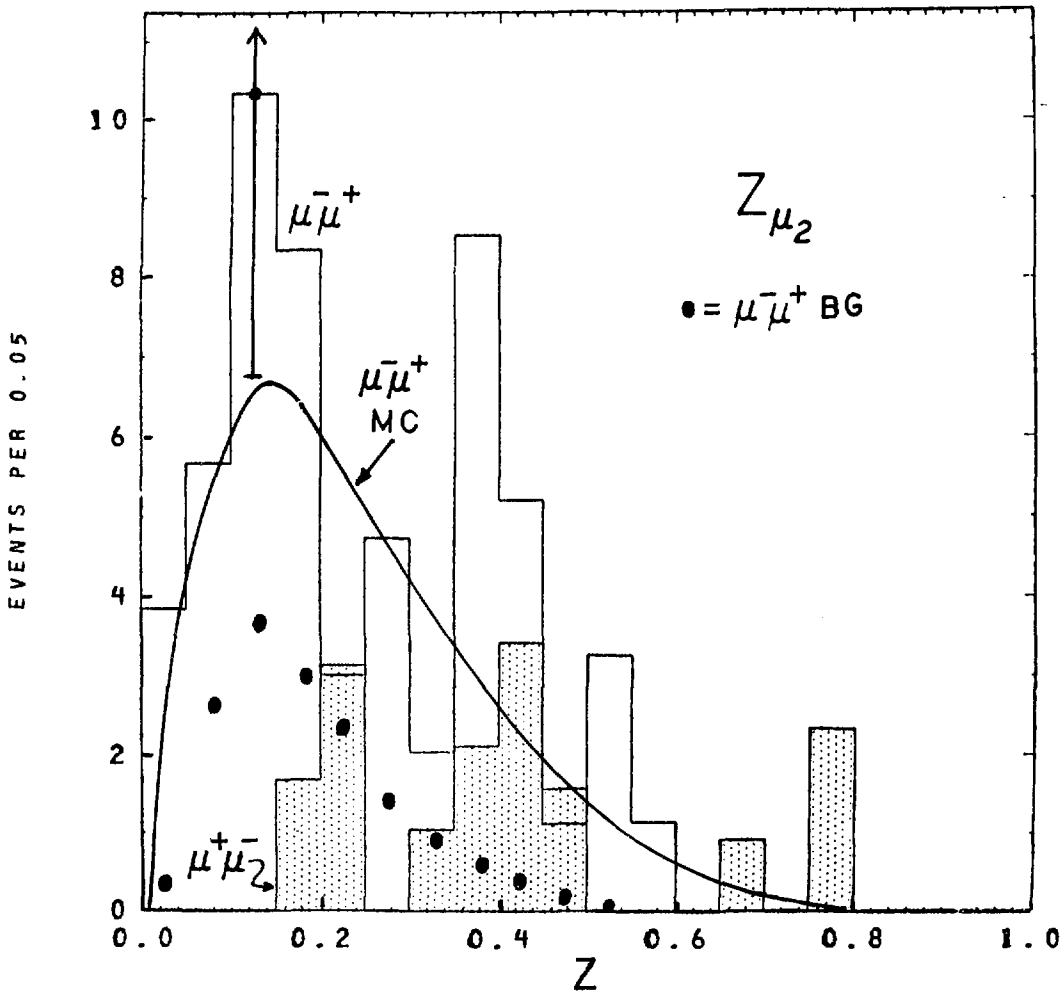
EVENTS PER 0.05
10
8
6
4
2
0
0.0
0.2
0.4
0.6
0.8
1.0
Z
$\mu^-\mu^+$
Z_{μ_2}
● = $\mu^-\mu^+$ BG
$\mu^-\mu^+$ MC
$\mu^+\mu^-_2$

Fig. 7.23

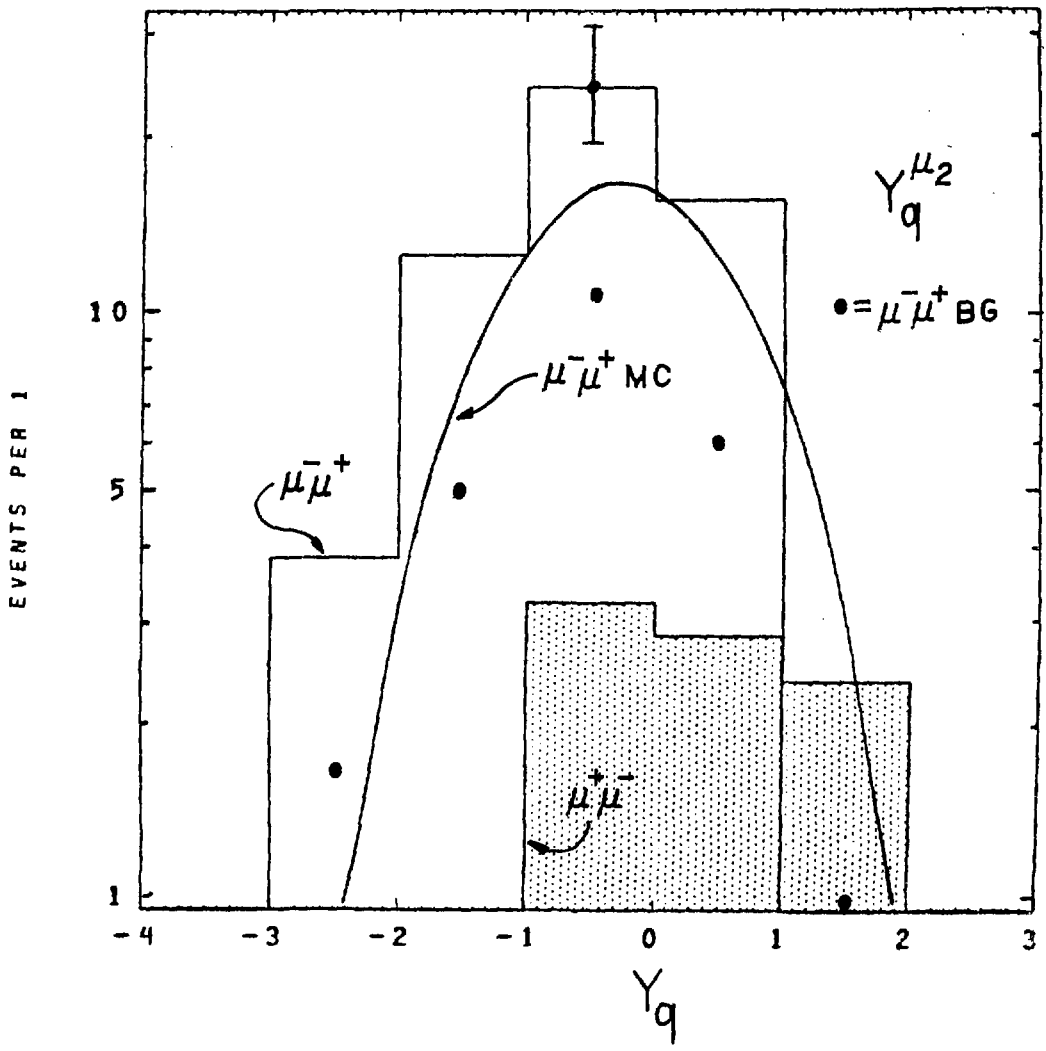
EVENTS PER 1
10
5
1
-4
-3
-2
-1
0
1
2
3
Y_q
$Y_q^{\mu_2}$
$\bullet = \mu^-\mu^+$ BG
$\mu^-\mu^+$ MC
$\mu^-\mu^+$
$\mu^+\mu^-$

Fig. 7.24

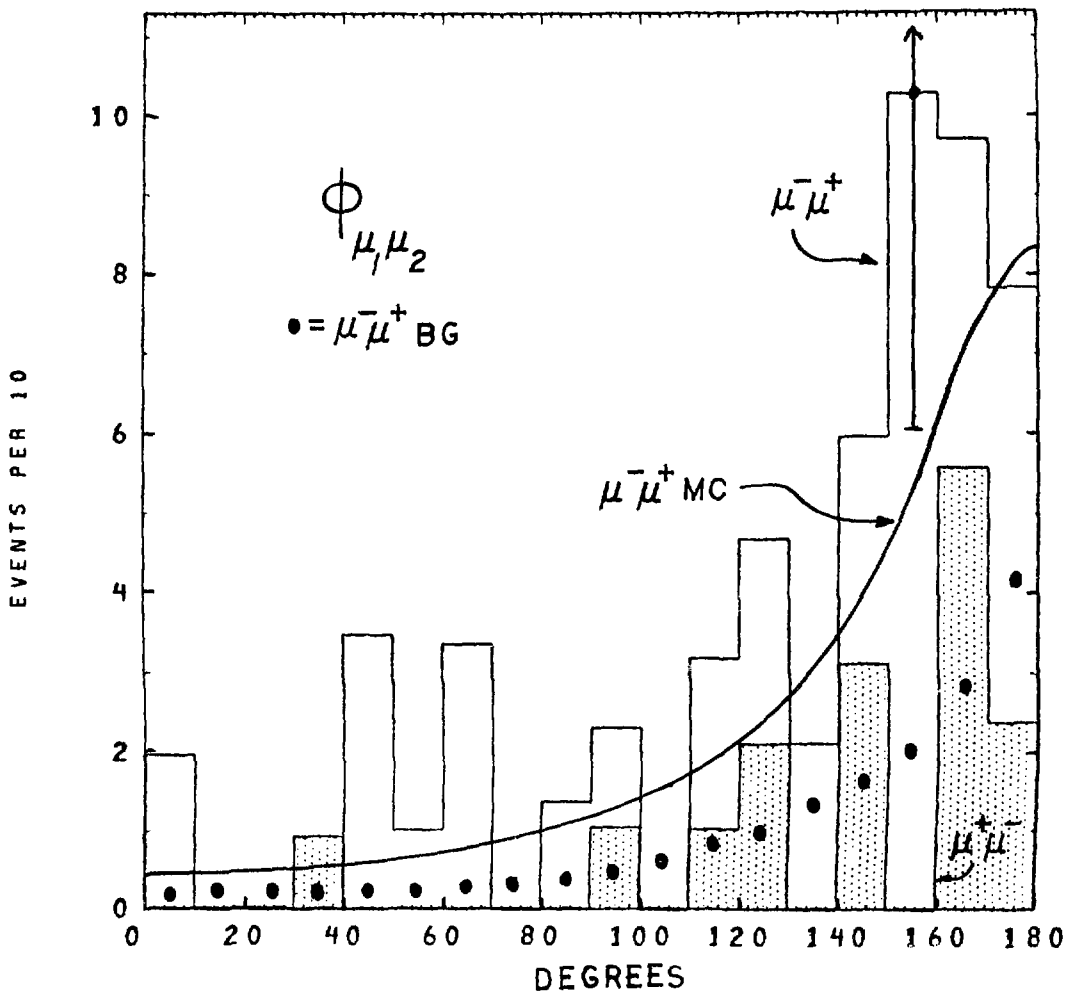
EVENTS PER 10
0
2
4
6
8
10
0
20
40
60
80
100
120
140
160
180
DEGREES
$\phi_{\mu_1\mu_2}$
• = $\mu^-\mu^+$ BG
$\mu^-\mu^+$
$\mu^-\mu^+$ MC
$\mu^+\mu^-$

Fig. 7.25

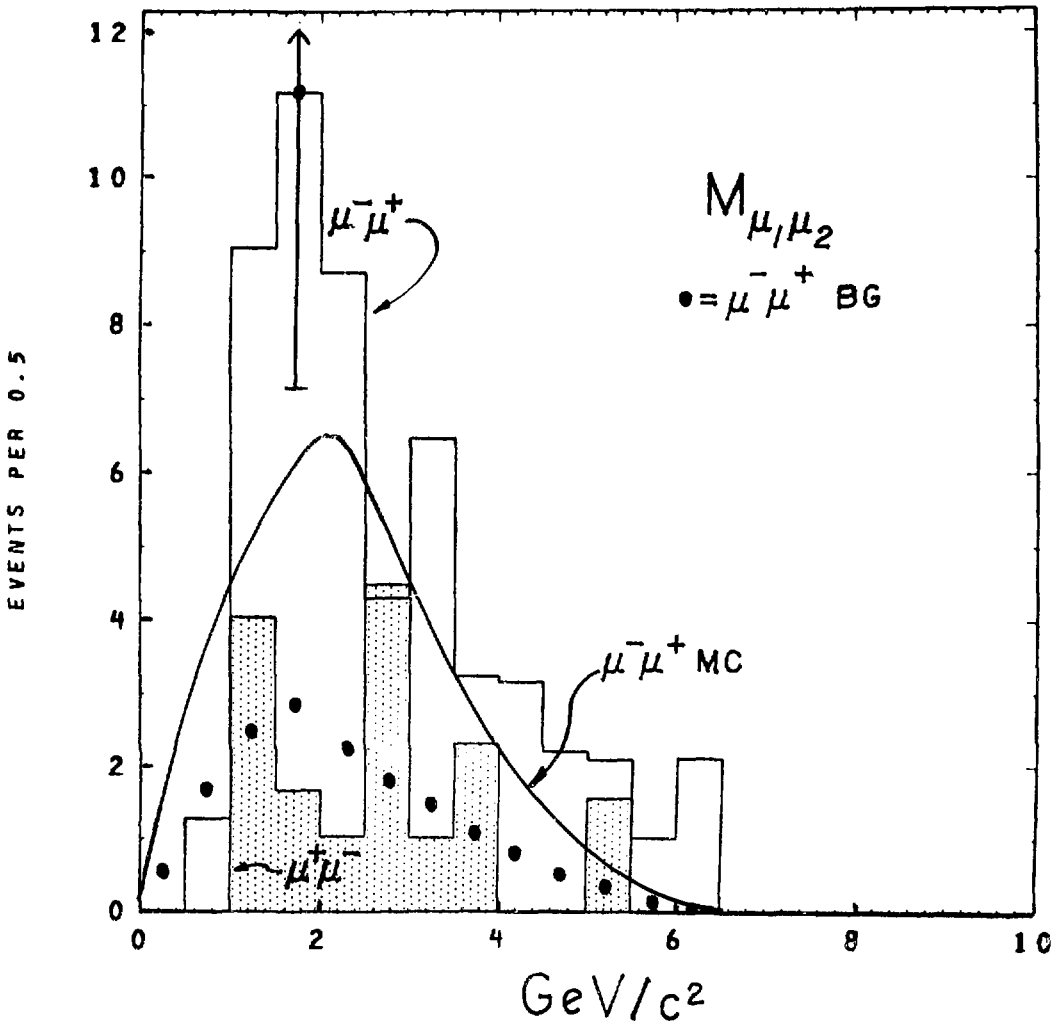
EVENTS PER 0.5
12
10
8
6
4
2
0
0
2
4
6
8
10
GeV/c²
$\mu^-\mu^+$
$M_{\mu_1\mu_2}$
● = $\mu^-\mu^+$ BG
$\mu^-\mu^+$ MC
$\mu^+\mu^-$

Fig. 7.26

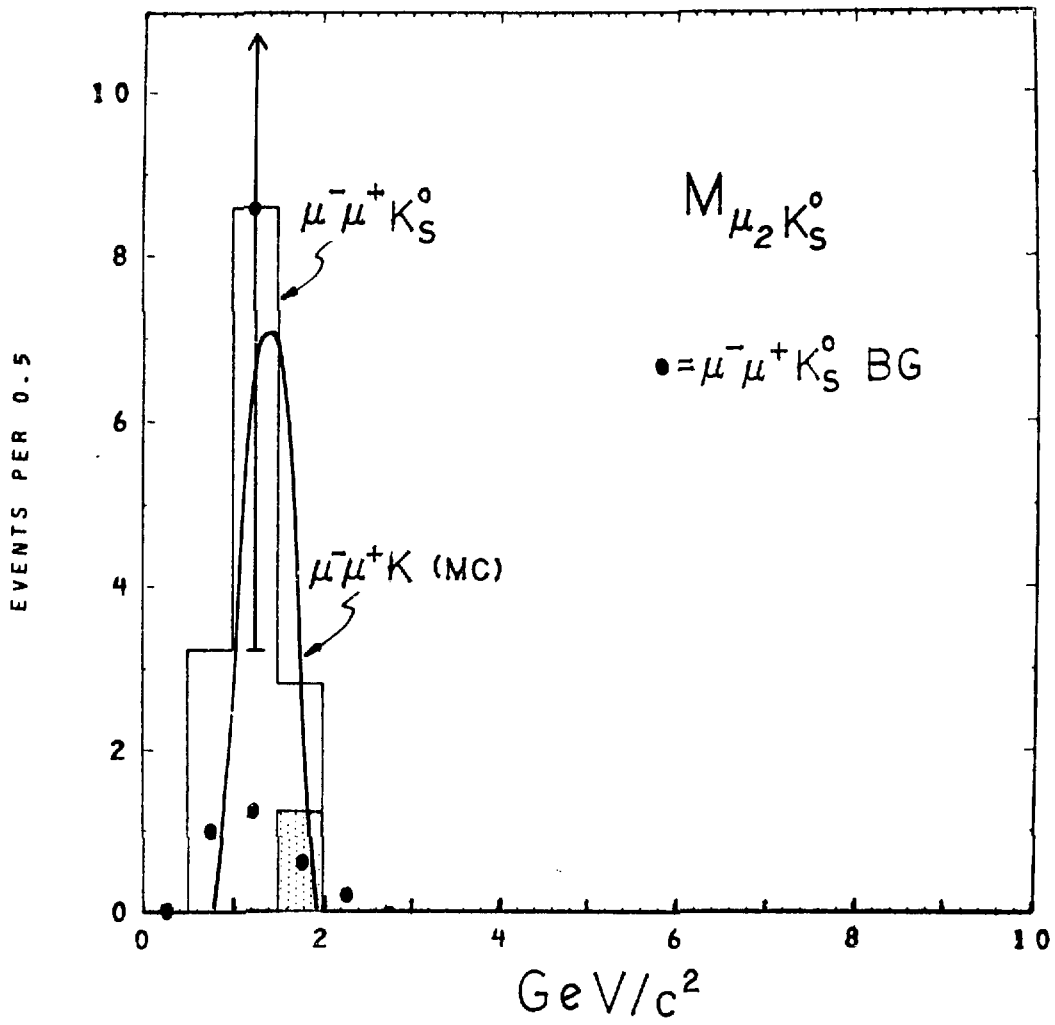
EVENTS PER 0.5
10
8
6
4
2
0
0
2
4
6
8
10
GeV/c²
μ⁻μ⁺K⁰S
μ⁻μ⁺K (MC)
Mμ₂K⁰S
●=μ⁻μ⁺K⁰S BG

Fig. 7.27a

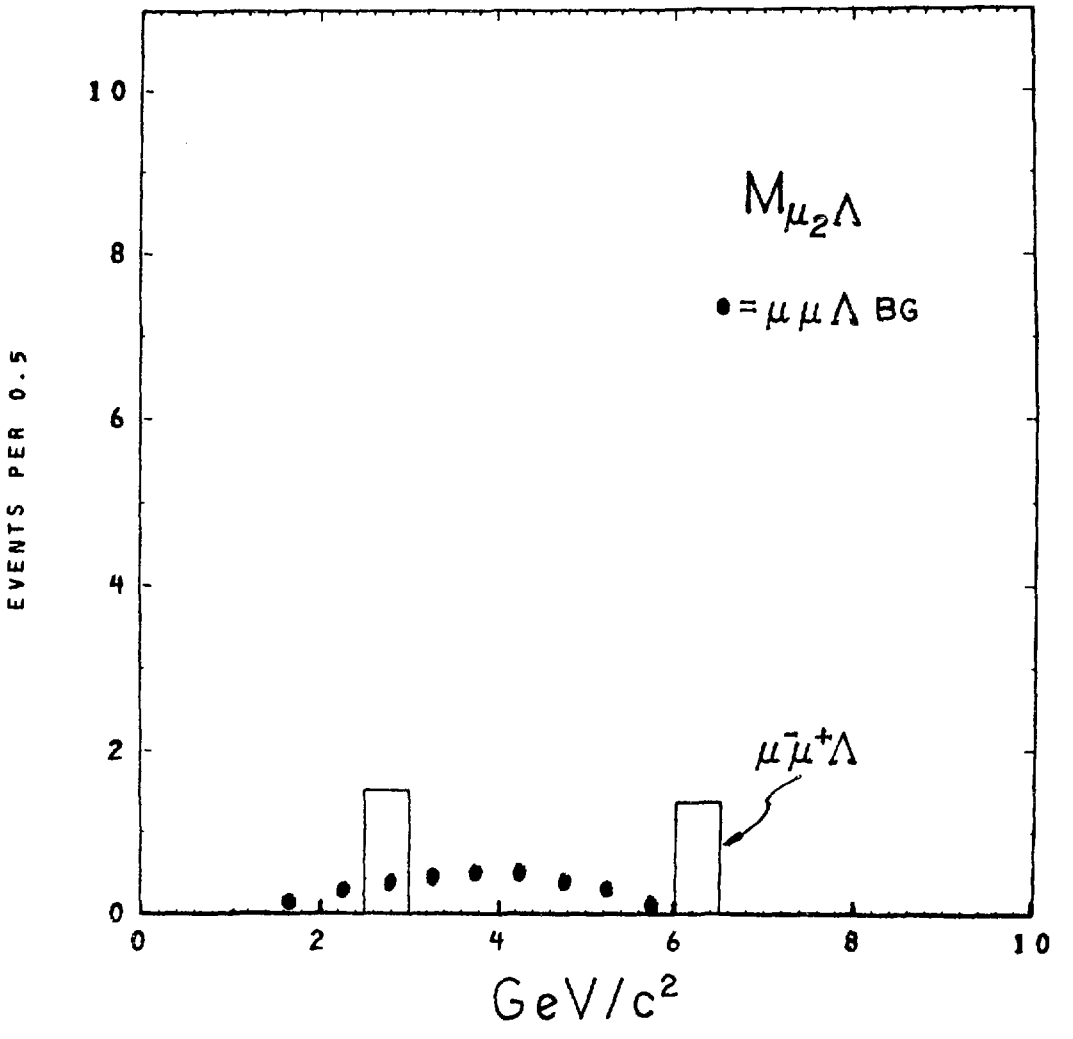
EVENTS PER 0.5
10
8
6
4
2
0
0
2
4
6
8
10
GeV/c²
$M_{\mu_2\Lambda}$
● = μμΛ BG
$\mu\bar{\mu}^+\Lambda$

Fig. 7.27b

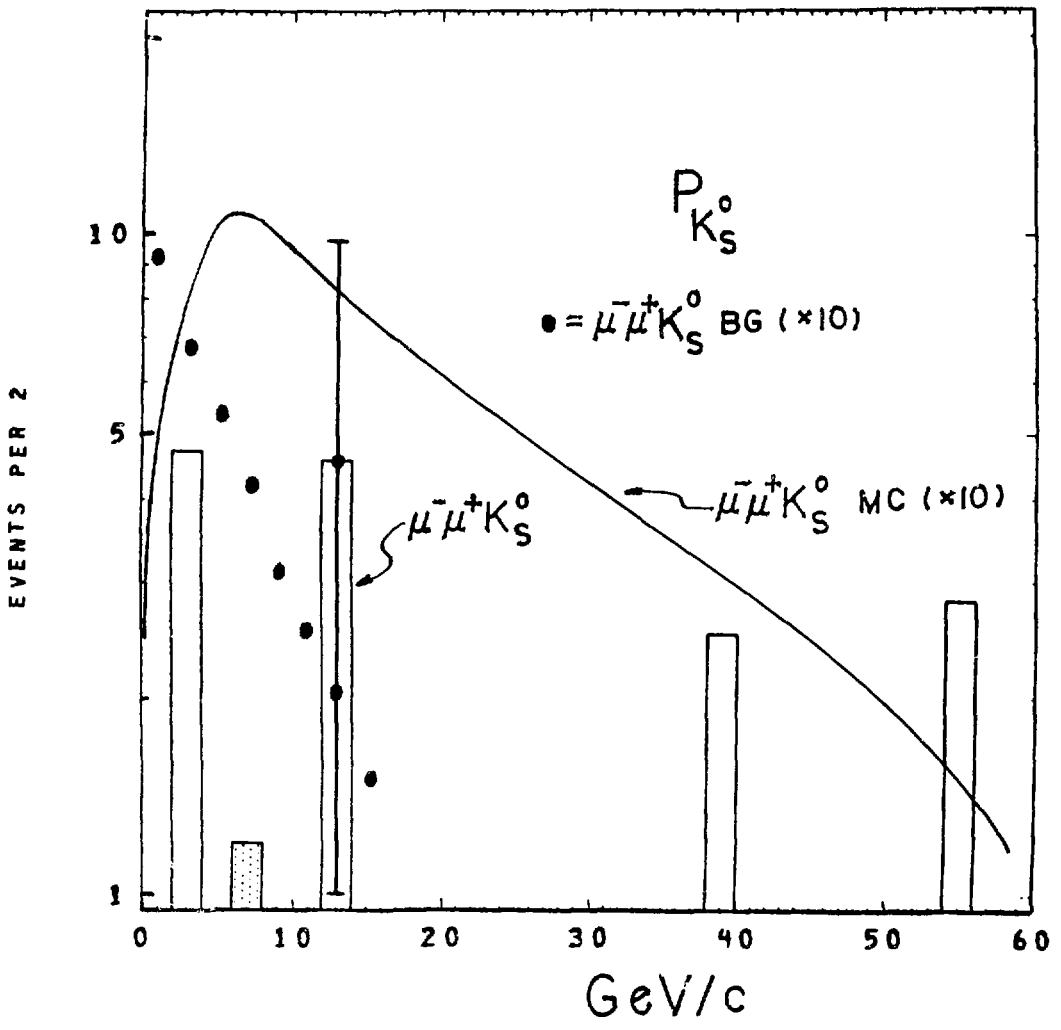
$P_{K^0_S}$
● = $\mu^-\mu^+K^0_S$ BG (×10)
$\mu^-\mu^+K^0_S$ MC (×10)
$\mu^-\mu^+K^0_S$
EVENTS PER 2
10
5
1
0
10
20
30
40
50
60
GeV/c

Fig. 7.23a

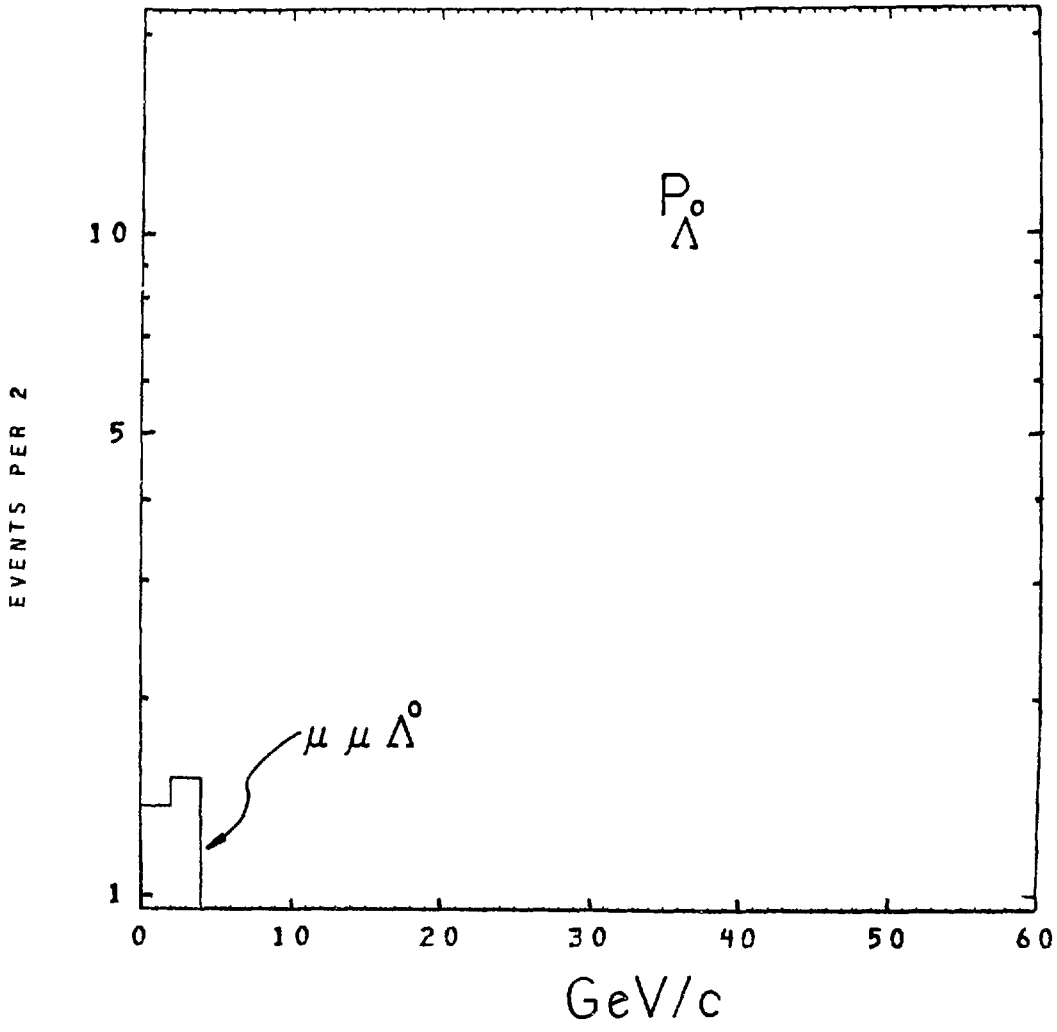
EVENTS PER 2
10
5
1
P_{Λ^0}
$\mu\,\mu\,\Lambda^0$
0
10
20
30
40
50
60
GeV/c

Fig. 7.28b

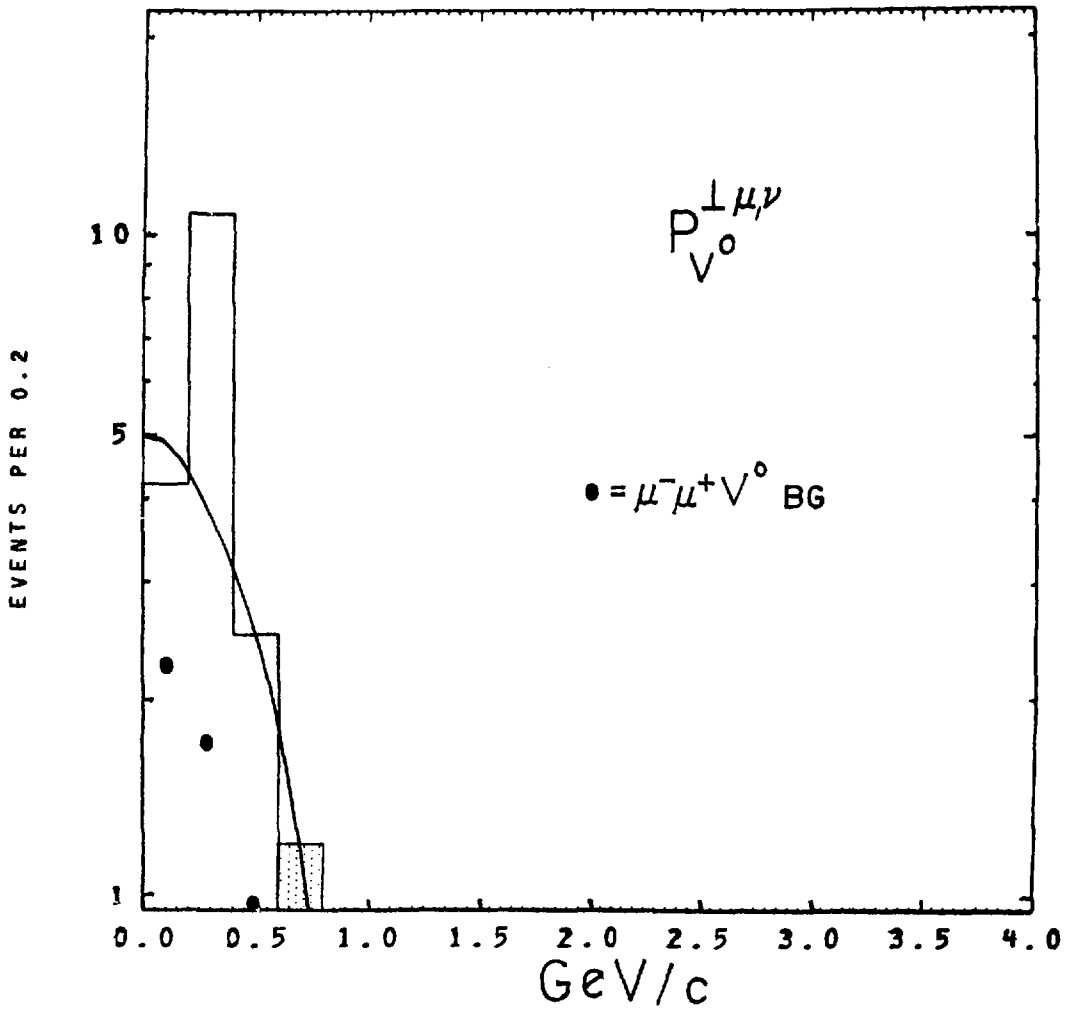
EVENTS PER 0.2
10
5
1
$P_{V^0}^{\perp \mu,\nu}$
● = $\mu^-\mu^+V^0$ BG
0.0
0.5
1.0
1.5
2.0
2.5
3.0
3.5
4.0
GeV/c

Fig. 7.29

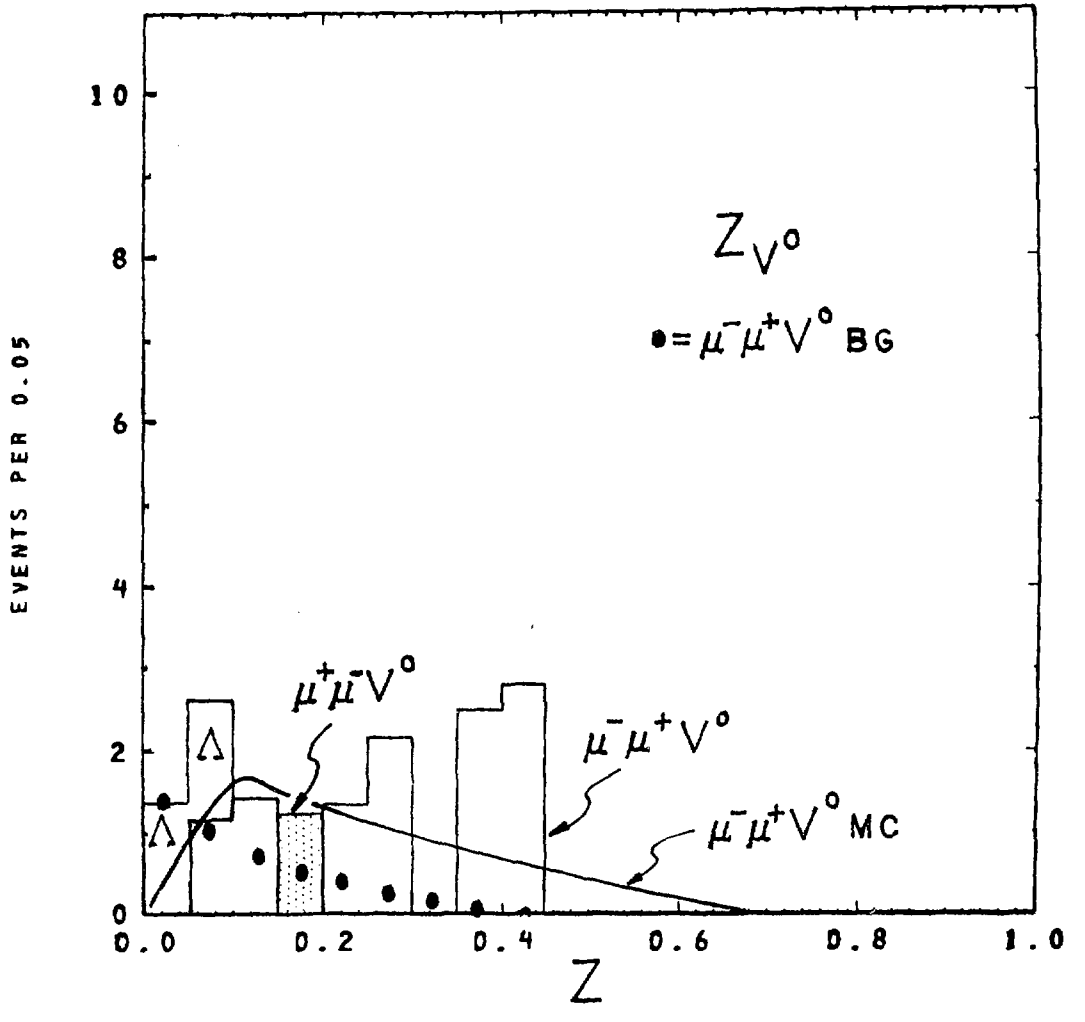
EVENTS PER 0.05
10
8
6
4
2
0
0.0
0.2
0.4
0.6
0.8
1.0
Z
Z_{V^0}
● = $\mu^-\mu^+V^0$ BG
$\mu^+\mu^-V^0$
$\mu^-\mu^+V^0$
$\mu^-\mu^+V^0$ MC
Λ
Λ

Fig. 7.30

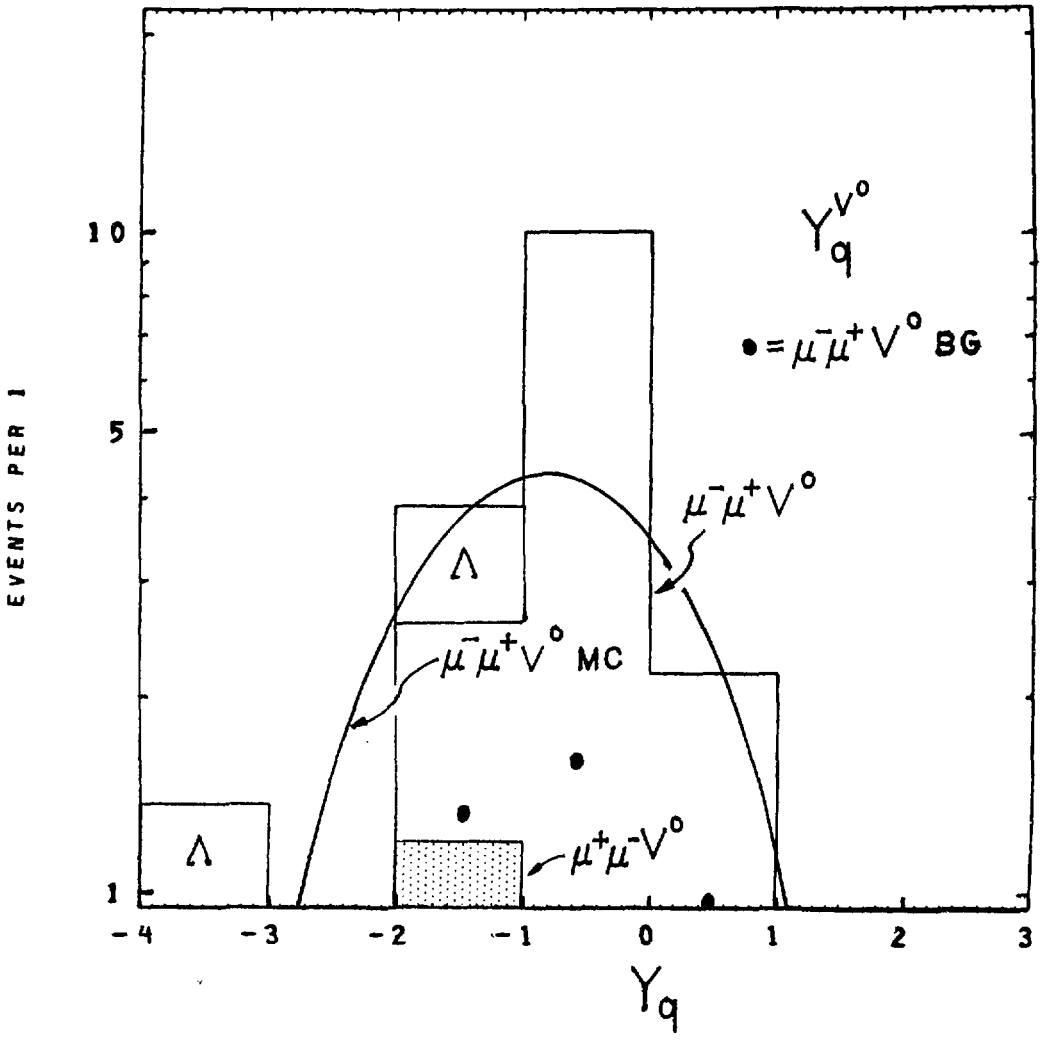
EVENTS PER 1
10
5
1
-4
-3
-2
-1
0
1
2
3
Y_q
$Y_q^{V^0}$
● = $\mu^-\mu^+V^0$ BG
$\mu^-\mu^+V^0$
$\mu^-\mu^+V^0$ MC
$\mu^+\mu^-V^0$
Λ
Λ

Fig. 7.31